Channel flow stability: influence of dust particles and geometry

A Thesis

Submitted to the

Tata Institute of Fundamental Research, Mumbai

Subject Board of Physics

for the degree of Doctor of Philosophy

by

Anup Kumar

International Centre for Theoretical Sciences

Tata Institute of Fundamental Research

Bengaluru, India.

December, 2025

DECLARATION

This thesis is a presentation of my original research work. Wherever contributions of others are involved, every effort is made to indicate this clearly, with due reference to the literature, and acknowledgment of collaborative research and discussions.

The work was done under the guidance of Professor Rama Govindarajan at the International Centre for Theoretical Sciences Tata Institute of Fundamental Research, Bengaluru.

Anup Kumar

8 December 2025

In my capacity as the formal supervisor of record of the candidate's thesis, I certify that the above statements are true to the best of my knowledge.

Prof. Rama Govindarajan

Date: 8 December 2025

Acknowledgements

I sincerely thank my advisor, Rama Govindarajan, for her invaluable guidance and support throughout this research. I am also grateful to my colleagues: Sarath Jose, Uddeepta Deka, Souvik Jana, Soumav Kapoor, Harshit Joshi, Shashank Roy, and many others for their insightful discussions and companionship.

A heartfelt thanks to my parents, Harender Prasad and Lalit Devi, and my wife, Sumi Shaw, for their unwavering support and encouragement.

I also extend my gratitude to ICTS and its members, especially Suresh, Krishna, Kishor, Basavraj, the security staffs, and many others whose support made this journey possible. Thank you all!

I dedicate this thesis to my parents

Harender Prasad

and

Lalti Devi

Contents

List of Publications

- A. Kumar and R. Govindarajan, "Mechanism of instability in non-uniform dusty channel flow". Published in *Journal of Fluid Mechanics*.
- A. Kumar and R. Govindarajan, "On the intense sensitivity to wall convergence of instability in a channel". Published as a featured article in a special issue of *Physics of Fluids*.
- A. Kumar and R. Govindarajan, "Horizontal channel flow with slowly sinking particles". The manuscript is currently in preparation and will be submitted soon."

Abstract

The dynamics of fluids laden with suspended particles has been a subject of investigation for decades. When the particles are extremely small and in great number, the term "dusty flow" is appropriate. Dusty shear flows are ubiquitous: occurring in environmental phenomena like dust storms, snow avalanches, and sediment transport in rivers, and in industrial processes like the manufacture of fertilizers and various powders. Whether such a flow will be laminar, turbulent, or in an unsteady transitional state is of great interest for a variety of reasons, and the first step is to study the stability of the laminar base state. Also, in practical applications, we know that it is extremely difficult to manufacture a pipe or channel that is perfectly straight, and if a small departure from being absolutely straight has such a profound effect on stability, this feature should surely be taken into consideration while drawing conclusions about the transition to turbulence.

For decades, shear flows have thrown up surprises in their stability behaviour, and the different mechanisms of instability, though not easy to predict, are crucial to unravel. In my thesis, I address the following problems:

- The stability of channel flow with non-uniformly distributed dust particles.
- The stability of channel flow with non-uniformly distributed dust particles under the influence of gravity.
- The stability of channel flow with slightly converging walls.

While these systems may appear similar, they are fundamentally distinct and exhibit significantly different stability behaviours. Despite these differences, they share common underlying physics, as their stability is governed by critical-layer dynamics, which I have demonstrated in my studies. Below, I give a summary of the problems, the methodology, and the findings in each case of study. It is essentially the synopsis of my thesis.

0.1 The stability of channel flow with non-uniformly distributed dust particles

0.1.1 Description of the system

I investigate here a dilute suspension of particles in a pressure-driven channel flow, a schematic of which is shown in Figure 1a . The impact of this suspension on the flow is

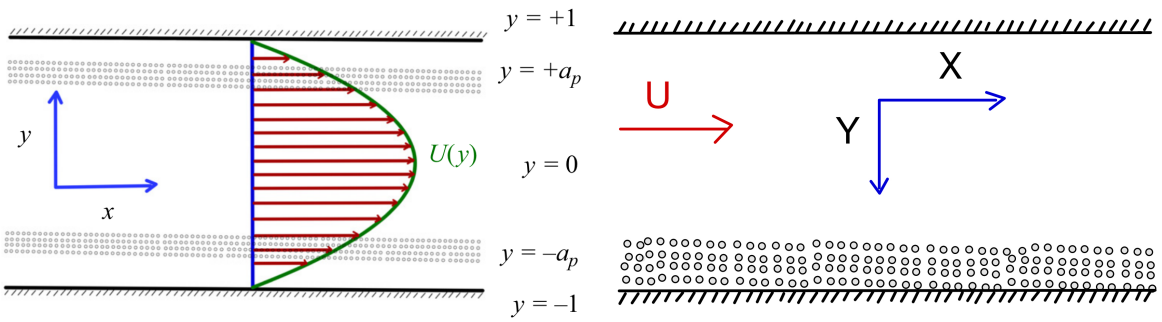

(a) (b)

Figure 1: Schematics of the flows under consideration. (a) The particles are concentrated around $y = \pm a_p$ within a band of size σ. (b) Quasi-steady state of particles settling under gravity.

characterized by a two-way coupling, modeled using the formulation of Saffman [1962], specifically through the application of Stokes drag, with the addition of viscosity variations due to particle concentration. The viscosity variation terms are derived from Govindarajan [2004]. The momentum balance and continuity equations for the fluid respectively are

$$\rho_f \left(\frac{\partial \mathbf{u_d}}{\partial t_d} + \mathbf{u_d} \cdot \nabla_\mathbf{d} \mathbf{u_d} \right) = -\nabla_\mathbf{d} p_d + \nabla_\mathbf{d} \left[\mu_d^{tot} \cdot \left(\nabla_\mathbf{d} \mathbf{u_d} + (\nabla_\mathbf{d} \mathbf{u_d})^T \right) \right] + KN \left(\mathbf{v_d} - \mathbf{u_d} \right), \quad (1)$$

$$\nabla_\mathbf{d} \cdot \mathbf{u_d} = 0, \quad (2)$$

while the particle suspension satisfies momentum balance and continuity respectively given by

$$mN \left(\frac{\partial \mathbf{v_d}}{\partial t_d} + \mathbf{v_d} \cdot \nabla_\mathbf{d} \mathbf{v_d} \right) = -KN \left(\mathbf{v_d} - \mathbf{u_d} \right), \quad (3)$$

$$\frac{\partial N}{\partial t_d} + \nabla_\mathbf{d} \cdot (N \mathbf{v_d}) = 0. \quad (4)$$

Here, the subscript d represents a dimensional variable, and ρ_f is the dimensional density of the fluid. The total dimensional viscosity $\mu_d^{tot} = \mu_f + \mu_p$, where μ_f is the dimensional viscosity of the fluid and μ_p is the contribution to viscosity due to the particles. m and $\tau = m/K$ are the mass and relaxation time of a spherical dust particle, N is their number density per unit volume. The quantity K is the drag coefficient given by $6\pi r \mu_f$ for a

sphere of radius r. The fluid velocity is given by $\mathbf{u} = (u_x, u_y, u_z)$, in the coordinate system shown in figure 1. The particles are assumed to be continuously distributed in the flow and to have a continuous velocity variation in space and time, and their dynamics may thus be described as a field, with $\mathbf{v} = (v_x, v_y, v_z)$. My analysis thus precludes situations of diverging number density and of particle collisions. The mass fraction of particles in the suspension is $f = mN/\rho_f = 4\pi N r^3 \rho_p / 3\rho_f$. The density of the solid making up the particles is ρ_p. Unless otherwise specified, I work in the limit of $\rho_p/\rho_f \to \infty$, so the volume fraction occupied by the particles is negligible. Non-dimensionalizing equations (1–4) with the channel-centerline velocity U_m, the half-channel width, H, and the viscosity μ_f of the fluid as scales, and with a mean dust mass-fraction profile

$$\bar{f}(y) = f_{max} \left[\exp\left\{ \frac{-(y-a_p)^2}{2\sigma^2} \right\} + \exp\left\{ \frac{-(y+a_p)^2}{2\sigma^2} \right\} \right], \tag{5}$$

with particles concentrated in two layers of thickness σ, but my numerical method is general and suitable for any desired particle concentration profile. The location a_p of the maximum in particle concentration is an important parameter. If the same particles were to be uniformly distributed across the channel, the loading would be $f_{ave} \simeq \sqrt{2\pi} f_{max} \sigma$. The Reynolds and Stokes numbers are given respectively by

$$R \equiv \frac{HU_m}{\mu_f/\rho_f} \qquad \text{and} \qquad S \equiv \frac{\tau}{\rho_f H^2/\mu_f} = \frac{2}{9}\frac{r^2}{H^2}\frac{\rho_p}{\rho_f}. \tag{6}$$

These two quantities, along with the thickness σ of the particle-laden layer, the mass loading for a given σ as measured by f_{max}, and the location a_p of the maximum in particle concentration, determine this problem.

0.1.2 Linear stability equations

After non-dimensionalising, we split all quantities into their basic and fluctuating parts, as $\mathbf{u} = \mathbf{U} + \hat{\mathbf{u}}$, $\mathbf{v} = \mathbf{U} + \hat{\mathbf{v}}$, $p = P + \hat{p}$, $f = \bar{f} + \hat{f}$ and $\mu^{tot} = \bar{\mu} + \hat{\mu}$. Here, a hat represents a perturbation quantity, while an upper case or overbar denotes a mean quantity. At steady state, the particles follow the flow field, meaning that the particle and fluid phases share the same mean velocity field, $\mathbf{U}$. In parallel shear flows, we have $\mathbf{U} = U(y)\mathbf{e_x}$, where $\mathbf{e_x}$ is a unit vector in the streamwise direction. The viscosity is non-dimensionalized by the viscosity of the pure fluid, μ_f. The mean viscosity is then described as $\bar{\mu} = 1 + \bar{f}/\gamma$, and the perturbation viscosity is $\hat{\mu} = \hat{f}/\gamma$, obtained from Einstein's viscosity formula for small particulate volume fraction. Here $\gamma = 0.4\rho_p/\rho_f$. In the limit of infinite γ, the dimensional viscosity remains at μ_f everywhere.

The perturbation quantities are linearised and written in normal mode form as

$$(\hat{\mathbf{u}}, \hat{\mathbf{v}}, \hat{f}, \hat{\mu}) = \frac{1}{2}\left[(\mathbf{u}(y), \mathbf{v}(y), f(y), \mu(y)) \exp\left\{i\alpha(x - ct) + i\beta z\right\} + \text{c.c.}\right]. \tag{7}$$

Squire's theorem applies here, allowing us to analyze two-dimensional systems that fully describe the exponential growth of perturbations. After appropriate elimination and reduction, the stability equations can be written in terms of the perturbation streamfunction $\psi(y)$ and the perturbation viscosity $\mu(y)$ as:

$$\begin{aligned}\left[(U_* - c)(D^2 - \alpha^2) - U_*''\right]\psi + D(J\bar{f}'\psi) = \frac{1}{i\alpha R}\Big[\bar{\mu}(D^2 - \alpha^2)^2 + 2\bar{\mu}'D^3 + \bar{\mu}''D^2 \\ - 2\alpha^2\bar{\mu}'D + \alpha^2\bar{\mu}''\Big]\psi + \frac{1}{R}\left[U'D^2 + 2U''D + U''' + \alpha^2 U'\right]\mu,\end{aligned} \tag{8}$$

and

$$-(U - c)\gamma\mu + \Big[- i\alpha RS\mathcal{M}^2 U'\bar{f}' + (\mathcal{M}\bar{f})'\Big]\psi = 0, \tag{9}$$

where

$$U_* \equiv U + J\bar{f}, \quad \mathcal{M} = \frac{1}{1 + i\alpha(U - c)SR}, \quad J = (U - c)\mathcal{M}, \tag{10}$$

$$[u_x, u_y, v_x, v_y] = \left[D\psi, -i\alpha\psi, \mathcal{M}u_x - (\mathcal{M}^2 SRU')u_y, \mathcal{M}u_y\right]. \tag{11}$$

The operator D is defined as $D = d/dy$, and a prime denotes a derivative in y of a mean quantity. The velocities can be expressed in terms of ψ using equations (11). The boundary conditions are:

$$\psi(y = \pm 1) = D\psi(y = \pm 1) = \mu(y = \pm 1) = 0. \tag{12}$$

For given mean flow $U(y)$ streamwise wavenumber α, base particle loading $\bar{f}(y)$, particle to fluid density ratio, and fixed Reynolds and Stokes numbers, equations 8 to 12 define an eigenvalue problem, which yields a spectrum of eigenvalues c and corresponding eigenfunctions, $(\psi(y), \mu(y))$. If even one eigenvalue has a positive imaginary part, i.e., $c_{im} > 0$, we have an exponential growing mode.

In the Orr-Sommerfeld equation, the stability equation for a clean fluid, it is seen that the highest, i.e., fourth-order, derivative term in y is scaled by the inverse of the Reynolds number. Now, even if the Reynolds number approaches infinity, this term may not be dropped, because if it is, we will not be able to satisfy all four boundary conditions associated with the equation. This is thus a classical singular perturbation problem [Van Dyke, 1964], where the highest derivative term becomes as big as the terms on the left-hand side in some portions of the flow. There are two layers [Lin, 1945a,b, 1946] where viscous effects are important and gradients are large: the wall layer, of thickness $\epsilon_w \sim R^{-1/2}$, and the critical layer, of thickness $\epsilon \sim R^{-1/3}$. It is the critical layer which is of primary interest to us to explain the mechanism of the particle-driven instabilities we

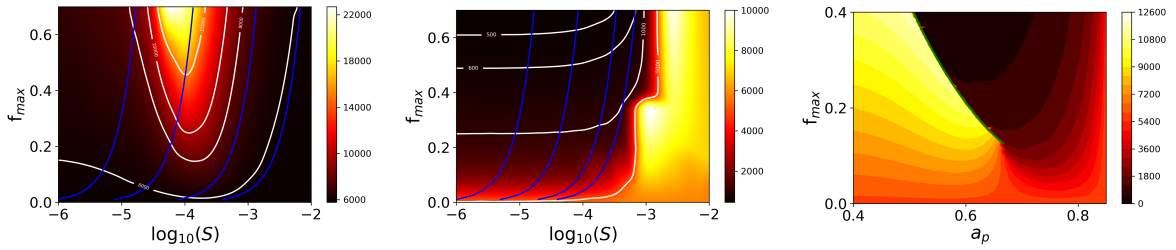

(a) (b) (c)

Figure 2: Phase plot of the critical Reynolds number, shown in colour, in (a) and (b) as a function of the Stokes number S and the particle loading strength f_{max}, and in (c) as a function of the particle loading location a_p, and f_{max}. (a) A case where there is no overlap mechanism in operation, with $a_p = 0.40$, and (b) where it is in operation, with $a_p = 0.75$. Note the difference in the colourbars in the two figures. In both figures $\sigma = 0.1$, and the blue lines represent curves of constant particle number density N. The value of N decreases from left to right, with the non-dimensional quantity $9\sqrt{2}H^3N\sqrt{\rho_f/\rho_p}$ being $[1.00 \times 10^7, 4.42 \times 10^5, 1.40 \times 10^4,$ and $1.25 \times 10^3]$ for plot (a), and $[1.00 \times 10^7, 8.94 \times 10^5, 1.12 \times 10^5,$ and $3.95 \times 10^4]$ for plot (b). The other parameters in (c) are the same as in Figure(5). The green curve serves as a visual guide for observing the sharp change in the critical Reynolds number due to a change in the mode of instability. Some jitter in the colours is visible, and is due to the interpolation of results on a finitely spaced grid.

find. This is a thin region centered around the critical point y_c within the channel, where $U(y_c) = c$, and perturbation kinetic energy is produced primarily within this layer.

We employ the Chebyshev spectral collocation method to discretize the system given by equations 8 to 12 at $n = 81, 121, 141, 161$ discrete points in the domain and solve them using the LAPACK FORTRAN package.

0.1.3 Summary of results

The response of the flow to non-uniform particle loading may be divided into two broad categories that we term overlap and non-overlap conditions. Under non-overlap conditions, the particle-laden layer lies at some distance from the critical layer, and particles do not significantly alter this process. However, when there is an overlap between these layers, there is a dramatic alteration of stability behaviour, with two modes of instability apart from the TS mode appearing. The fundamental difference between overlap and non-overlap conditions is starkly visible in Fig. 2 . Though these modes have been observed in one older study [Rudyak et al., 1997] at constant viscosity, they had not been explained before, to my knowledge. The shortwave overlap mode occurs at much lower Reynolds number than the TS mode, and supports wavelengths of the order of the channel width, see Fig.3 . The longwave overlap mode appears over a wide range of Reynolds numbers and supports wavelengths which could be as small as the channel width but become longer and longer

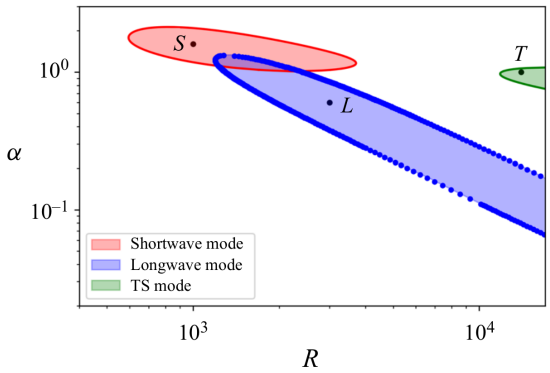

Figure 3: The three distinct modes of instability, shown by the shaded regions. A specific choice of parameters is made here, where overlap conditions prevail: the peak of the mean particle concentration profile has an amplitude $f_{max} = 0.70$, and is positioned at $a_p = 0.75$. The thickness of the particle-layer is $\sigma = 0.1$ and the Stokes number is $S = 8 \times 10^{-4}$. This figure is representative of a wide range of parameters under overlap conditions. The points marked S, L, and T are representative of shortwave, longwave and Tollmien-Schlichting modes respectively, and will be elaborated on.

with increasing Reynolds number. This mode is unusual because its wall-normal velocity perturbation is antisymmetric (odd) about the channel centerline. In the classical, clean channel flow, the primary instability corresponds to the symmetric (even) TS mode. Odd modes are generally more stable and do not lose stability first, and therefore they are not the modes that normally govern the onset of transition. The three modes of instability show regimes of distinct existence, and go through interesting intersections and mergers with changes in parameters.

In the critical layer the perturbation velocity may be expanded as $u_y = \sum_{n=0}^{\infty} \epsilon^n u_{y,n}(\xi)$, with $\xi = (y - y_c)/\epsilon \sim 1$, $D_\xi = d/d\xi$, and $\epsilon = (\alpha R)^{-1/3} \ll 1$. I derive the lowest-order equations in the critical and wall layers as

$$\left[(1+\bar{f})\xi U_c' D_\xi^2 + i\frac{1}{\alpha R \epsilon^3} D_\xi^4 - \frac{\epsilon}{\sigma} U_c' (D_\chi \bar{f})(I - \xi D_\xi)\right] u_{y,1} = 0, \tag{13}$$

(14)

$$\left[-c\left(1 + \frac{\bar{f}}{1 - i\alpha c S R}\right) D_\xi^2 + i\frac{1}{\alpha R \epsilon_w^2} D_\xi^4 - \frac{\epsilon_w}{\sigma}\left(\frac{c D_\chi \bar{f}}{1 - i\alpha c S R}\right) D_\xi\right] u_{y,1} = 0, \tag{14}$$

where $\epsilon_w = (\alpha R)^{-1/2}$, (with subscripts 'w' and 'c' referring to wall and critical layers respectively) for particulate parallel shear flow for dilute particle loading, and show how they differ fundamentally from the classical equations for clean flow. This is combined with an energy-budget analysis which brings out the consequences for stability. The reason for the existence of two categories of behaviour is shown to lie in the dynamics within the critical layer. Variations in the base particle concentration within the critical layer significantly alter the production of disturbance kinetic energy. We note that despite the

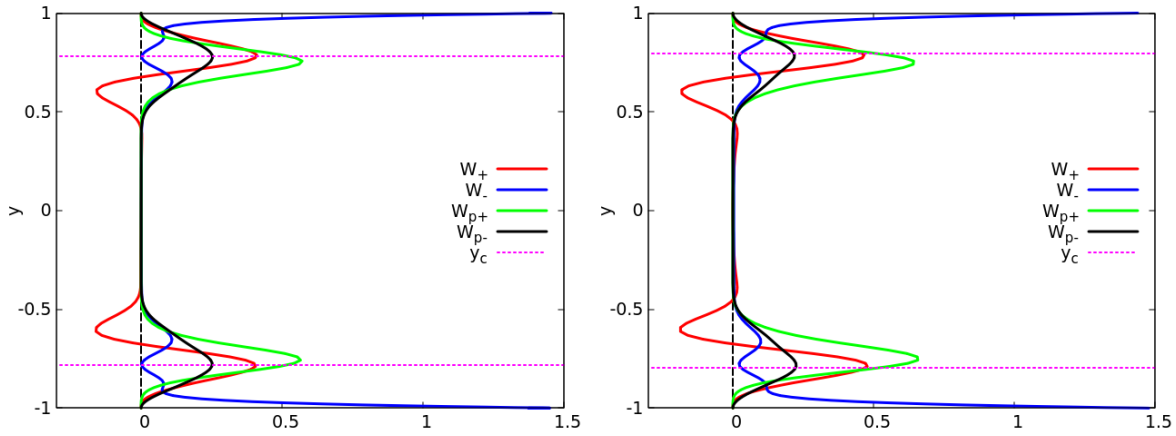

(a) (b)

Figure 4: Comparison of contributions to the energy budget in the longwave (odd) mode (a) at point 'L' in figure 3, where $R = 3000$ and $\alpha = 0.6$, with that of the shortwave (even) mode (b) at point 'S' in figure 3, i.e., $R = 1000$ and $\alpha = 1.6$. In both, $f_{\max} = 0.70$, $\sigma = 0.1$, $S = 8 \times 10^{-4}$, and $a_p = 0.75$. Both of these modes are unstable, with net production beating dissipation by a small amount.

marked differences in the symmetry of the eigenstructures and the regime of exponential growth between the two overlap modes S and L, they exhibit nearly identical energy budgets, as shown in Fig.(4). This similarity underscores the significance of concentration variations within the critical layer in driving instability. The wall layer is seen not to be a major player, see Fig. 5. The lowest-order physics everywhere in the flow may be obtained from a minimal composite equation

$$\left[(U_* - c)(D^2 - \alpha^2) - U''\right]\psi - (J'\bar{f}')\psi + (J\bar{f}')D\psi = \frac{1}{i\alpha R}D^4\psi, \tag{15}$$

which contains all the terms in the complete stability equations which contribute at the leading order somewhere in the flow, i.e., in the outer, critical or wall layers. The wall layer contributes no additional terms not present in the other two. The minimal composite equation is shown (see Figure 5a) to contain the essential physics of the overlap instabilities, in terms of trends in the critical Reynolds number and indeed in the eigenfunction behaviour.

In the limit of heavy particles, the volume loading is negligible, so the viscosity is constant. I then consider finite particle to fluid density ratios, where the volume loading is finite but small. Now viscosity varies with particle concentration. The change in the mean flow velocity profile effects a significant stabilisation as shown in Fig.6 whereas the explicit viscosity gradient terms are shown to be non-players in this case. Whether this is a consequence of the special viscosity profile that this loading produces, is being examined in the following section, and hopefully will be answered in the thesis.

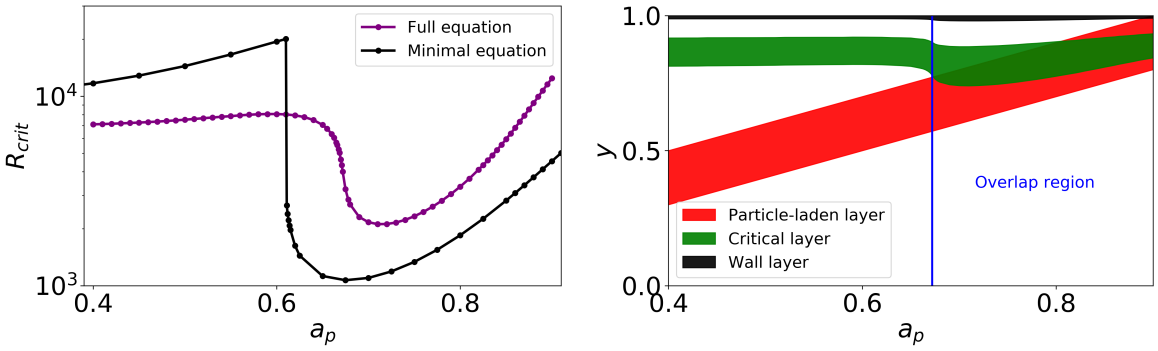

(a) (b)

Figure 5: With a specified amplitude of $f_{max} = 0.1$, a peak width of $\sigma = 0.1$ for the mass fraction profile, and a Stokes number of $S = 2.5 \times 10^{-4}$, the purple curve and the black curve in (a) illustrate the critical Reynolds number as a function of the position of the peak, a_p of the mass fraction profile for the full equation (8) without viscosity terms and the minimal equation (15) respectively. The green, black, and red bands in (b) illustrate the notional critical layer, the wall layer, and the particle-laden layer, respectively, as they vary with a_p.

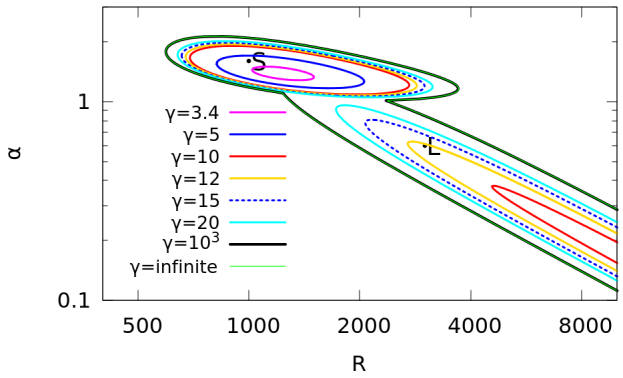

,

Figure 6: Neutral boundaries of the shortwave and longwave modes of instability for various density ratios $\rho_p/\rho_f = 2.5\gamma$. All other parameters are as in figure 3, where we had $\gamma \to \infty$.

0.1.4 The stability of channel flow with non-uniformly distributed dust particles under the influence of gravity

This problem is an extension of the previous one, with the additional consideration of gravity. Particles which are not neutrally buoyant settle toward the bottom or top wall when their density is greater or less than that of the fluid, respectively. We assume the Froude number, defined as $Fr = U_0/\sqrt{gH}$, where U_0, g, and H represent the centerline velocity, gravitational acceleration, and half-channel width, respectively, is much greater than 1. At high Froude numbers, gravitational effects on the fluid momentum equations become negligible, and particle settling is slow. As a result, change in the mass fraction and velocity profiles occur over long timescales. In instability analysis, we focus on much shorter timescales, during which the mass fraction and velocity profiles can be considered unchanged. This enables the base flow to be considered quasi-steady for stability analysis, with gravitational effects influencing the stability problem solely through the mean mass fraction profile. The mean mass fraction of the particles now follows

$$\bar{f} = 0.5 f_{max} \left[1 + \tanh\left(\frac{y - a_p}{\sigma} \right) \right]. \tag{16}$$

The particle concentration is zero far from the wall and increases to f_{max} near the wall, with the transition occurring around $y = a_p$ within a band of width 2σ. A schematic of the steady state of the problem is given in Figure (1b). The added mass term is now included in the particle equation, so the linearized equations differ from those for the above study. However, I find that this term has a minimal impact on stability.

We had seen above that the viscosity introduced by the suspension of particles has a stabilizing effect. However, in this case, I find that the particle-induced viscosity has the opposite effect on flow stability. I analyze that the origin of the instability is the alteration in mean velocity U caused by particle-induced viscosity. To understand how the viscosity causes destabilization, I compared the results with those of a one-peak Gaussian-shaped mass fraction profile, $\bar{f} = 0.5 f_{max} \left[\tanh\left(\frac{y-a_{p_1}}{\sigma} \right) - \tanh\left(\frac{y-a_{p_2}}{\sigma} \right) \right]$, inspired by the problem in Section 0.1. I began with a set of parameters that preserved the instability modes present in Figure 3 and gradually shifted the peak of the mass fraction profile toward a wall to obtain a similar profile to what I have in this gravity case. The destabilization is driven by changes in the mass fraction profile, as illustrated in Figure (7).

Further analysis reveals that the mass fraction profile has little direct impact through the additional stratification terms, but it modifies stability majorly by altering the mean velocity profile. As a result, the instability is primarily driven by the mean viscosity profile, which exhibits higher viscosity near the wall. As explained by [Ranganathan and Govindarajan, 2001, Govindarajan, 2004], the key mechanism is that a positive viscosity gradient, with higher viscosity near the wall compared to the inner channel, induces a

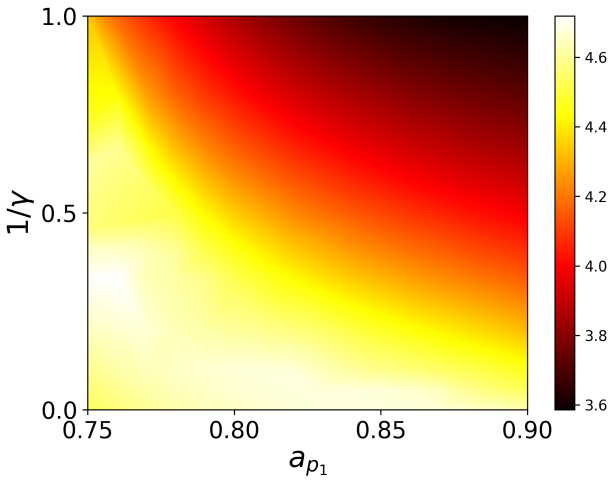

Figure 7: The parameters used are $f_{max} = 0.903$, $S = 8 \cdot 10^{-4}$, $\sigma = 0.0968$, and $a_{p_2} = a_{p_1} + 0.2$. The color scale represents the base-10 logarithm of the critical Reynolds number. For a fixed a_{p_1}, the critical Reynolds number initially increases with the induced viscosity ($\propto 1/\gamma$), reaches a peak, and then decreases. At a fixed induced viscosity, it initially decreases as a_{p_1}, the location of the rising arm of the mass fraction, shifts towards the wall, reaching a minimum before increasing again and asymptotically approaching the critical Reynolds number of the clean flow.

destabilizing effect, while a negative gradient promotes stabilization. The origin of this low Reynolds number instability mode can be traced to the tendency of the velocity profile to develop an inflection point. At low Reynolds numbers, this leads to a different lowest-order governing equation than the one derived for the overlap mechanism for the earlier case [Kumar and Govindarajan, 2024b], resulting in the observed instability modes.

0.2 The stability of channel flow with slightly converging walls

0.2.1 Description of the system

The laminar flow through channels whose walls converge or diverge at a constant angle is described by the Jeffery-Hamel (JH) equations (Jeffery [1915], Hamel [1917]). Eagles [1966] calculated the critical Reynolds number, R_{crit}, at which the first linear instability is seen, for diverging channel flow. They noticed that R_{crit} falls steeply compared to that in a straight channel. For a straight channel, $R_{crit} = 5772.2$ (see Orszag [1971]) whereas with a wall divergence of only 0.04 degree, $R_{crit} \sim 2000$. Note that this divergence is so small that a channel built with such a divergence would be indistinguishable visually from a straight one. The reason for this sharp fall is an open question, with some beginnings having been made by Swaminathan et al. [2011]. On the other hand are channels with a

small angle of convergence. The stability of this flow, to my knowledge, was first studied by Fujimura [1982]. A sharp increase in the critical Reynolds number with the smallest convergence was seen. The sensitivity to convergence angle is even more stark than to divergence.

The Jeffery-Hamel (JH) equation provides the steady state of two-dimensional laminar flow of an incompressible fluid within an infinite wedge, driven by a source/sink located at the intersection of the rigid planes forming the wedge, a schematic is shown in Figure 8 .

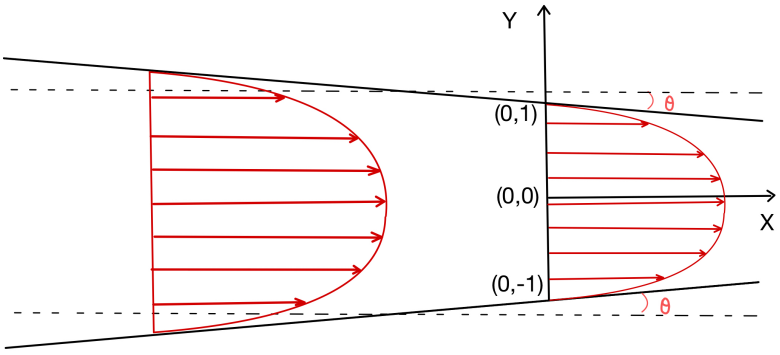

Figure 8: Schematic illustrating a convergent channel flow with a Type III_1 velocity profile. I emphasise that the angle of convergence is grossly exaggerated for clarity of viewing, compared to the range I study here. The x-axis is oriented along the channel centerline and the y-axis intersects the channel walls at an angle of $\pi/2 - \theta$. The lengths are non-dimensionalized using the local half-channel width H, placing the walls at $y = \pm 1$. Note that θ is negative.

It is a similarity equation given by

$$U''' + 2S_0 UU' + 4\theta^2 U' = 0, \tag{17}$$

with the boundary conditions

$$U(+1) = U(-1) = 0; \quad U(0) = 1, \tag{18}$$

where U is the streamwise velocity nondimensionalised by the centerline velocity U_m. The angle made by the rigid walls with respect to the channel centerline (the x-axis) is denoted by θ, as illustrated in Figure(8). An important parameter in this problem is $S_0 \equiv \theta R$. Note that in convergent flow, θ, and therefore S_0, are negative. The Reynolds number $R \equiv \frac{|Q|}{\nu}$, where $Q = U_m(x_d)H(x_d)M_U$ is the net mass flux through the channel, where $H(x_d)$ is the local channel half-width, or the distance of the wall from the centerline, and ν is the kinematic viscosity. The non-dimensional mass flux is given by $M_U = \int_{-1}^{+1} U(y)dy$. For a constant tilt angle, we may approximate flow in the convergent channel to that going towards a sink at a location x_L, which lies extremely far downstream, so $H = (x_L - x_d)\tan|\theta|$ and $U_m \propto 1/H$. A prime denotes a derivative

with respect to a similarity coordinate y, which is the coordinate normal to the centerline non-dimensionalized by $H(x)$. Given that the net mass flux must be constant through all x, the Reynolds number too is constant throughout. It will become useful to define another Reynolds number, $R_{SC} = U_m(x)H(x)/\nu$. The Reynolds numbers are related as $R = R_{SC}|M_U|$.

Numerically, I get the mean velocity U by solving the equations (17,18), with an initial guess for $U''(0)$, and iterating by the Newton-Raphson method until the boundary conditions are met. A few of the computed velocity profiles are illustrated in Figure 9 . The stability analysis is carried out as described before, and the relevant equation is

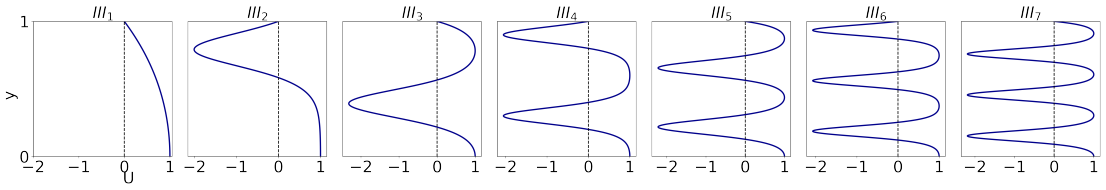

Figure 9: Laminar velocity profiles of type III_n for $n = 1$, 2, 3, 4, 5, 6, and 7. The top half of the profiles are shown. The Reynolds number is 100, and the angle $\theta = -0.6^{\circ}$.

simply the Orr-Sommerfeld.

0.2.2 Summary of results

My basic aim has been to show why an extremely small angle of wall convergence can drastically and fundamentally change the flow through a two-dimensional channel. The answer lies in a fundamental shift in the dynamics of the critical layer. For the one-lobed profile of type III_1, I have obtained the lowest-order equation (19)

$$\left[-\frac{iU_c'\xi}{\epsilon}D_\xi^2 - U_c'' - \frac{1}{i\alpha R\epsilon^4}D_\xi^4\right]\psi_0 = 0. \tag{19}$$

in the critical layer, where $\epsilon = (-\alpha S_0 R)^{-1/4}$, following the traditional approach. I have shown how the dominant (lowest-order) balance in the critical layer is altered fundamentally by convergence, with the second derivative of the velocity profile entering the balance at even very low angles of convergence and ousting out the inviscid term which normally balances the dominant viscous effect.

This study also reveals that at small Reynolds numbers, of $O(10)$, we can have multiple stable laminar flow solutions through convergent channels, which is shown in Fig. 10 . Since multiple velocity profiles are stable at low Reynolds number, they can all, in principle, be observed experimentally. The ease of experimentally obtaining a given profile, will however, depend on the size of its basin of attraction in phase space and the ability to access that basin.

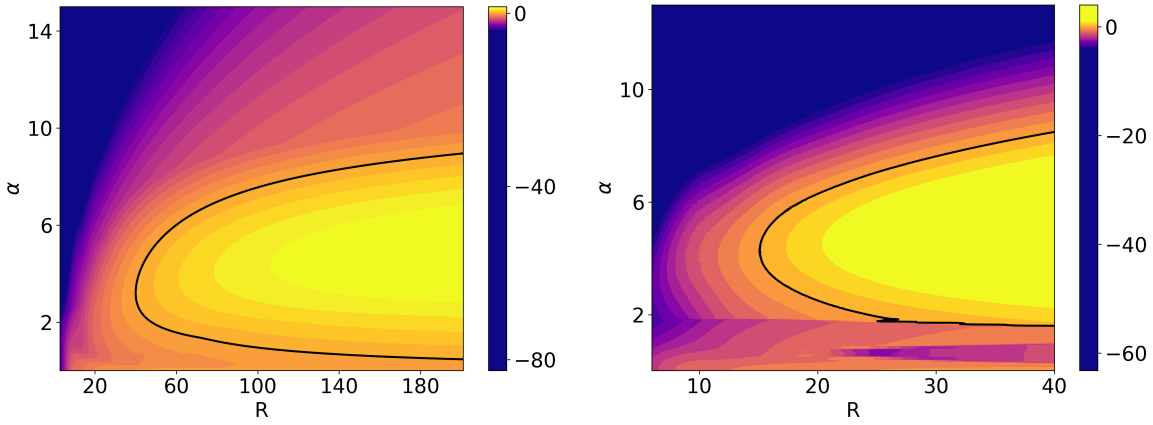

(a) (b)

Figure 10: The instability growth rate (indicated by color) is presented for velocity profiles of type III_2 and III_3 in (a) and (b) respectively, as a function of perturbation wave number α and Reynolds number R. The black line denotes the neutral curve. The wall convergence angle θ is -0.6^o.

Chapter 1

Introduction

The instability of a clean fluid through a straight channel has been a topic of interest for many decades. In this thesis I study two departures from this flow: of dusty flow through a straight channel, and of clean flow through a convergent channel. Due to each of these departures, remarkable changes in stability occur.

The dynamics of fluids laden with suspended particles has been a subject of investigation for decades. When the particles are extremely small and in great number, the term "dusty flow" is appropriate. Dusty shear flows are ubiquitous: occurring in environmental phenomena like dust storms, snow avalanches and sediment transport in rivers, and in industrial processes like the manufacture of fertilizers and various powders. Whether such a flow will be laminar, turbulent or in an unsteady transitional state is of great interest for a variety of reasons, and the first step is to study the stability of the laminar base state. The study of the onset of instability in a laminar flow, which often leads to turbulence, provides valuable insights into the turbulent state.

To discuss the second departure, namely the effect of geometry, we know that it is extremely difficult to manufacture a pipe or channel that is perfectly straight. Now a small departure from being absolutely straight has a profound effect on stability, this feature should therefore be taken into consideration while drawing conclusions about the transition to turbulence. I explore the stability of shear flow under the parallel flow approximation. For decades, shear flows have thrown up surprises in their stability behaviour, and the different mechanisms of instability, though not easy to predict, are crucial to unravel. I address the following problems:

- The stability of channel flow with non-uniformly distributed dust particles.
- The stability of channel flow with non-uniformly distributed dust particles under the influence of gravity.
- The stability of channel flow with slightly converging walls.

While these systems may appear similar, they are fundamentally distinct and exhibit significantly different stability behaviours. Despite these differences, they share common underlying physics, as their stability is governed by critical-layer dynamics, which I have demonstrated in my studies.

We conduct linear stability analysis of steady-state flows. This analysis involves examining the eigenspectrum of linearised governing equations to understand both modal and non-modal stability characteristics. In modal stability, perturbations either grow or decay exponentially over time, leading to instability or stability, respectively. Non-modal stability, on the other hand, considers transient algebraic growth of perturbations, even if they ultimately decay exponentially over long timescales. When this transient growth becomes sufficiently large, despite all eigenvalues indicating eventual decay, nonlinear effects can take over and destabilize the flow, a phenomenon known as subcritical transition. Although my thesis focuses exclusively on modal stability, our findings provide valuable insights and potential directions for future investigations into non-modal stability.

The stability equation of parallel shear flow was first given by Orr [1907] and Sommerfeld [1909] independently. The equation appears as a generalized eigenvalue problem $AX = cBX$ where A and B are the linear operators, X and c are the eigenfunction and the eigenvalue respectively. This involves a fourth-order homogeneous differential equation, which remains challenging to solve analytically and requires a good computational scheme, such as the pseudo-spectrum method, to numerically solve this stiff equation. The first semi-analytical solution, specific to boundary-layer flow, was provided by Tollmien [1930], with experimental validation following later by Schubauer and Skramstad [1947]. Orszag [1971] subsequently provided accurate numerical results for plane channel flows. Despite the early establishment of the Orr–Sommerfeld equation, its solutions remain difficult to obtain, with progress in the field often spanning decades. The challenge lies in the singular perturbation nature of the problem, where viscosity introduces singularities in viscous flow stability.

In the absence of viscosity, the problem reduces to that of inviscid flow stability, governed by the Rayleigh equation formulated in 1880. Several theorems guide the analysis of inviscid flow stability. For instance, the Rayleigh inflexion-point theorem states that instability is possible only if the velocity profile has at least one inflexion point. Fjørtoft extended this condition, asserting that the velocity profile must have an inflexion point coinciding with a vorticity maximum for instability to occur. Additionally, Howard's semicircle theorem constrains the complex phase speed of perturbations within a semicircular region in the complex plane. While these theorems provide valuable insights into inviscid stability, similar results for viscous flows remain elusive. Nonetheless, inviscid results often inform viscous stability analyses. For example, velocity profiles with inflexion points often exhibit inviscid instabilities even in viscous flows, and Howard's semicircle

theorem provides a broad guideline for phase speeds, and helps filter unphysical modes in numerical solutions of the Orr–Sommerfeld equation. In the case of pressure or gravity-driven channel flow of a single clean viscous fluid, the velocity profile lacks inflexion points, implying stability under inviscid conditions. Of course we may not apply theorems derived for inviscid flow directly to the viscous problem. Historically, it was believed that viscosity would only have a stabilising effect across all Reynolds numbers due to its dissipative nature. However, this assumption was disproved when it was shown that laminar channel flow is linearly stable only up to a critical Reynolds number R=5772.2 and unstable thereafter, though it contains no inflexion point and is inviscidly stable. This discrepancy arises because viscosity exhibits dual effects: it dissipates perturbation energy, which has a stabilizing effect, but also contributes to perturbation energy production, which can be destabilizing. In channel flows, dissipation predominantly occurs near the walls due to maximum wall resistance, while perturbation energy production is significant in the critical layer, a region centered around a critical point y_c where the perturbation phase speed matches the mean flow velocity. As the Reynolds number increases, production in the critical layer surpasses wall dissipation, leading to instability. Thus, the critical layer dynamics govern the onset of instability. Lin [1945a,b, 1946] was the first to propose a theory for channel flow instability based on critical layer dynamics. His asymptotic theory provided a scaling law for the critical layer thickness and a simplified equation capturing its behavior. My work builds on Lin's framework and extends it to explore novel mechanisms of instability in three problems of interest. Specifically, I have examined how critical layer dynamics, differing from Lin's original theory, drive instabilities in cases involving dust particles and wall tilts. Dust particles in channel flows are often non-uniformly distributed due to inertial migration (e.g., Segre and Silberberg [1961, 1962]; Ho and Leal [1974]). While earlier studies assumed uniform particle distributions, which primarily have a stabilizing effect, our findings reveal significant destabilization caused by non-uniform distributions. The magnitude and location of clustered particles play critical roles, and particle viscosity introduces complex effects: slight stabilization in the absence of gravity but destabilization when gravity is considered. Wall tilts or convergent/divergent channel geometries further complicate the flow dynamics. These flows, known as Jeffery–Hamel flows, possess infinitely many steady-state profiles categorized into five types by Fraenkel and Squire [1962]. Although most of these profiles are unstable and seldom observed experimentally, our study identifies at least three stable velocity profiles at low Reynolds numbers.

This thesis explores these intricate stability mechanisms, emphasizing critical layer dynamics and their modulation by dust particle distribution, wall tilts, and other flow configurations. These findings contribute to a better understanding of shear flow instability.

Chapter 2

Mechanism of instability in non-uniform dusty channel flow

This work presented in this chapter has been published in our *Journal of Fluid Mechanics* article Kumar and Govindarajan [2024b].

2.1 Introduction

Saffman [1962] was the first to propose a formulation for the stability of a pressure-driven laminar channel flow, of a fluid containing dust particles in dilute suspension. The dust particles were uniformly distributed across the channel width. Subsequently, Michael [1964] conducted numerical computations, validating the conclusions of Saffman [1962]. Isakov and Rudnyak [1995] extended the study of Michael [1964] with improved numerical accuracy. Boronin and Osiptsov [2008] studied uniform particle loading with a finite volume fraction modeled by a corrected Stokes drag including the effects of viscosity variations due to perturbations in particle concentration, and found destabilization compared to the dusty-gas results of Isakov and Rudnyak [1995]. In a later study, Klinkenberg et al. [2011] noted that the critical Reynolds number increases to high levels with strengthening of loading in a uniform particle distribution. Nevertheless, at a Reynolds number of a few thousand, loading of particles can enhance the transient growth for three-dimensional perturbations. Nath et al. [2024] found that in simple shear flow, non-uniformly distributed particles destabilize the flow through an inviscid mechanism. This is in contrast to our system of plane channel flow, where we show that destabilization is by a viscous mechanism.

Small particles suspended in channel or pipe flow normally do not occur with uniform probability everywhere [Matas et al., 2004]. They tend to concentrate in certain relatively thin regions of the flow. The location of concentration depends on different flow and loading conditions, and examples are available in the experiments of Snook et al. [2016]. The early experiments of Segre and Silberberg [1961, 1962] showed that particles, when

homogeneously distributed in a pipe, undergo inertial cross-stream migration, caused by lift forces and the wall, and tend to accumulate within an annular region, located at a certain radial distance. Saffman [1965] calculated the lift force for a small solid particle in unbounded linear shear. Cox and Brenner [1968] included considerations of the wall, and of shear variation. The review of Cox and Mason [1971] provides the equilibrium radial variation of particle concentration in a range of conditions in a pipe. For two-dimensional channel flow, studied here, Ho and Leal [1974] offered the first theoretical explanation for non-uniform particle loading, due to the wall-induced lift force and the shear-gradient lift force. For neutrally buoyant particles, they found two equilibrium points: an unstable point at the channel centerline and stable points located ± 0.6 times the half-channel width from the center. Their calculations were for creeping flow in the channel, namely for channel Reynolds number $R \ll 1$, as well as the particle Reynolds number Re_p being significantly smaller than R. Schonberg and Hinch [1989], Asmolov [1999] revealed a wallward shift of the stable equilibrium points for increasing R. For particles of a finite size relative to the channel width, Anand and Subramanian [2023] found an additional equilibrium point closer to the centerline.

Thus an inhomogeneous equilibrium particle distribution with a relatively thin particle-containing layer is natural in channel flow, though its location depends on several factors. The question is whether this arrangement remains stable to an accumulation of particles, or whether such accumulation, when sufficiently high, can cause the laminar flow to undergo instability. We adopt a gaussian particle distribution profile to model experimental observations and theoretical findings. Following the findings of Klinkenberg et al. [2011] and the calculations of many, we may take the lift force at the equilibrium location, on a sufficiently small particle, to be negligibly small compared to the Stokes drag.

Rudyak and Isakov [1996], Rudyak et al. [1997] investigated the effects of inhomogeneous gaussian particle loading and found low Reynolds number instabilities of the kind we discuss here. A channel loaded with particles where particle concentration tapers off towards the walls was shown by Boronin [2009] to support instability at zero Reynolds number. Incidentally we found the instabilities of Rudyak and Isakov [1996], Rudyak et al. [1997] independently, since we only learned about that work recently. They noticed that the critical layer lies close to the particle-laden layer in these instabilities, but did not provide the mechanism which generates the new instabilities. The mechanism is the subject of the present chapter. Along the lines of the famous classical derivation of Lin [1945a,b, 1946] for a clean fluid, we derive the critical-layer and wall-layer equations for dusty parallel shear flow. The critical layer equations make it obvious how the inhomogeneity of particle loading enters the leading-order physics. We derive a minimal composite equation containing all the leading-order terms and show that it contains the essential overlap physics. Our energy budget study and the eigenfunctions support our findings, and directly

show how production of perturbation kinetic energy is altered in the critical layer. Our study demarcates two distinct classes of stability behaviour: one where the critical layer overlaps the layer where the particle concentration is non-constant, and another where the two layers lie away from each other. Two modes of overlap instability occur in the former.

Incidentally the earlier study on inhomogeneous particle loading only briefly mentions the numerical method, but provides no details of the discretisation, or the level of accuracy of the solutions. In order to achieve reasonable accuracy, we find that a high grid-resolution is needed within the particle-laden layer.

Introducing particles into the flow exacerbates the complexity of the transition to turbulence [Mueller et al., 2010]. Matas et al. [2003a,b], in pipe flow experiments, observed that adding particles at a significant volume fraction can delay or advance the transition to higher or lower Reynolds number, based on whether the particles are extremely small or somewhat larger, with a minimum in the transition Reynolds number being attained at a particular volume fraction. Numerical and experimental studies conducted by Matas et al. [2003a], Yu et al. [2013], Lashgari et al. [2014], Wen et al. [2017] demonstrate that transition to turbulence occurs smoothly, with velocity and pressure fluctuations increasing gradually. This suggests that particles can alter the nature of the transition and the resulting turbulence state.

Whether or not the transition occurs due to exponentially growing modes, the first step in understanding the transition to turbulence is to understand the mechanism causing linear stable and unstable eigenmodes to exist. We conduct this study below.

2.2 The governing equations and their solution

2.2.1 Description of the system

We investigate here a dilute suspension of particles in a pressure-driven channel flow, a schematic of which is shown in figure 2.1. The impact of this suspension on the flow is characterized by a two-way coupling, modeled using the formulation of Saffman [1962], specifically through the application of Stokes drag, with the addition of viscosity variations due to particle concentration. The viscosity variation terms are derived from Govindarajan [2004]. The particulate suspension is treated as a continuous medium whose dynamics is describable by a field equation. The momentum balance and continuity equations for the fluid respectively are

$$\rho_f \left(\frac{\partial \mathbf{u_d}}{\partial t_d} + \mathbf{u_d} \cdot \nabla_\mathbf{d} \mathbf{u_d} \right) = -\nabla_\mathbf{d} p_d + \nabla_\mathbf{d} \left[\mu_d^{tot} \cdot \left(\nabla_\mathbf{d} \mathbf{u_d} + (\nabla_\mathbf{d} \mathbf{u_d})^T \right) \right] + KN \left(\mathbf{v_d} - \mathbf{u_d} \right), \tag{2.1}$$

$$\nabla_\mathbf{d} \cdot \mathbf{u_d} = 0, \tag{2.2}$$

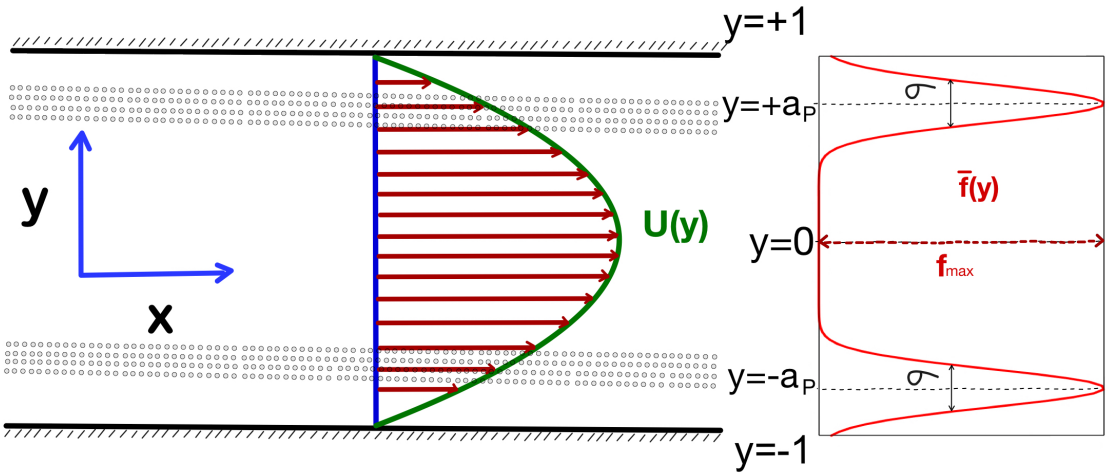

Figure 2.1: Schematic of the flow under consideration. The walls are situated at $y = \pm 1$, with the green curve and red arrows representing the mean velocity profile, $U(y) = 1 - y^2$. The particles are concentrated around $y = \pm a_p$ within a band of size σ. The mean particle mass fraction, $\bar{f}$, given by equation (2.6) is depicted on the right. Note that the volume fraction that heavy particles occupy will be much less.

while the particle suspension satisfies momentum balance and continuity respectively given by

$$mN\left(\frac{\partial \mathbf{v_d}}{\partial t_d} + \mathbf{v_d}\cdot\nabla_{\mathbf{d}}\mathbf{v_d}\right) = -KN\left(\mathbf{v_d} - \mathbf{u_d}\right), \tag{2.3}$$

$$\frac{\partial N}{\partial t_d} + \nabla_{\mathbf{d}}\cdot\left(N\mathbf{v_d}\right) = 0. \tag{2.4}$$

Here, the subscript d represents a dimensional variable and ρ_f is the dimensional density of the fluid. The total dimensional viscosity $\mu_d^{tot} = \mu_f + \mu_p$, where μ_f is the dimensional viscosity of the fluid and μ_p is the contribution to viscosity due to the particles. m and $\tau = m/K$ are the mass and relaxation time of a spherical dust particle, N is their number density per unit volume. The quantity K is the drag coefficient given by $6\pi r\mu_f$ for a sphere of radius r. We establish the x-axis to be aligned with the channel centerline, the y-axis to be oriented in the wall-normal direction, and the z-axis to be oriented perpendicular to the plane of the figure. The fluid velocity is given by $\mathbf{u} = (u_x, u_y, u_z)$. The particles are assumed to be continuously distributed in the flow, and to have a continuous velocity variation in space and time, and their dynamics may thus be described as a field, with $\mathbf{v} = (v_x, v_y, v_z)$. Our analysis thus precludes situations of diverging number density and of particle collisions. The mass fraction of particles in the suspension is

$$f = mN/\rho_f = \frac{4\pi N r^3}{3}\frac{\rho_p}{\rho_f}. \tag{2.5}$$

The density of the solid making up the particles is ρ_p. Unless otherwise specified, we assume a small particle volume fraction $f/(\rho_p/\rho_f)$ and a large density ratio ρ_p/ρ_f. In Section 2.5, however, we will instead vary the density ratio to control the volume fraction. In practical experiments, since the density ratio is finite, the volume fraction is typically controlled by adjusting the mass fraction or the particle number density. We non-dimensionalize equations (2.1-2.4) using the channel-centerline mean velocity U_m (i.e., the steady-state fluid velocity at the center of the channel), the half-channel width, H, and the viscosity μ_f of the fluid as scales. In dimensionless coordinates, the channel walls are positioned at $y = \pm 1$, with the suspended particles concentrated in around $y = \pm a_p$. We prescribe a mean dust mass-fraction profile

$$\bar{f}(y) = f_{max}\left[\exp\left\{\frac{-(y-a_p)^2}{2\sigma^2}\right\} + \exp\left\{\frac{-(y+a_p)^2}{2\sigma^2}\right\}\right], \tag{2.6}$$

with particles concentrated in two layers of thickness σ, but our numerical method is general and suitable for any desired particle concentration profile. The location a_p of the maximum in particle concentration is an important parameter. If the same particles were to be uniformly distributed across the channel, the loading would be given by

$$f_{ave} = \frac{\int_{-1}^{+1} \bar{f}(y;\sigma,a_p)dy}{\int_{-1}^{+1} dy} \simeq \sqrt{2\pi} f_{max}\sigma. \tag{2.7}$$

The Reynolds and Stokes numbers, which will emerge out of the non-dimensionalisation, are given respectively by

$$R \equiv \frac{HU_m}{\mu_f/\rho_f} \qquad \text{and} \qquad S \equiv \frac{\tau}{\rho_f H^2/\mu_f} = \frac{2}{9}\frac{r^2}{H^2}\frac{\rho_p}{\rho_f}. \tag{2.8}$$

In terms of the average density in the flow, we may also define an effective Reynolds number $R_{eff} = (1 + \bar{f}_{ave})R$. These two quantities, the Reynolds number R and the Stokes number S, along with the thickness σ of the particle-laden layer, the mass loading for a given σ as measured by f_{max}, and the location a_p of the maximum in particle concentration are the parameters which determine this problem.

2.2.2 Linear stability equations

After non-dimensionalising, we split all quantities in equations (2.1–2.4) into their basic and fluctuating parts, as $\mathbf{u} = \mathbf{U} + \hat{\mathbf{u}}$, $\mathbf{v} = \mathbf{U} + \hat{\mathbf{v}}$, $p = P + \hat{p}$, $f = \bar{f} + \hat{f}$ and $\mu^{tot} = \bar{\mu} + \hat{\mu}$. Here a hat represents a perturbation quantity, while an upper case or overbar denotes a mean quantity. In parallel shear flows, we have $\mathbf{U} = U(y)\mathbf{e_x}$, where $\mathbf{e_x}$ is a unit vector in the streamwise direction, and $\bar{f} = \bar{f}(y)$. For small particulate volume fraction, the local

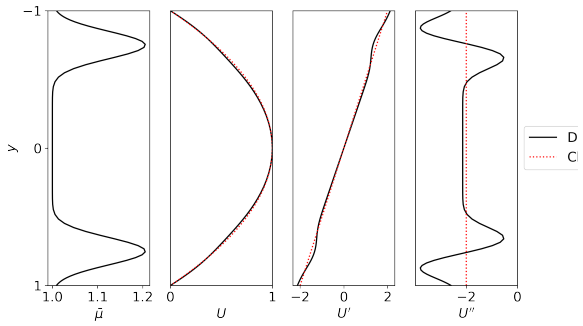

Figure 2.2: The mean viscosity, mean velocity, and their derivatives for the particle-laden flow (black) are compared to those for the clean flow (red dots). The parameters are as follows: the mean particle concentration profile has an amplitude of $f_{max} = 0.70$ and its peak is located at $a_p = 0.75$. The particle layer thickness is $\sigma = 0.1$, with $\gamma = 3.4$, and the Stokes number is $S = 8 \times 10^{-4}$.

viscosity is linearly related to the local particle concentration, as

$$\mu_d^{tot} = \mu_f \left[1 + \frac{f}{\gamma}\right], \tag{2.9}$$

where $\gamma \propto \rho_p/\rho_f$. In accordance with Einstein's law, we take the proportionality constant to be 0.4. In the limit of infinite γ, the dimensional viscosity remains at μ_f everywhere. The viscosity is non-dimensionalized by the viscosity of the pure fluid, μ_f. The mean viscosity is described as $\bar{\mu} = 1 + \bar{f}/\gamma$, and the perturbation viscosity is $\hat{\mu} = \hat{f}/\gamma$, obtained from equation (2.9).

We assume that the particles are sufficiently small such that with a small lag time, they attain the same velocity as the surrounding fluid, so in the steady state, both the flow and particles move together with a common mean velocity, $\mathbf{U}$. The mean flow profile, $U(y)$, satisfies the equation:

$$(\bar{\mu}U')'' = 0, \tag{2.10}$$

with the boundary conditions $U(\pm 1) = 0$, and $U(0) = 1$. When the particles are infinitely denser than the fluid (i.e., $\gamma \to \infty$), they do not occupy any significant volume fraction of the flow, and so do not introduce any change in viscosity. The mean viscosity thus remains constant, $\bar{\mu} = 1$. In this case, the mean velocity profile is parabolic, $U = 1 - y^2$, identical to the particle-free case. For particles with finite density, however, the mean velocity profile is modified, as shown in Figure (2.2).

Upon linearization of equations (2.1-2.4) we have

$$\left(\frac{\partial \hat{\mathbf{u}}}{\partial t} + \hat{\mathbf{u}} \cdot \nabla \mathbf{U} + \mathbf{U} \cdot \nabla \hat{\mathbf{u}}\right) = -\nabla \hat{p} + \frac{1}{R}\Bigg[\nabla \bar{\mu} \cdot \left(\nabla \hat{\mathbf{u}} + (\nabla \hat{\mathbf{u}})^T\right) + \nabla \hat{\mu} \cdot \left(\nabla \mathbf{U} + (\nabla \mathbf{U})^T\right) + \hat{\mu} \nabla^2 \mathbf{U} + \bar{\mu} \nabla^2 \hat{\mathbf{u}}\Bigg] + \frac{\bar{f}}{SR}\left(\hat{\mathbf{v}} - \hat{\mathbf{u}}\right), \tag{2.11}$$

$$\nabla \cdot \hat{\mathbf{u}} = 0, \tag{2.12}$$

$$\left(\frac{\partial \hat{\mathbf{v}}}{\partial t} + \hat{\mathbf{v}} \cdot \nabla \mathbf{U} + \mathbf{U} \cdot \nabla \hat{\mathbf{v}}\right) = -\frac{1}{SR}\left(\hat{\mathbf{v}} - \hat{\mathbf{u}}\right), \tag{2.13}$$

$$\frac{\partial \hat{f}}{\partial t} + \nabla \cdot (\bar{f}\, \hat{\mathbf{v}}) + \nabla \cdot (\hat{f}\, \mathbf{U}) = 0. \tag{2.14}$$

We start by performing a normal mode analysis, considering single Fourier modes for the perturbation quantities ($\hat{\mathbf{u}}$, $\hat{\mathbf{v}}$, $\hat{p}$, $\hat{f}$, $\hat{\mu}$) in both the x-direction and z-direction, as well as in time. In other words, the perturbation quantities are written in normal mode form, with each mode given by

$$(\hat{\mathbf{u}}, \hat{\mathbf{v}}, \hat{f}, \hat{\mu}) = \frac{1}{2}\left[(\mathbf{u}(y), \mathbf{v}(y), f(y), \mu(y)) \exp\left\{i\alpha(x - ct) + i\beta z\right\} + \text{c.c.}\right]. \tag{2.15}$$

We may now express the particle velocity in terms of the flow velocity using equations (2.13), to get

$$(v_x, v_y, v_z) = (\mathcal{M} u_x - SR\mathcal{M}^2 U' u_y, \mathcal{M} u_y, \mathcal{M} u_z) \tag{2.16}$$

where

$$\mathcal{M} = \frac{1}{1 + i\alpha SR(U - c)}. \tag{2.17}$$

Additionally, by taking the divergence of equation (2.11), we write the pressure laplacian in terms of the velocity field as

$$\begin{aligned} -\nabla^2 p = 2i\alpha U' u_y - \Big[2\bar{\mu}' \nabla^2 u_y + 2\bar{\mu}'' D u_y + 2i\alpha U' D\mu + 2i\alpha U'' \mu\Big] \\ - \frac{1}{SR}\Big[\bar{f}'(\mathcal{M} - 1) u_y + \bar{f} \mathcal{M}' u_y - i\alpha SR \mathcal{M}^2 U' \bar{f} u_y\Big]. \end{aligned} \tag{2.18}$$

We apply the operator ∇^2 to the y component of the vector equation (2.11), use equations (2.16) and (2.18), and divide throughout by $-i\alpha^2$ to express the resulting equation in

terms of the variables u_y and μ:

$$\begin{aligned}-ic\nabla^2\frac{u_y}{-i\alpha} &= i\left[U''-U\nabla^2\right]\frac{u_y}{-i\alpha}+\frac{1}{\alpha R}\left[\bar{\mu}''\left(-\nabla^2+2D^2\right)+2\bar{\mu}'D\nabla^2+\bar{\mu}\nabla^4\right]\frac{u_y}{-i\alpha}\\ &+\frac{1}{\alpha R}\left[U'''+2U''D-U'\nabla^2+2U'D^2\right]\mu\\ &+i\left[(\mathcal{M}^2U'\bar{f})'-(U-c)\mathcal{M}\bar{f}'D-(U-c)\mathcal{M}\bar{f}\nabla^2\right]\frac{u_y}{-i\alpha}\end{aligned} \tag{2.19}$$

Using equation (2.16) and the continuity equation (2.12), we can convert equation (2.4) into an expression that includes the variables u_y and μ, leading, after dividing throughout by $-i\alpha$, to

$$(U-c)\gamma\mu+\left[-RS\mathcal{M}^2U'\bar{f}'+\frac{(\mathcal{M}\bar{f})'}{i\alpha}\right]u_y=0. \tag{2.20}$$

Equations (2.19) and (2.20) represent the linear stability equations for three-dimensional perturbations. For a clean parallel shear flow without particles, Squire [1933] had shown that for every three-dimensional perturbation mode satisfying the stability equations, there exists a corresponding two-dimensional perturbation mode at a lower Reynolds number, displaying the same growth rate. Saffman [1962] had shown that Squire's theorem applies in the case of a dusty channel with uniform particle loading. If we substitute $(\alpha^2+\beta^2)=\alpha_{2D}^2$, $\alpha R=\alpha_{2D}R_{2D}$, and $u_y/\alpha=u_{y,2D}/\alpha_{2D}$ into the aforementioned equations (2.19) and (2.20), these equations become equivalent to those of a two-dimensional system with the wave number denoted as α_{2D}, the Reynolds number as R_{2D} and the velocity eigenfunction $u_{y,2D}$. We thus show that Squire's theorem may be extended to dusty channels with inhomogeneous loading, including viscosity variation as well. Thus for two-dimensional perturbations, these equations become (2.21) and (2.22). Therefore, while a nonmodal study would require us to study three-dimensional perturbations, since our purpose is to obtain linear instability at low Reynolds number, it is sufficient to perform a two-dimensional calculation, by setting $\beta=0$ in equation 2.15. In fact results for any given three-dimensional single mode may be obtained directly from an equivalent two-dimensional one by simple rescaling.

The two-dimensional equations for linear perturbations, after appropriate elimination and reduction, can be written in terms of the perturbation streamfunction $\psi(y)$ and the perturbation viscosity $\mu(y)$ as:

$$\begin{aligned}\left[(U_*-c)(D^2-\alpha^2)-U_*''\right]\psi+D(J\bar{f}'\psi) &= \frac{1}{i\alpha R}\Big[\bar{\mu}(D^2-\alpha^2)^2+2\bar{\mu}'D^3+\bar{\mu}''D^2\\ &-2\alpha^2\bar{\mu}'D+\alpha^2\bar{\mu}''\Big]\psi+\frac{1}{R}\left[U'D^2+2U''D+U'''+\alpha^2U'\right]\mu,\end{aligned} \tag{2.21}$$

and

$$-(U-c)\gamma\mu + \Big[-i\alpha RS\mathcal{M}^2 U'\bar{f}' + (\mathcal{M}\bar{f})' \Big]\psi = 0, \tag{2.22}$$

where

$$U_* \equiv U + J\bar{f}, \quad \mathcal{M} = \frac{1}{1+i\alpha(U-c)SR}, \quad J = (U-c)\mathcal{M}, \tag{2.23}$$

$$u_y = -i\alpha\psi \tag{2.24a}$$

$$u_x = D\psi \tag{2.24b}$$

$$v_x = \mathcal{M}u_x - (\mathcal{M}^2 SRU')u_y \tag{2.24c}$$

$$v_y = \mathcal{M}u_y \tag{2.24d}$$

The operator D is defined as $D = d/dy$, and a prime denotes a derivative in y of a mean quantity. Note that v_x and v_y in equations (2.24c, 2.24d) can be expressed in terms of ψ using equations (2.24a, 2.24b). The boundary conditions are:

$$\psi(y=\pm1) = D\psi(y=\pm1) = \mu(y=\pm1) = 0 \tag{2.25}$$

For given mean flow $U(y)$ streamwise wavenumber α, base particle loading $\bar{f}(y)$, particle to fluid density ratio, and fixed Reynolds and Stokes numbers, equations 2.21 to 2.25 define an eigenvalue problem, which yields a spectrum of eigenvalues c and corresponding eigenfunctions, $(\psi(y), \mu(y))$. If even one eigenvalue has a positive imaginary part, i.e., $c_{im} > 0$, we have an exponential growing mode.

In the limit of $\gamma \to \infty$, we have $\bar{\mu} = 1$ and $\mu = 0$, so equation (2.21) becomes

$$\left[(U_*-c)(D^2-\alpha^2) - U_*''\right]\psi + (J\bar{f}')'\psi + (J\bar{f}')D\psi = \frac{1}{i\alpha R}(D^2-\alpha^2)^2\psi \tag{2.26}$$

and is now decoupled from equation (2.22). When there is no particulate suspension, we have $\bar{f} = 0$, and the system (2.26) reduces to the well-known Orr-Sommerfeld equation

$$\left[U(D^2-\alpha^2) - U'' + \frac{i}{\alpha R}(D^2-\alpha^2)^2\right]\psi = c\left(D^2-\alpha^2\right)\psi. \tag{2.27}$$

In the case of a homogeneous suspension ($\bar{f}$ = constant) along with $\gamma \to \infty$, the system reduces to that of Saffman [1962].

2.2.3 Balance of perturbation kinetic energy

Whenever the flow is unstable, there is an exponential increase in perturbation kinetic energy. It is useful to derive the positive and negative contributors to this quantity. To do this, we multiply the linear equations for the fluid flow (in $\hat{\mathbf{u}}$) and for the particulate flow (in $\hat{\mathbf{v}}$), given as equations (2.11) and (2.13), by the respective complex conjugates $\hat{\mathbf{u}}^*$ and $\hat{\mathbf{v}}^*$. Upon averaging over a wavelength in the streamwise direction, we derive the evolution of perturbation kinetic energy $\hat{E}$ to be described by

$$\begin{aligned}\partial_t \int \hat{E}\, dV = &- \int \frac{\partial U_i}{\partial x_j}\hat{u}_i\hat{u}_j^* dV - \frac{1}{R}\int \bar{\mu}\,|\partial_i \hat{u}_j|^2\, dV \\ &- \int \bar{f}\frac{\partial U_i}{\partial x_j}\hat{v}_i\hat{v}_j^* dV - \frac{1}{SR}\int \bar{f}\,|\hat{u}_i - \hat{v}_i|^2\, dV \\ &- \frac{1}{R}\int \frac{\partial^2 \bar{\mu}}{\partial x_j \partial x_i}\hat{u}_i\hat{u}_j^* dV - \frac{1}{R}\int \frac{\partial U_j}{\partial x_i}\hat{\mu}(\partial_j \hat{u}_i + \partial_i \hat{u}_j) dV\end{aligned} \tag{2.28}$$

where

$$\hat{E} = \frac{1}{2}(\hat{u}_i^2 + \bar{f}\hat{v}_i^2), \tag{2.29}$$

and V indicates a volume of fluid extending from wall to wall and over one perturbation wavelength in the streamwise direction. We then introduce the normal-mode forms of the perturbations, given by equation (2.15), into equation (2.28), and average over the streamwise direction x, to get

$$\begin{aligned}2\alpha c_{im}\int E\, dy = &- \frac{1}{4}\int \frac{\partial U_i}{\partial x_j}\left(u_i u_j^* + u_i^* u_j\right) dy - \frac{1}{2R}\int \bar{\mu}\,|\partial_i u_j|^2\, dy \\ &- \frac{1}{4}\int \bar{f}\frac{\partial U_i}{\partial x_j}\left(v_i v_j^* + v_i^* v_j\right) dy - \frac{1}{2SR}\int \bar{f}\,|u_i - v_i|^2\, dy \\ &- \frac{1}{4R}\int \frac{\partial^2 \bar{\mu}}{\partial x_j \partial x_i}\left(u_i^* u_j + u_i u_j^*\right) dy \\ &- \frac{1}{4R}\int \frac{\partial U_j}{\partial x_i}\{\mu(\partial_j u_i^* + \partial_i u_j^*) + \mu^*(\partial_j u_i + \partial_i u_j)\} dy \\ &\equiv \int (W_+ - W_- + W_{p+} - W_{p-} + W_{\mu,1} + W_{\mu,2}) dy,\end{aligned} \tag{2.30}$$

where

$$E(y) = \frac{1}{4}(u_i(y)^2 + \bar{f}v_i(y)^2), \tag{2.31}$$

and $W_+(y)$ and $W_-(y)$ respectively are the production and dissipation of perturbation kinetic by the fluid, while $W_{p+}(y)$ and $W_{p-}(y)$ respectively give the production and dissipation of perturbation kinetic energy of the particles. The last two terms $W_{\mu,1}$ and $W_{\mu,2}$ arise due to viscosity stratification.

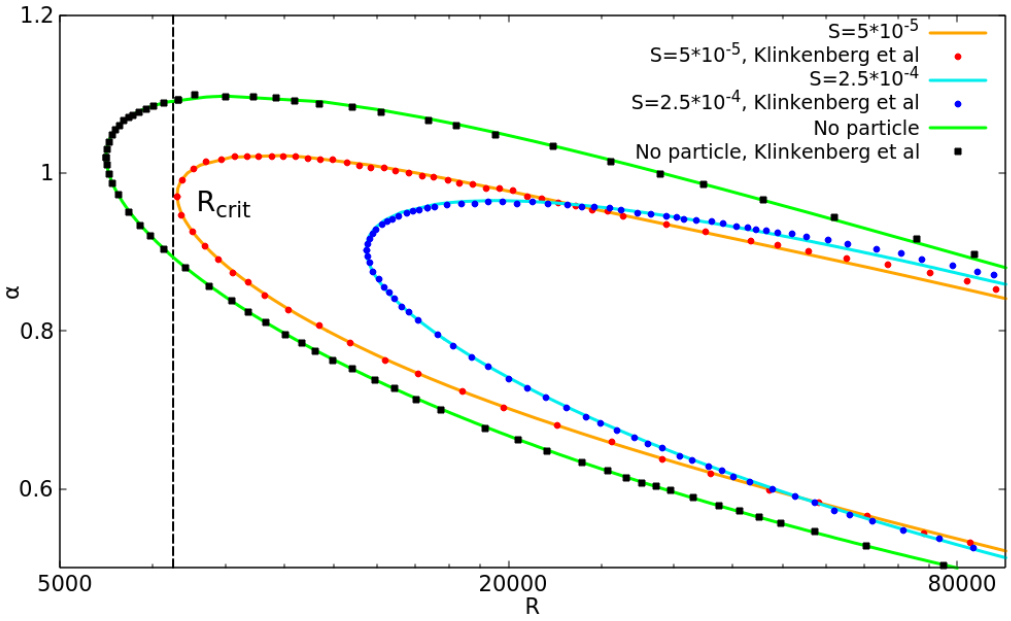

Figure 2.3: Validation for the case of uniform particle loading, in the form of neutral stability curves, with $\bar{f} = 0.05$, $S = 5 \times 10^{-5}$, and $S = 2.5 \times 10^{-4}$. Symbols correspond to Klinkenberg et al. [2011], while solid lines are from present computations. The region within the curves is unstable. The black dotted vertical line marks the minimum Reynolds number for $S = 5 \cdot 10^{-5}$ at which instability is seen, termed the critical Reynolds number R_{crit}.

2.2.4 Numerical method

We employ the Chebyshev spectral collocation method to discretize the system given by equations 2.21 to 2.25 at n discrete points in the domain. The Chebyshev collocation points, defined as $y_{Cheb,j} = \cos[\pi j/(n-1)], \quad j = 0, 1, 2, 3, ..., n-1$, are naturally clustered close to the walls. Such a discretisation would resolve the near-wall region well, where variations are large. But, for a small number of collocation points it would leave the particle layer, where too variations are large, not well resolved. In order to get results insensitive to the number of collocation points, we employ a stretching function to cluster a sufficient number of grid points into the particle-laden layer. Such a stretching function was used in Govindarajan [2004] in a different context, and works well in the present situation as well. It is given by

$$y_j = \frac{a}{\sinh(by_b)} \left[\sinh\left\{(y_{Cheb,j} - y_b)\, b\right\} + \sinh(by_b)\right], \tag{2.32}$$

where

$$y_b = \frac{1}{2b} \log\left[\frac{1 + (e^b - 1)\, a}{1 + (e^{-b} - 1)\, a}\right]$$

is a constant, a signifies the location around which clustering is desired, and b serves to determine the level of clustering. Once written in discrete form, each boundary condition

may be applied by replacing one row of the discrete system appropriately. To solve equation (2.26) after discretisation, we utilize the LAPACK FORTRAN package. For our all simulations, we use $n = 81$, and verify our answers with $n = 121$. At this resolution, the results are insensitive to the number of grid points, as well as to whether stretching is employed or not. But stretching improves the physical appearance of the eigenfunctions.

Since the chosen mass fraction profile corresponds to the clustering of particles in the vicinity of $y = \pm a_p$, we select a to be equal to $\pm a_p$ and set b to the value of 2 or 4 in equation (2.32). We obtain eigenvalues correct to five decimal places for the most part, and at least to four places everywhere. At Stokes number of 10^{-2} or higher, however, the accuracy drops to three decimal places, and we do not venture into this regime to make our conclusions.

To validate our approach, we first perform computations using a uniform particle profile across the channel. Figure 2.3 shows neutral stability boundaries provided by Klinkenberg et al. [2011], compared to present computations. The agreement is excellent for two different particle Stokes numbers as well as for the clean channel. The mode of instability which appears in all these cases is the traditional Tollmien-Schlichting (hereafter TS) instability, which is modified by the introduction of particles.

We are now in a position to study the instability mechanism. In the following section we derive a minimal equation set which allows us to highlight the basic physics.

2.3 A minimal composite theory for particulate shear flow stability

It is useful to begin this section by defining the critical layer, since the physics therein dominate this discourse. It is a relatively thin layer centered around the critical point y_c in the channel, where the mean-flow velocity is the same as the phase speed of the dominant normal-mode perturbation, i.e., $U(y_c) = c$ [Lin, 1945a,b, 1946]. The particle layer on the other hand, as seen from equation (2.6), is centered around $y = a_p$. If y_c and a_p are in close proximity, such that both layers overlap, we term it as the 'overlap' condition, and when these layers are distinct and well-separated, we term it a 'non-overlap' condition. The channel comprises the critical layer, the wall layer, the particle laden layer and the inviscid outer layer; and different physics can appear in each. The first three are shown schematically in figure 2.4, under overlap and non-overlap conditions. The need for asymptotic analyses in the different layers is motivated below.

In the dilute particle limit, whether or not the particles are far denser than the fluid, it can be worked out that the viscosity variation terms will not enter the dominant balance, so we may work with the single equation 2.26.

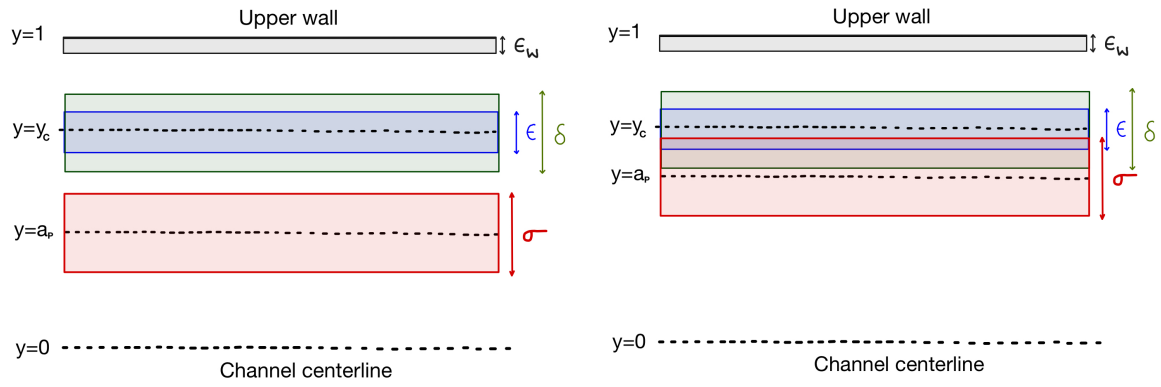

(a) (b)

Figure 2.4: Schematic of layers within which there are rapid variations in one or more physical quantities. The perturbation stream function ψ and the perturbation suspension velocities v_x and v_y display critical layers of thickness ϵ and δ respectively around $y = y_c$. Additionally, the swift transition in the suspension mass fraction profile occurring at $y = a_p$ within a small region characterized by size σ is seen. This depiction shows only the top half of the channel; the other half being symmetric. (a) condition where the layers are distinct, (b) overlap condition.

2.3.1 Motivation

We saw in figure 2.3 that in the case of constant particle loading, the TS mode of instability is modified by particles. Even with non-uniform particle loading, under non-overlap conditions, the same is observed. On the other hand, under overlap conditions, the picture is very different, and an example is shown in figure 2.5. Here the TS mode is seen as a minor blip on the right of the figure. Two other modes of instability are now seen, which occur at much lower Reynolds number. The fact that these modes are distinct from the TS mode is evident from the separate regions in $\alpha - R$ space they occupy. To distinguish between them, the two lower Reynolds number modes of instability will be termed shortwave and longwave respectively, while remembering that the so-called shortwave mode actually has perturbation wavelengths of $O(1)$, i.e., comparable to the channel width (a wavelength of $\alpha = 1$ is 2π times the half-width). The longwave modes extend from $O(1)$ to far lower wavenumbers. The shortwave mode of overlap instability occurs over the smallest Reynolds numbers, ranging from a few hundreds to a few thousands, while the longwave mode spans decades in the Reynolds number, with the instability Reynolds number and the typical wavelength increasing together. In the following section we show that both of these are overlap modes of instability, caused by the variation of particle concentration within the critical layer. In section 2.3.3 we perform a similar analysis for the wall layer.

In explaining the mechanism for the low Reynolds number instabilities, we may pursue one of two approaches. For both of them, we must begin by deriving the dominant balance in the critical layer. Once we have the lowest order equations in the critical layer,

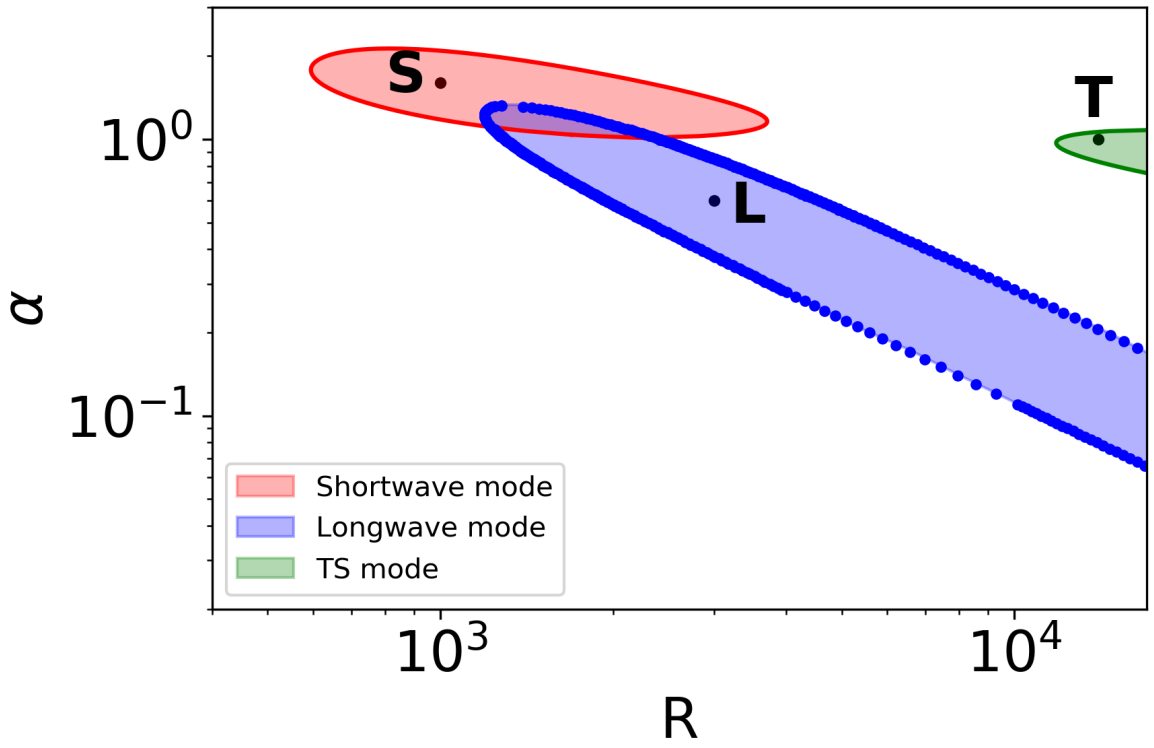

Figure 2.5: The three distinct modes of instability, shown by the shaded regions. A specific choice of parameters is made here, where overlap conditions prevail: the peak of the mean particle concentration profile has an amplitude $f_{max} = 0.70$, and is positioned at $a_p = 0.75$. The thickness of the particle-layer is $\sigma = 0.1$ and the Stokes number is $S = 8 \times 10^{-4}$. This figure is representative of a wide range of parameters under overlap conditions. The points marked S, L and T are representative of shortwave, longwave and Tollmien-Schlichting modes respectively, and will be elaborated on.

we could solve the equations in the inner (critical) layer, and perform a matching with the outer layer (inviscid) solutions to obtain the full solutions. But this would yield no extra information, since we can already solve the full solutions. We therefore follow a second approach: of writing down a minimal composite theory for particulate shear flow. This theory [Narasimha and Govindarajan, 2000, Govindarajan and Narasimha, 2001, Bhattacharya et al., 2006] will obtain a reduced set of equations describing the stability problem. The reduced equations will contain all terms in the complete stability equations (2.55) which participate in the dominant balance somewhere in the flow, and none of the terms which do not participate in this anywhere.

2.3.2 Dominant balances in the critical layer

We first summarise existing knowledge in the context of a clean fluid, and then derive dominant balances within the critical layer in particulate shear flow.

In the Orr-Sommerfeld equation (2.27) for a clean fluid, it is seen that the highest, i.e., fourth-order, derivative term in y is scaled by the inverse of the Reynolds number. Now even if the Reynolds number approaches infinity, this term may not be dropped, because if it is, we will not be able to satisfy all four boundary conditions associated with equation (2.27). This is thus a classical singular perturbation problem [Van Dyke, 1964], where the highest derivative term becomes as big as the terms on the left-hand side in some portions of the flow. There are two layers [Lin, 1945a,b, 1946] where viscous effects are important and gradients are large: the wall layer, of thickness $\epsilon_w \sim R^{-1/2}$, and the critical layer, of thickness $\epsilon \sim R^{-1/3}$ where, as defined above, $U \sim c$. It is the latter which is of primary interest to us to explain the mechanism of the overlap instabilities. To perform a similar analysis for particulate shear flow, we limit ourselves here to the regime where $RS \sim O(1)$, which is reasonable for dilute particle suspensions at high Reynolds number. A similar analysis may be carried out for any order of magnitude of this quantity. There are three layers we pay attention to on each side of the centreline, and these are shown in Fig. (2.4) for one half of the channel. There is also a wall layer shown, which will be discussed separately in section 2.3.3. There are now two critical layers: for the fluid and for the particle flow, of thickness ϵ and δ respectively, and the layer where the particles are concentrated, of thickness σ, which is pre-specified. The scales $\epsilon \ll 1$ and $\delta \ll 1$ are as yet unknown, and will be determined below. Fig. (2.4a) is a schematic for conditions where the particle layer and the critical layer are distinct, which we shall refer to as the non-overlap condition, and Fig. (2.4b) depicts the overlap condition.

We derive equations within the critical (inner) layer in the inner variables ξ and λ, defined as

$$\xi = \frac{y - y_c}{\epsilon}, \quad \text{and} \quad \lambda = \frac{y - y_c}{\delta} \tag{2.33}$$

and will select ϵ and δ to ensure that the derivatives of the fluid velocity components in ξ and the particle velocity components in λ are $O(1)$. In addition, it is useful to define

$$\chi = \frac{y - a_p}{\sigma}. \tag{2.34}$$

To derive the dominant balances we write the relevant variables in the form of series expansions within the critical layer as

$$u_y = \sum_{n=0}^{\infty} \epsilon^n u_{y,n}(\xi), \quad v_y = \sum_{n=0}^{\infty} \delta^n v_{y,n}(\lambda) \quad \text{and} \quad v_x = \sum_{n=0}^{\infty} \delta^n v_{x,n}(\lambda). \tag{2.35}$$

In this layer the mean flow may be written in the following expansion:

$$U(y) - c = (y - y_c)U_c^{'} + \frac{(y - y_c)^2}{2} U_c^{''} + \cdots . \tag{2.36}$$

The relative magnitudes within the critical layer of the two components of flow can be established from the continuity equation. We have

$$\sum_{n=0}^{\infty} \epsilon^n \left[i\alpha u_{x,n} + \frac{1}{\epsilon} D_\chi u_{y,n} \right] = 0. \tag{2.37}$$

Constructing hierarchies of equations of different powers of ϵ yields

$$u_{y,0} = 0 \tag{2.38}$$

and shows that the coefficient of a particular power of ϵ in u_x is related to that which is one order higher in u_y. This is in fact a natural consequence of incompressibility. For the particle field, from the equation (2.24), and using equations (2.35) and (2.36), we get

$$\left[U - c - \frac{i}{\alpha SR} \right] v_x = i\frac{U'}{\alpha} v_y + \frac{1}{\alpha^2 SR} D u_y. \tag{2.39}$$

At the next two orders, using equation (2.39) as well as the incompressibility condition $D_\xi u_{y,1} = -i\alpha u_{x,0}$ in the critical layer, we get

$$v_{x,0} = u_{x,0}, \quad v_{x,1} = \frac{\epsilon}{\delta} \left\{ \frac{i}{\alpha} D_\xi u_{y,2} - i\alpha SR U_c^{'} \xi v_{x,0} \right\} - SR U_c^{'} v_{y,1}. \tag{2.40}$$

This yields $\delta \sim \epsilon$, and without loss of generality, we choose $\delta = \epsilon$. The critical layer thickness as perceived by the fluid and the particles is thus identical.

Using the third row of the matrix equation (2.26) along with equations (2.35) and

(2.36), and collecting terms at the lowest order in the expansion, we obtain

$$v_{y,0} = u_{y,0}, \tag{2.41}$$

which we know to be 0 from equation (2.38). In other words, the expansions for the normal velocity components for the particles too begin one order higher than the streamwise component. At the next two orders, from the equation (2.24)

$$\left[U - c - \frac{i}{\alpha SR}\right] v_y = -\frac{i}{\alpha SR} u_y \tag{2.42}$$

we get

$$v_{y,1} = u_{y,1}, \quad \text{and} \quad v_{y,2} = u_{y,2} - i\alpha SR U_c^{'} \xi v_{y,1}. \tag{2.43}$$

From equations (2.35), (2.40), and (2.43), we can see that the components of $\mathbf{v}$ and $\mathbf{u}$ differ from each other only at order ϵ relative to their largest value in the critical layer. This is consistent with the expectation that the particle velocity field must closely follow the fluid velocity field for low Stokes numbers. This analysis yields a measure of the difference between the two.

Finally, we may derive the dominant balance for fluid velocity in the critical layer from the equation (2.24), along with (2.35) and (2.36), and the Taylor expansion

$$\bar{f} = \begin{cases} \bar{f}_c + (y - y_c)\bar{f}_c' + \frac{(y-y_c)^2}{2}\bar{f}_c'' + \cdots, & \text{overlap case} \\ \bar{f}_c, & \text{non-overlap case} \end{cases} \tag{2.44}$$

and under overlap conditions we may rewrite this in the relevant variable χ. Now there are different choices possible for the small parameters. We therefore apriori retain all terms which may participate in the dominant balance, and after some algebra obtain the following composite lowest-order equation

$$\left[(1 + \bar{f})\xi U_c' D_\xi^2 + i\frac{1}{\alpha R \epsilon^3} D_\xi^4 - \frac{\epsilon}{\sigma} U_c' (D_\chi \bar{f})(I - \xi D_\xi)\right] u_{y,1} = 0, \tag{2.45}$$

where I is the identity operator. We will have one of the following four distinct cases arising. Case 1 includes the non-overlap case, while the others are for overlap conditions.
Case-1: Either the particle layer and critical layer are well separated, or they overlap, but $1 \sim \frac{1}{\alpha R \epsilon^3} \gg \frac{\epsilon}{\sigma}$, i.e., the size of the particle layer significantly exceeds that of the critical layer. The third term in equation (2.45) now becomes negligible and in both cases this equation simplifies to:

$$\left[-iU_c' \xi D_\xi^2 + D_\xi^4\right] u_{y,1} = 0. \tag{2.46}$$

The balance, with $\epsilon = \alpha R^{-1/3}$, is identical to the case with no particles, for the following

reasons. When the particle layer and critical layer are well separated, the mass fraction $\bar{f}$ and its derivative $(D_\chi \bar{f})$ / σ practically negligible or much less than $O(1)$ in the critical layer, regardless of how small the particle layer σ is.

Case-2: $1 \ll \frac{1}{\alpha R \epsilon^3} \sim \frac{\epsilon}{\sigma}$, i.e., the particle-laden layer is markedly smaller than the critical layer. The scaling that emerges is $\epsilon \sim (\frac{\sigma}{\alpha R})^{1/4}$, and upon replacing $\sim$ by equality, equation (2.45) simplifies to:

$$\left[D_\xi^4 + i\left\{(D_\chi \bar{f})_c U_c'\right\}(I - \xi D_\xi)\right] u_{y,1} = 0. \tag{2.47}$$

The variation in particle concentration is as important as the largest viscous effects in the critical layer.

Case-3: $1 \sim \frac{\epsilon}{\sigma} \gg \frac{1}{\alpha R \epsilon^3}$. The size of the particle layer is comparable to that of the critical layer, and the critical layer is much wider than that dictated by the scaling on the inverse Reynolds number. This case is a mathematical possibility, but is unlikely to occur physically, since the critical layer at large Reynolds will normally be influenced by the Reynolds number, and become thinner as Reynolds number increases. Under these hypothetical conditions, viscous effects appear only at higher order, since equation (2.45) simplifies to:

$$\left[(1 + \bar{f})\xi U_c' D_\xi^2 - (D_\chi \bar{f}) U_c' (I - \xi D_\xi)\right] u_{y,1} = 0, \tag{2.48}$$

where we have set $\epsilon = \sigma$.

Case-4: $1 \sim \frac{\epsilon}{\sigma} \sim \frac{1}{\alpha R \epsilon^3}$. The size of the particle layer is comparable to that of the critical layer, and viscosity plays a significant role as well. Equation (2.45) now becomes

$$\left[U_c'(1 + \bar{f})\xi D_\xi^2 + i D_\xi^4 - \kappa (D_\chi \bar{f}) U_c' (I - \xi D_\xi)\right] u_{y,1} = 0, \tag{2.49}$$

Here, we define $\epsilon = (\alpha R)^{-1/3}$ and $\frac{\epsilon}{\sigma} \equiv \kappa$.

Equation (2.49) completely describes the critical layer for the thickness σ we consider. Cases 2 to 4 correspond to overlap conditions, and the variation of the particle concentration within the critical layer, estimated by $D_\chi \bar{f}$ is an important player in the critical-layer balance, altering it fundamentally. We have thus established that the concentration profile will alter the fundamental nature of shear flow instability, only under overlap conditions. This effect would be absent with uniform particle loading, where only under case 4, we will have a factor $(1 + \bar{f})$ which merely rescales the Reynolds number.

2.3.3 Dominant balance in the wall layer

In shear flows, the critical and wall layers are often not well-separated, and the overlap mode of instability presents such a case. We conduct the exercise below only to confirm that wall effects are not bringing in new physics into the instability. As before we define

inner variables

$$\xi = \frac{y - y_w}{\epsilon_w}, \quad \text{and} \quad \lambda = \frac{y - y_w}{\delta_w} \tag{2.50}$$

where $y_w = \pm 1$ are the wall locations. Also, we have $U_w \equiv U(y_w) = 0$ and $U_w^{'} \equiv U'(y_w)$. We expand the variables in the form

$$u_y = \sum_{n=0}^{\infty} \epsilon_w^n u_{y,n}(\xi), \quad v_y = \sum_{n=0}^{\infty} \delta_w^n v_{y,n}(\lambda) \quad \text{and} \quad v_x = \sum_{n=0}^{\infty} \delta_w^n v_{x,n}(\lambda). \tag{2.51}$$

At the lowest order, $u_{y,0} = 0$, and $v_{y,0}$ is proportional to this quantity and thus vanishes. At the next order, after some algebra, we obtain the scaling $\delta_w = \epsilon_w$, and we can use the incompressibility condition $D_\xi u_{y,1} = -i\alpha u_{x,0}$. Additionally, we have the following equations:

$$v_{x,0} = \frac{u_{x,0}}{1 - i\alpha cSR}, \tag{2.52}$$

$$v_{x,1} = \frac{u_{x,1}}{1 - i\alpha cSR} - \left(\frac{SRU_w'}{1 - i\alpha cSR}\right) v_{y,1}, \quad \text{and} \quad v_{y,1} = \frac{u_{y,1}}{1 - i\alpha cSR}. \tag{2.53}$$

We can express the dominant-balance composite equation for the flow as follows:

$$\left[-c\left(1 + \frac{\bar{f}}{1 - i\alpha cSR}\right) D_\xi^2 + i\frac{1}{\alpha R\epsilon_w^2} D_\xi^4 - \frac{\epsilon_w}{\sigma}\left(\frac{cD_\chi \bar{f}}{1 - i\alpha cSR}\right) D_\xi\right] u_{y,1} = 0 \tag{2.54}$$

The structure of equation (2.54) in the wall layer is the same as (2.45) in the critical layer. There are changes in the coefficients, which change the scaling of ϵ_w to be $(\alpha R)^{-1/2}$. Again, when $\epsilon_w \sim \sigma$, along with significant overlap of the wall layer and the particle layer, the first derivative of the particle concentration profile is among the biggest terms at the lowest order. In our range of study, the wall layer is always very thin and well-separated from the critical layer. All three terms are important when $\epsilon_w \sim (\alpha R)^{-1/2}$. In our investigation, we always positioned the particle layer at a considerable distance from the wall layer. Consequently, the mass fraction $\bar{f}$ and its derivative become negligible in the wall layer, and the dominant balance (2.54) is unaffected by the presence of particles.

2.3.4 Construction of the minimal composite theory

In the rest of the channel, a particle-laden counterpart of the Rayleigh equation, where all viscous effects are neglected in the stability operator, is valid. We now construct a reduced equation which includes every term in the complete equations (2.26) from which any of the dominant terms in the three layers originates, and neglects all other terms.

The final minimal composite equation is

$$\left[(U_* - c)(D^2 - \alpha^2) - U''\right]\psi - (J'\bar{f}')\psi + (J\bar{f}')D\psi = \frac{1}{i\alpha R} D^4\psi, \tag{2.55}$$

with, as before,

$$U_* \equiv U + J\bar{f} \qquad J \equiv \frac{U-c}{1+i\alpha(U-c)SR}. \tag{2.56}$$

The terms that are not included in the above equation compared to the full equation (2.26) are: $-J''\bar{f}\psi - (1/i\alpha R)(-2\alpha^2 D^2 + \alpha^4)\psi$, apart from all the viscosity stratification effects which vanish from the minimal physics in a dilute suspension. This is because the derivative of the mean viscosity is $O(f_{max}/[\gamma\sigma])$, which is small for a dilute suspension. Moreover, since J is a function of y, we see that (2.55) represents a significant reduction of the complete stability operator. It comprises the inviscid stability operator of Rayleigh and the highest order derivative in the viscous operator. For a constant particle loading, the only effect due to particles would come from the modified effective mean flow profile U_*. Besides these, terms appear are due to variations in the particle concentration profile which are critical. Note importantly that the minimal equation does not reduce to the Orr-Sommerfeld equation in any limit.

It remains to be seen whether the essential physics is contained in the minimal composite equation. The best parameter to make this explicit is the location, a_p, of the maximum in particle concentration. In figure 2.6 we show how the critical Reynolds number (the lowest Reynolds number for instability), R_{crit}, changes with a_p. The purple line with particles represents the full solution to equation (2.26), whereas the black line is the solution of the minimal composite equation (2.55). As a_p increases, the particle-laden layer shifts towards the wall. We see that below $a_p \sim 0.6$, there is a continuous increase in the critical Reynolds number. But beyond this, we see a sudden and large drop in R_{crit}, going down to values less than half of that a clean channel ($R_{crit} = 5772.2$). At large a_p, however, i.e., when the particle-laden layer is very close to the wall, the trend is reversed again and a large stabilization is seen. The complete trend is captured by the minimal composite equation, although, as is to be expected, the agreement with the full solution is only qualitative.

The sensitivity of the critical Reynolds number with the location of the particle-laden layer is now seen to have its root in the dynamics within the critical layer of the dominant disturbance. The critical layer is shown in the inset of figure 2.6, as a function of a_0. A notional thickness of $R^{-1/3}$ is shown in this sketch. Shown in the same figure is the linear movement of the particle-laden layer with a_p. The large changes in stability occur in the regime of a_p when the two layers overlap. A major portion of the disturbance kinetic energy is known to be produced within the critical layer in clean channel flow. We shall see that this is true of particulate flow too. Note that the wall layer (also shown in the figure) is unimportant in the dominant balance. A sufficiently steep gradient in the number density gives rise to these new types of instabilities, as illustrated in figure (2.7).

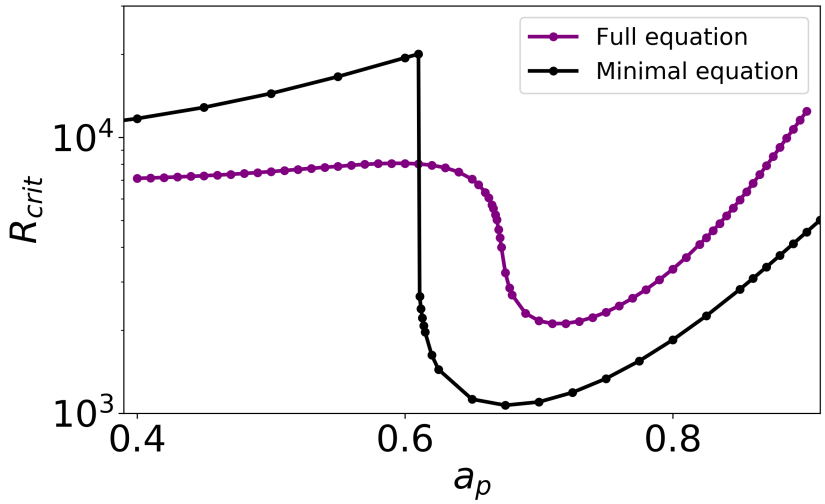

(a)

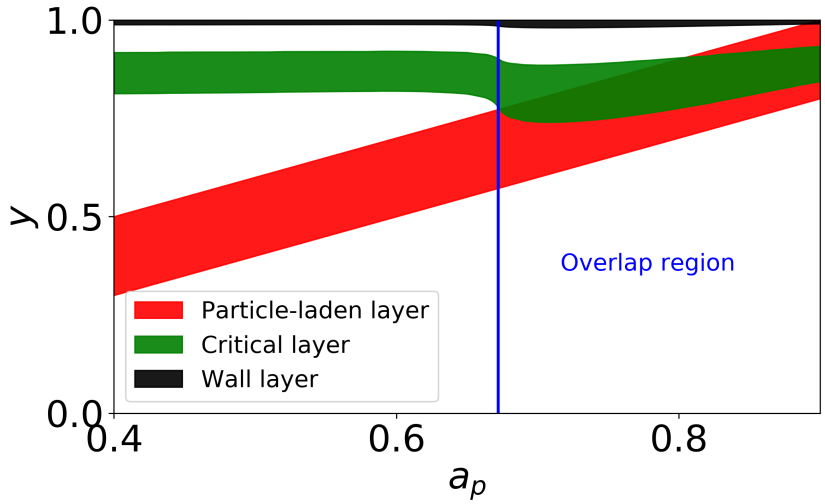

(b)

Figure 2.6: With a specified amplitude of $f_{max} = 0.1$, a peak width of $\sigma = 0.1$ for the mass fraction profile, and a Stokes number of $S = 2.5 \times 10^{-4}$, the purple curve and the black curve in (a) illustrate the critical Reynolds number as a function of the position of the peak, a_p of the mass fraction profile for the full equation (2.26) and the minimal equation (2.55) respectively. The green, black, and red bands in (b) illustrate the notional critical layer, the wall layer, and the particle-laden layer, respectively, as they vary with a_p.

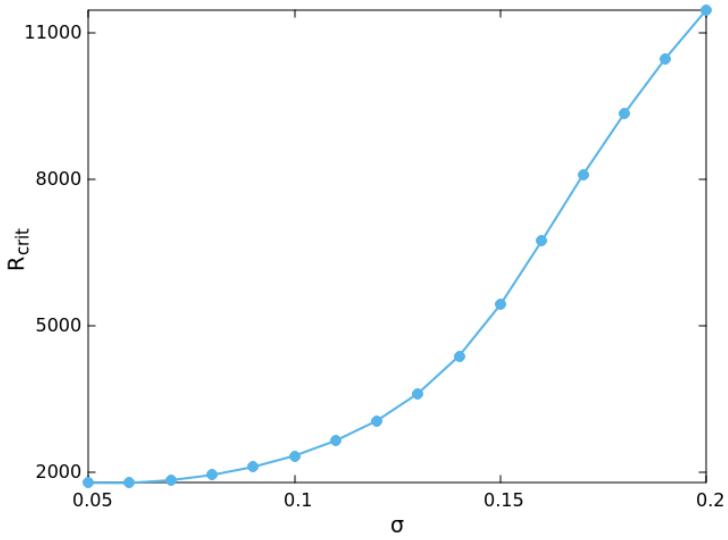

Figure 2.7: The critical Reynolds number is very sensitive to size of the particle layer. The parameters for this plot are $f_{\max} = 0.1$, $S = 2.5 \times 10^{-4}$, and $a_p = 0.75$.

2.3.5 Summary of instability features in the overlap and non-overlap contitions

Before we discuss the energy budget, we summarise some additional features of the modes of instability. The maximum, f_{max}, in the particle concentration and the thickness, σ, of the particle-laden layer, have a quantitative, rather than qualitative, effect. We fix σ at 0.1.

Figure 2.8 (a) and (b) summarise the variation of the critical Reynolds number (given in colour with contour lines) with the Stokes number and the particle loading. We examine two situations: at $a_p = 0.4$, where the overlap mechanism is not in operation, and at $a_p = 0.75$, where it is. It is evident that both in quality and quantity the two situations are very different. Under non-overlap conditions, i.e., where the particle-laden layer lies in a different part of the channel from the critical layer (figure 2.8(a)), we see stabilization as particle loading is increased. The stabilisation is enormous in some portions of the regime, with the critical Reynolds number being extremely sensitive to either the particle loading or the Stokes number or both. The qualitative dependence of the critical Reynolds number on Stokes number is essentially the same as that for uniformly distributed particles shown in Fig.(2.3) and in Fig.(1) of Rudyak et al. [1997]. At low Stokes number, the particles are sufficiently small that they follow the fluid motion closely. In this regime, they mainly act to increase the effective density of the suspension, so the decrease in the critical Reynolds number relative to the clean flow is minimal. For moderate Stokes number, particle–fluid coupling becomes significant and the drag dissipation increases, leading to a rise in the critical Reynolds number. At high Stokes number, the particles are large and barely interact with the flow, and therefore the critical Reynolds number approaches that of the

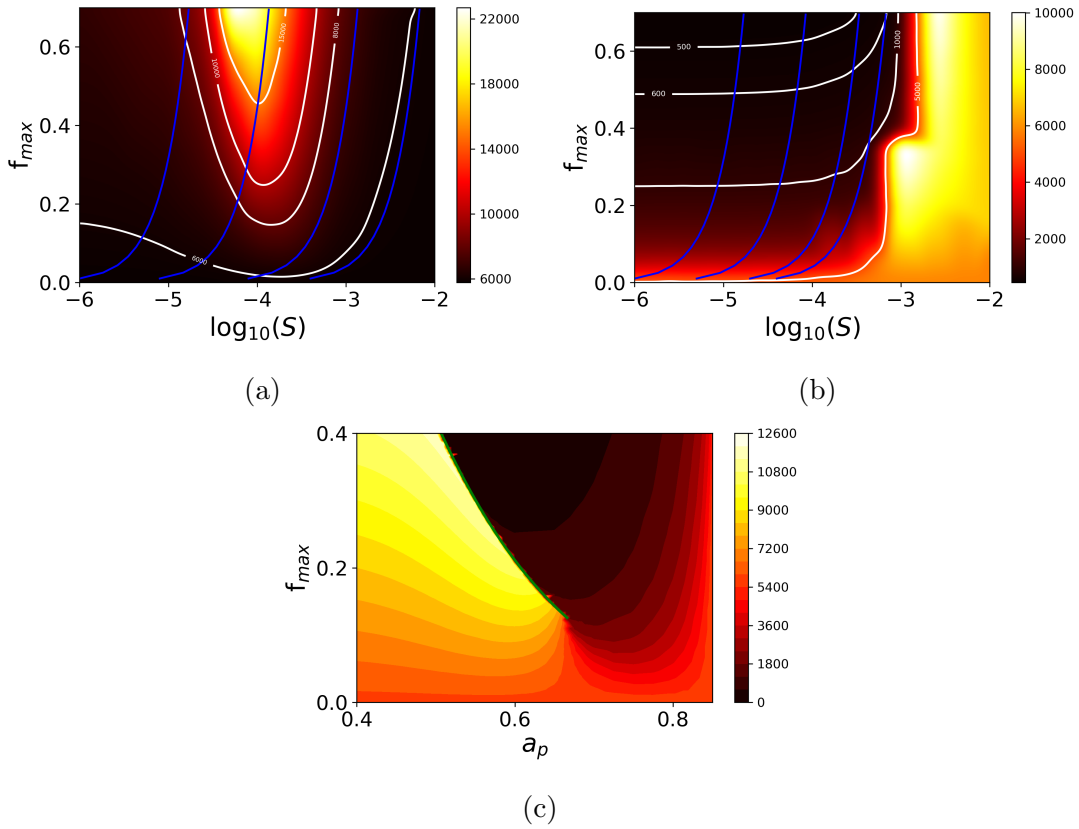

Figure 2.8: Phase plot of the critical Reynolds number, shown in colour, in (a) and (b) as a function of the Stokes number S and the particle loading strength f_{max}, and in (c) as a function of the particle loading location a_p, and f_{max}. (a) A case where there is no overlap mechanism in operation, with $a_p = 0.40$, and (b) where it is in operation, with $a_p = 0.75$. Note the difference in the colourbars in the two figures. In both figures $\sigma = 0.1$, and the blue lines represent curves of constant particle number density N. The value of N decreases from left to right, with the non-dimensional quantity $9\sqrt{2}H^3N\sqrt{\rho_f/\rho_p}$ being $[1.00 \times 10^7, 4.42 \times 10^5, 1.40 \times 10^4,$ and $1.25 \times 10^3]$ for plot (a), and $[1.00 \times 10^7, 8.94 \times 10^5, 1.12 \times 10^5,$ and $3.95 \times 10^4]$ for plot (b). The other parameters in (c) are the same as in Figure(2.6). The green curve serves as a visual guide for observing the sharp change in the critical Reynolds number due to a change in the mode of instability. Some jitter in the colours is visible, and is due to the interpolation of results on a finitely spaced grid.

clean fluid. We now turn to figure 2.8(b), where completely the opposite trend is seen in response to increase in loading. For small to moderate Stokes number, with increase in loading, the flow is highly destabilised, with a sharp drop in critical Reynolds number. At high Stokes number, we see a reduction in the effect of particle loading, and a stabilization this time. The reason for this non-monotonicity could be as follows. Holding fixed the mass fraction f_{max} of particles, as we increase the Stokes number, we are increasing the size of individual particles (from equation 2.8 we see that the particle radius r scales as the square-root of the Stokes number) and therefore reducing the number of particles. Thus, beyond a certain Stokes number, the forcing of the fluid by the particles comes down, and so does the effect of particle loading. We can check the consistency of this argument by examining the effect of Stokes number and mass loading on stability while holding the number density N in equation (2.5) constant. Representative lines of constant N are shown in figure 2.8. Following these lines from low S and f_{max} upwards, we again see different trends under overlap and non-overlap conditions. When the critical and particle-laden layers are distinct (figure 2.8(a)), and the particle number density is low (the two blue lines to the right of the figure), under non-overlap conditions, the critical Reynolds number is practically insensitive to changes in Stokes number and loading, i.e., the lines of constant N appear parallel to lines of constant R_{crit}. This indicates that at small particle number density the critical Reynolds number is practically a function of N. At higher number densities (the two blue lines to the left of the figure) we see a strong stabilising effect with increase in S while N is held constant. This is in sharp contrast to the stability response under overlap conditions, where we see that the effect of increasing Stokes number (and at the same time, mass loading) and constant N is monotonically and strongly destabilising.

Figure 2.8 (c) shows the variation of the critical Reynolds number with a_p and f_{max}. A sharp contrast between the high critical Reynolds numbers of the TS mode and the far lower ones of the overlap mode is evident. At higher levels of f_{max} the critical layer moves away from the wall, and R_{crit} attains values as low as 200 in this range.

Figure 2.9 shows the dependence of the neutral boundaries on f_{max} and a_p. A similar figure appears in Rudyak and Isakov [1996] as well. The longwave mode is absent for smaller particle loading. The longwave mode is odd in u_y whereas the shortwave and TS modes are even. The two even modes can go through merging bifurcations, as seen in figure 2.9(b) at $a_p \sim 0.695$. After merger it is not easy to distinguish the boundary between the TS and the shortwave modes. The entire range of a_p shown in this figure is small, underlining the sensitivity of the stability boundaries to this parameter. The even and odd overlap modes do not merge, but instead show a region of intersection, while each mode retains its character. They may always be distinguished by stipulating for the desired centerline conditions in the numerics. The longwave instability is particularly

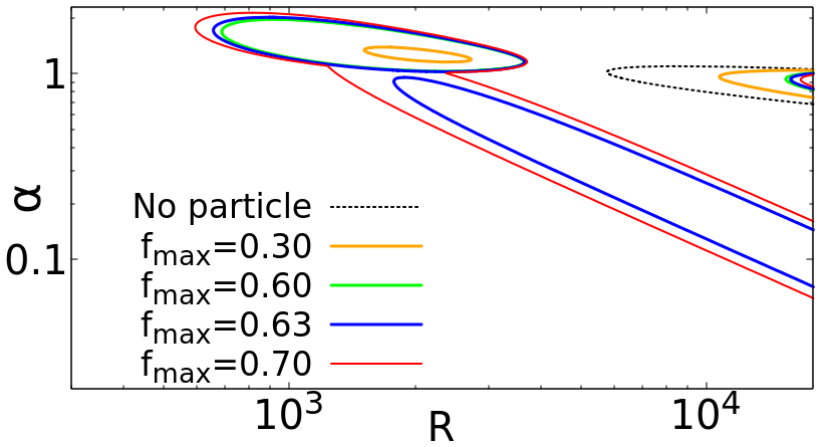

(a)

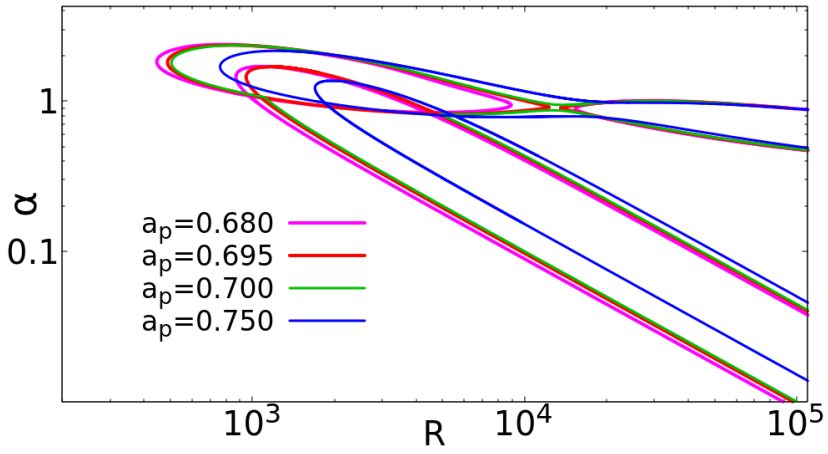

(b)

Figure 2.9: (a) Stability boundaries for different amplitude of particle loading, with $a_p = 0.75$ and $S = 8 \times 10^{-4}$. (b) Sensitive dependence of the stability boundaries on the location a_p of the particle concentration peak. Here $f_{max} = 0.4$, $S = 2.5 \times 10^{-4}$, and $\sigma = 0.1$. The shortwave overlap mode undergoes a merger with the TS mode just past $a_p = 0.695$. Also there is significant intersection between the longwave and shortwave modes.

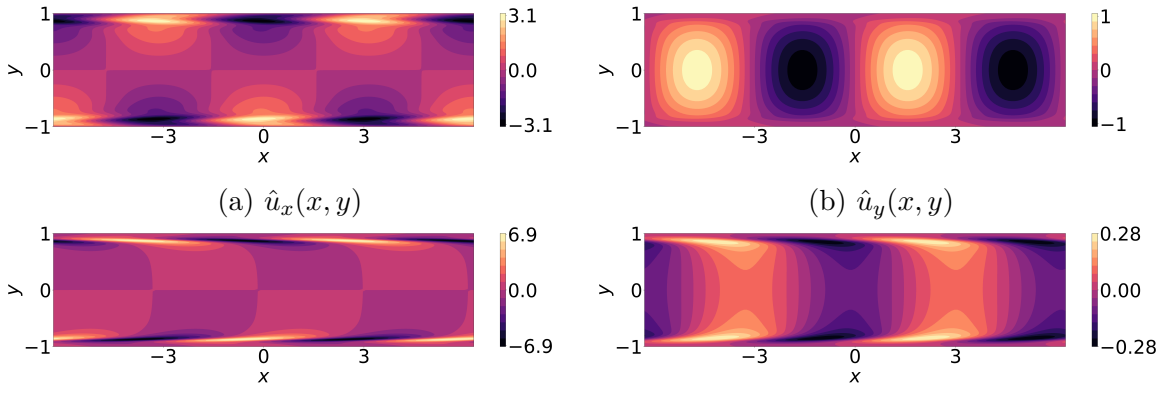

(a) $\hat{u}_x(x, y)$ (b) $\hat{u}_y(x, y)$

(c) $\hat{v}_x(x, y)$ (d) $\hat{v}_y(x, y)$

Figure 2.10: Typical eigenfunctions of the TS mode in the $x - y$ plane. This mode depicts point 'T' in figure 2.5 at $R = 14000$, $\alpha = 1.0$. A streamwise extent of two wavelengths is shown here and for all following eigenfunctions.

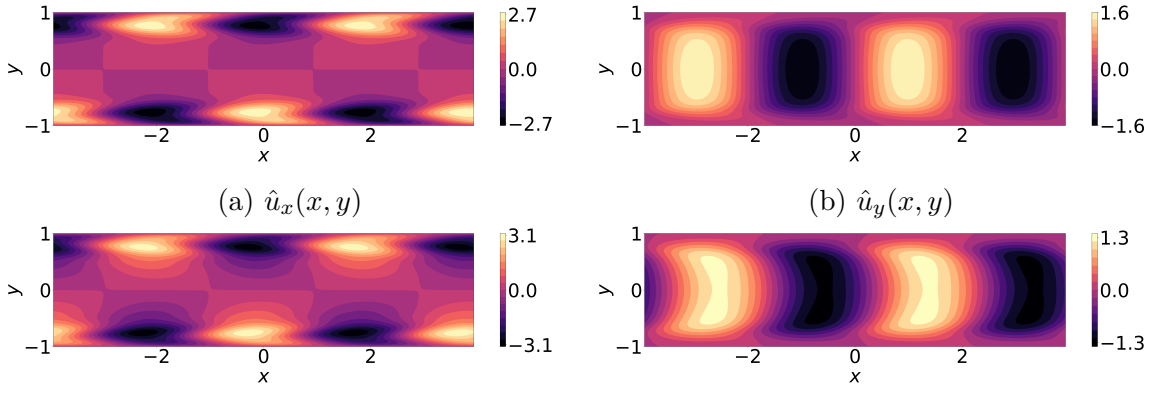

(a) $\hat{u}_x(x, y)$ (b) $\hat{u}_y(x, y)$

(c) $\hat{v}_x(x, y)$ (d) $\hat{v}_y(x, y)$

Figure 2.11: Typical eigenfunctions of the shortwave mode shown at point 'S' in figure 2.5, where R=1000, $\alpha = 1.6$.

interesting because in channel flows, the most unstable perturbations are widely believed to be those which are even, with a maximum at the centreline, in the normal perturbation u_y. This assumption is so widespread that instability computations are often performed in the half-channel by imposing this symmetry at the centreline. Note that we use the terminology 'odd' mode going by the normal perturbation u_y.

The very fact that the longwave mode is odd and the shortwave even means that their eigenfunctions are completely different in character, as seen in figures 2.10 to 2.14. The eigenfunctions have been normalised to set the maximum value of the stream function ψ to unity. The shortwave instability in Figure 2.11 exhibits much stronger streamwise velocity fluid perturbations compared to the TS mode throughout most of the channel, except in a narrow region where the TS streamwise velocity perturbations are pronounced. Also the near-wall structure of the streamwise velocity presents a distinct, wider and more symmetric reverse arrowhead shape than the TS. The eigenfunctions in the particle perturbation velocity components are strikingly different in the shortwave and the TS

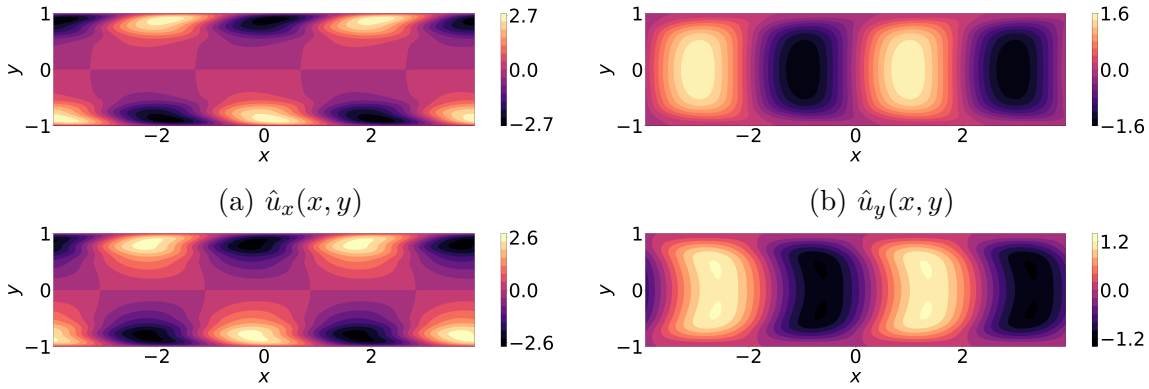

(a) $\hat{u}_x(x, y)$ (b) $\hat{u}_y(x, y)$

(c) $\hat{v}_x(x, y)$ (d) $\hat{v}_y(x, y)$

Figure 2.12: Characteristic eigenfunctions of the shortwave mode, obtained from the minimal composite equation (2.55) using identical parameters as those employed for Figure 2.11.

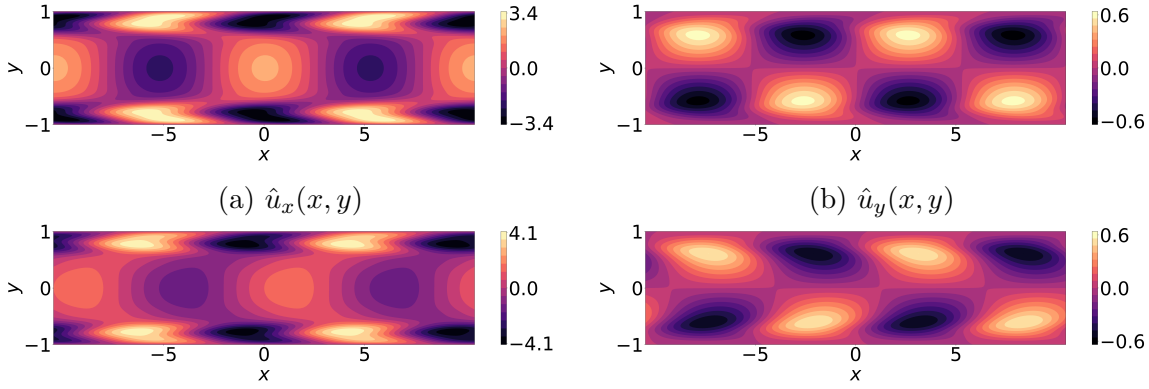

(a) $\hat{u}_x(x, y)$ (b) $\hat{u}_y(x, y)$

(c) $\hat{v}_x(x, y)$ (d) $\hat{v}_y(x, y)$

Figure 2.13: Typical eigenfunctions of the longwave mode, at point 'L' in figure 2.5, where R=3000, $\alpha = 0.6$.

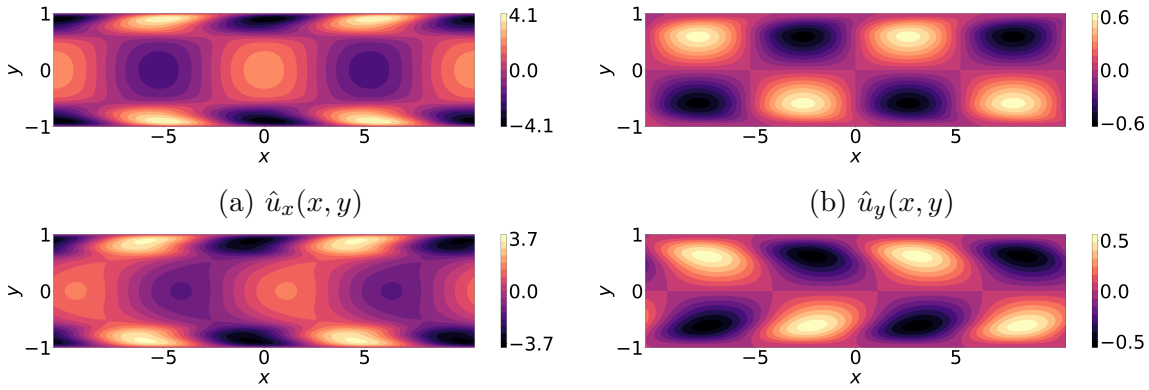

(a) $\hat{u}_x(x, y)$ (b) $\hat{u}_y(x, y)$

(c) $\hat{v}_x(x, y)$ (d) $\hat{v}_y(x, y)$

Figure 2.14: Characteristic eigenfunctions of the longwave mode obtained from the minimal composite equation (2.55) using identical parameters as those employed for Figure 2.13.

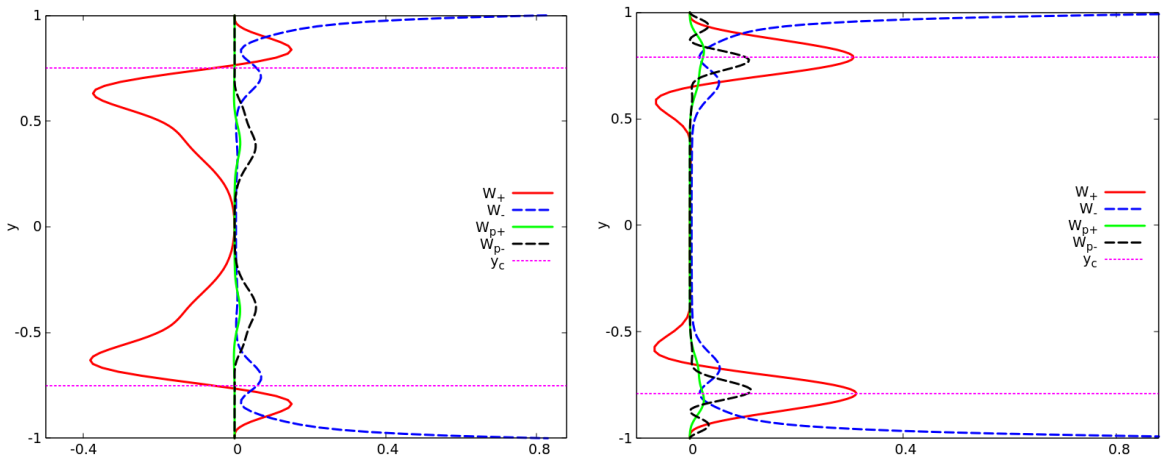

Figure 2.15: Contributions to the perturbation kinetic energy balance at a Reynolds number of 1000 and a streamwise wavenumber of $\alpha = 1.56$, with $f_{max} = 0.30$, $\sigma = 0.1$ and $S = 2.5 * 10^{-4}$. The kinetic energy production W_+ due to the fluid is net negative in (a), where $a_p = 0.40$, but net positive in (b) which is under overlap conditions, with $a_p = 0.75$. The kinetic energy production has a noticeable contribution within the critical layer from particles, W_{p+}, in (b) but not in (a). The dissipation W_- in the flow is similar in the two figures. The location $y = y_c$ is shown by the dashed pink lines.

modes. In the shortwave mode, the particle dynamics is seen to follow the dynamics of the fluid, especially as seen in the streamwise velocity components. The normal velocity component is more peaky for the particles and more rounded for the flow. In contrast, the particles in the TS mode show a thinner region of strong streamwise velocity, but their wall-normal velocity is everywhere weak. The fact that the relevant portions of the eigenfunction profiles are thicker for the shortwave than for the TS mode is a consequence of the lower Reynolds numbers in the former, and we expect this from our critical-layer analysis above. For the shortwave mode, we compare the eigenfunctions from the full solution in figure 2.11 to those from the minimal composite equation in figure 2.12. Though the arrowhead shape is now distorted, the overall similarity in the eigenfunction structure between the two is striking. This is strong visual evidence that the dominant physics is contained in the minimal composite theory.

The eigenstructure of the longwave instability is shown in figure 2.13 from the full equation. Again the eigenfunctions from minimal composite theory, given in figure 2.14, are strikingly similar to those of the complete solution. The energy budgets in the following section will be rendered very surprising, given how different the odd and even modes are in their eigenstructure.

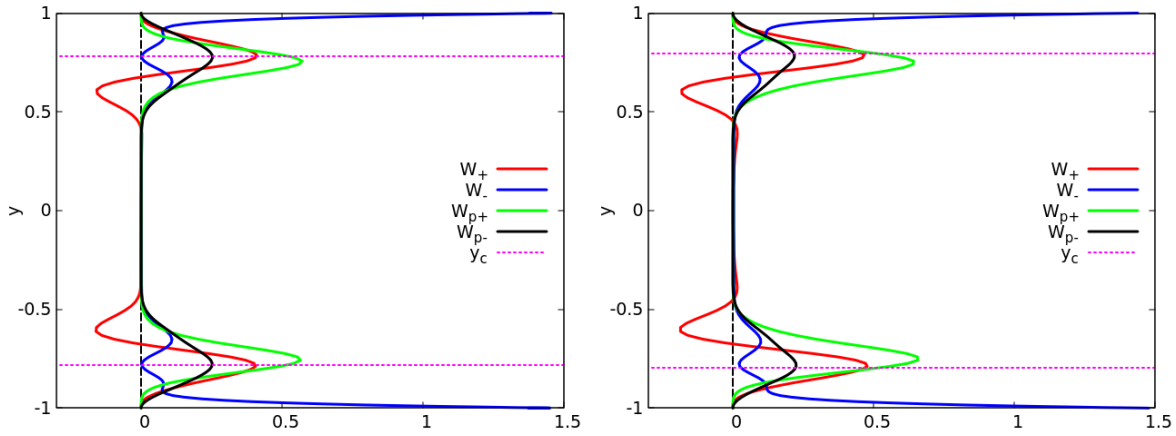

(a) (b)

Figure 2.16: Comparison of contributions to the energy budget in the odd mode (a) at point 'L' in figure 2.5, where $R = 3000$ and $\alpha = 0.6$, with that of the even mode (b) at point 'S' in figure 2.5, i.e., $R = 1000$ and $\alpha = 1.6$. In both, $f_{\max} = 0.70$, $\sigma = 0.1$, $S = 8 \times 10^{-4}$, and $a_p = 0.75$. Both of these modes are unstable, with net production beating dissipation by a small amount.

2.4 Energy production and the critical layer

Figure 2.15 shows the profiles across the channel of the four quantities that contribute to the growth of perturbation kinetic energy, written down in equation 2.30. In the heavy particle limit, the two quantities W_{μ_1} and W_{μ_2} are zero. The parameters are all identical in figures 2.15(a) and 2.15(b), except for a_p, which corresponds to non-overlap conditions in (a) and overlap conditions in (b). The quantities plotted, when combined in the form given in equation 2.30, and integrated over y across the channel, in case (a) give a negative number, i.e., the perturbation is highly damped, whereas this results in a positive number in case (b), indicating an exponentially growing mode. The dissipation quantities W_- and W_{p-} are positive definite by definition. The striking difference between the two figures is in the production of perturbation kinetic energy by the fluid (W_+). In the non-overlap case, the net production is clearly negative, i.e., W_+ is feeding back kinetic energy from the perturbations to the mean flow, and contributing to the decay of the perturbations. Under overlap conditions on the other hand, the production is sharply peaked and positive in the critical layer, leading to the instability. Thus we establish that moving the the particle-laden layer from non-overlap to overlap conditions has a remarkable effect on the solutions to the linear stability problem. Also noticeable is that under non-overlap conditions, there is effectively no contribution to energy production from the particles, i.e., W_{p+} is too small to matter. But in the overlap case, particles contribute directly to the instability as well as by triggering the fluid production. In both cases, W_{p-} is small, and concentrated in the particle-laden layer, while in both cases the fluid dissipates perturbation kinetic energy primarily near the walls (see W_-), i.e., displays

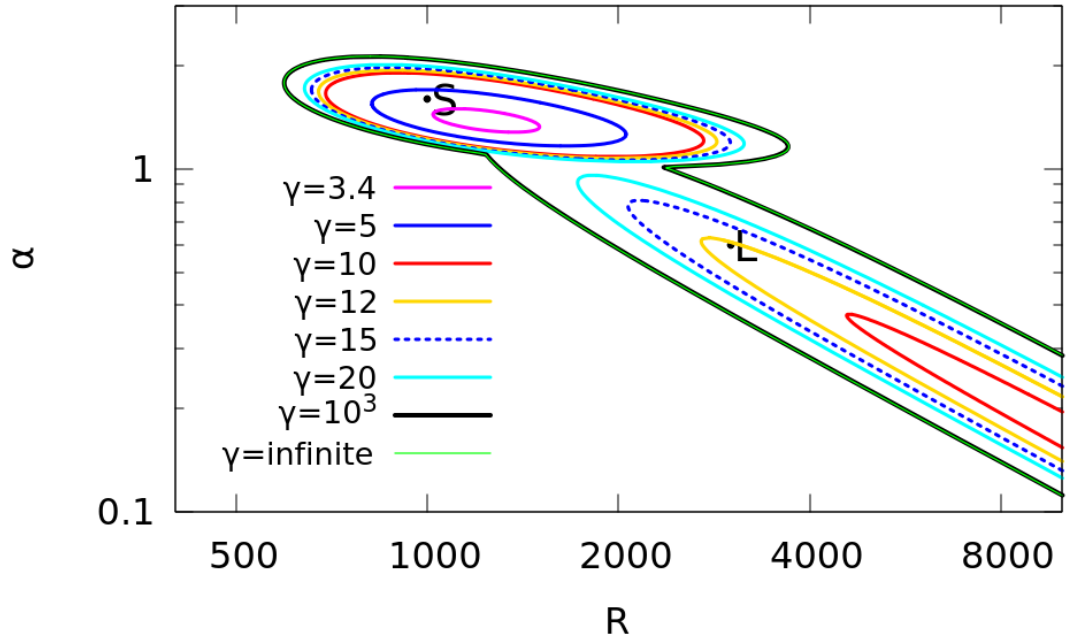

Figure 2.17: Neutral boundaries of the shortwave and longwave modes of instability for various density ratios $\rho_p/\rho_f = 2.5\gamma$. All other parameters are as in figure 2.5, where we had $\gamma \to \infty$.

classical behaviour.

Figure 2.16, comparing the energy budgets of the odd and even mode of overlap instability, holds a surprise. Note that by equation (2.30) this plot is constructed entirely from the eigenfunctions depicted in figures 2.11 and 2.13. The eigenfunctions are completely different in structure, but the energy budgets are very close to each other. Closer observation reveals that the two eigenfunctions are indeed very similar in the neighborhood of the critical and wall layers, which explains the similarity in the production and dissipation. This finding begs the question of the possibility of different eigenstructures in the bulk in different flows yielding critical-layer driven instabilities. We are not aware of any other such situation in shear flows.

2.5 Viscosity stratification

Thus far we have worked in the heavy particle limit, where the mass fraction is finite and the volume fraction of the particles is negligible. We now relax this, and impose a finite particle to fluid density ratio, thereby allowing viscosity to vary in accordance with equation (2.9). The stability equation (2.21) is now applicable, and the mean flow profile $U(y)$ is given by:

$$(\bar{\mu}U')'' = 0, \tag{2.57}$$

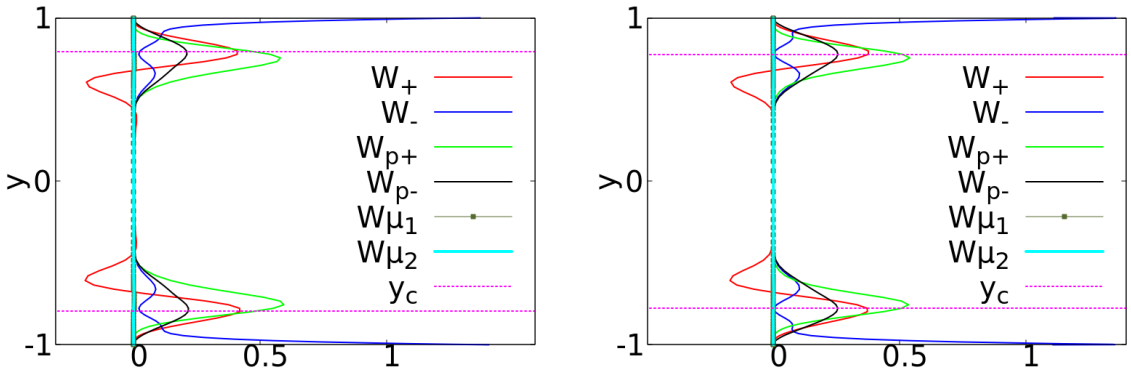

(a) (b)

Figure 2.18: Energy budget for $\gamma = 15$. Profiles of the quantities in equation 2.30 are shown. (a) R=1000, $\alpha = 1.6$, see point 'S' in Fig. 2.17, and (b) R=3000, $\alpha = 0.6$, i.e., point 'L' in that figure. At this γ, both 'S' and 'L' are still unstable.

with the boundary conditions $U(\pm 1) = 0$, and $U(0) = 1$. The effect on the neutral boundaries of the viscosity variation is seen in Fig. 2.17 to be uniformly stabilizing in this flow, with both stability boundaries shrinking significantly as γ is decreased. The longwave mode vanishes below $\gamma = 10$, while a small region of instability persists in the shortwave mode up to $\gamma = 3.4$. The maximum particle volume fraction we have considered occurs for this γ, which is 8 percent at the maximum in the particle layer and lower elsewhere. We ask why this large change happens, since in the critical layer analysis told us that viscosity stratification should not enter the dominant balance at these modest volume fractions. The energy budget for the two modes S and L, which are unstable, is shown for $\gamma = 15$ in Fig. 2.18. We note that the production is very similar to what is seen for no viscosity stratification in Fig. 2.16. But there is practically no contribution from the viscosity variation terms W_{μ_1} and W_{μ_2}. The change in stability is entirely due to the change in the mean profile U.

2.6 Summary and outlook

For decades, shear flows have thrown up surprises in their stability behaviour, and the different mechanisms of instability, though not easy to predict, are crucial to unravel. This is an important reason why these flows are appealing to study. We have persevered to show that the inclusion of particles in a Poiseuille flow is such a case, where we present the mechanism of low Reynolds number instability.

We have shown that the response of the flow to non-uniform particle loading may be divided into two broad categories that we term overlap and non-overlap conditions. Under non-overlap conditions, the particle-laden layer lies at some distance from the critical layer,

where perturbation kinetic energy is produced, and particles do not significantly alter this process. However, when there is an overlap between these layers, there is a dramatic alteration of stability behaviour, with two modes of instability apart from the TS mode appearing. The fundamental difference between overlap and non-overlap conditions is starkly visible in Fig. 2.8 and has been discussed above. Though these modes have been observed in one older study Rudyak et al. [1997] at constant viscosity, they had not been explained before, to our knowledge. The shortwave overlap mode occurs at much lower Reynolds number than the TS mode, and supports wavelengths of the order of the channel width. The longwave overlap mode appears over a wide range of Reynolds numbers and supports wavelengths which could be as small as the channel width but become longer and longer with increasing Reynolds number. This mode is rather unusual in that it is odd in the wall-normal component of the perturbation velocity. The three modes of instability show regimes of distinct existence, and go through interesting intersections and mergers with changes in parameters.

We derive the lowest-order critical and wall layer equations for particulate parallel shear flow for dilute particle loading, and show how they differ from the classical equations for clean flow. This is combined with an energy-budget analysis which brings out the consequences for stability. The reason for the existence of two categories of behaviour is shown to lie in the dynamics within the critical layer. Variations in the base particle concentration within the critical layer significantly alter the production of disturbance kinetic energy. The result is a large destabilisation for this loading profile under a range of conditions. The wall layer is seen not to be a major player. To directly evaluate the lowest-order physics, we derive a minimal composite equation, which contains all the terms in the complete stability equations which contribute at the leading order somewhere in the flow, i.e., in the outer, critical or wall layers. The wall layer contributes no additional terms not present in the other two. The minimal composite equation is shown to contain the essential physics of the overlap instabilities, in terms of trends in the critical Reynolds number and indeed in the eigenfunction behaviour.

In the limit of heavy particles, the volume loading is negligible, so the viscosity is constant. We then consider finite particle to fluid density ratios, where the volume loading is finite but small. Now viscosity varies with particle concentration. The change in the mean flow velocity profile effects a significant stabilisation, whereas the explicit viscosity gradient terms are shown to be non-players in this case. Whether this is a consequence of the special viscosity profile that our loading produces remains to be studied in the future. This question is interesting because in the case of viscosity variations produced by temperature or solute concentration, an overlap mode of instability was predicted by Ranganathan and Govindarajan [2001], Govindarajan [2004] and seen in experiments such as those of Hu and Cubaud [2018]. Related overlap physics can change the nature of

turbulence and the transition to turbulence in heated flow [Giamagas et al., 2024].

The important next question therefore is whether the location of particle loading can affect the transition to turbulence in shear flows. Non-modal linear effects might be important for certain ranges of parameters in this process, and need further attention, in the overlap and non-overlap regimes. Interestingly, when the Reynolds number is about two thousand, nonhomogeneous loading shows exponential growth whereas homogeneous loading [Klinkenberg et al., 2014] shows merely transient growth, indicating that the route to turbulence in the two can be different. Direct numerical simulations are needed to determine the route to turbulence and the possibility of multiple routes due to the different modes of instability. Finally, any theoretical treatment of particulate flow is almost always rife with assumptions whose validity needs to be established by detailed experiments. The effects of geometry are not obvious either, and need investigation. For example, in pipe flow experiments by Matas et al. [2003a,b], at small particle volume fraction, an increase in volume fraction has a destabilising effect in a pipe, whereas for a channel we see stabilisation. It is worth noting that pipe flow differs from channel flow in many aspects. Notably, Squire's theorem, which we have shown here to hold true for channel flow, is not applicable there, so helical modes are often the least stable.

Chapter 3

Horizontal channel flow with slowly sinking particles

3.1 Description of the system and governing equations

This problem is an extension of the previous chapter, with the additional consideration of gravity. Particles which are not neutrally buoyant settle toward the bottom or top wall when their density is greater or less than that of the fluid, respectively. In this study, we assume that the particle is denser than the fluid, with gravity acting in the y-direction. However, the same analysis also applies to a particle that is less dense than the fluid. We work in the limit where the Froude number, defined as $Fr = U_0/\sqrt{gH}$, where U_0, g, and H represent the centerline velocity, gravitational acceleration, and half-channel width, respectively, is much greater than 1. At high Froude numbers, gravitational effects on the fluid momentum equations are negligible. Also, the particle settling is slow, which means that transient variations in the mass fraction profile occur over long timescales. As the instability analysis focuses on much shorter timescales, these transient effects can be neglected, allowing the base flow to be treated as quasi-steady for stability analysis. We find in this limit that gravitational effects appear in the stability problem solely through the mean mass fraction profile. The model mean mass fraction of the particles is given by

$$\bar{f} = 0.5 f_{max} \left[1 + \tanh\left(\frac{y - a_p}{\sigma} \right) \right]. \tag{3.1}$$

The particle concentration is zero away from the bottom wall and reaches f_{max} near this wall, with the transition occurring around $y = a_p$ within a band of size 2σ. The schematic of the quasi-steady state of the problem is shown in Figure (3.1). The added mass term is

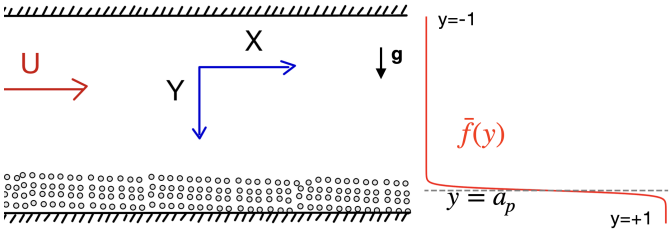

Figure 3.1: Schematic illustrating the flow under study: particles in a quasi-steady state settling under the influence of gravity. For finite-size particles, the mean particle distribution leads to a change in viscosity in the region where particles are present. This viscosity variation affects the mean velocity profile. A representative profile is shown in Figure (3.2).

now included in the particle equation 2.3. Consequently, the linearized equations (3.2-3.5)

$$\begin{aligned}-i\alpha c(D^2-\alpha^2)\psi =& i\alpha\left[U''-U(D^2-\alpha^2)\right]\psi+\frac{1}{R}\left[\bar{\mu}\left(D^2-\alpha^2\right)^2+\bar{\mu}''\left(D^2+\alpha^2\right)+2\bar{\mu}'\left(D^3-\alpha^2 D\right)\right]\psi\\ &-\frac{1}{SR}\left[\bar{f}'D+\bar{f}(D^2-\alpha^2)\right]\psi+\frac{1}{R}\left[U'''+2U''D-U'(D^2-\alpha^2)+2U'D^2\right]\mu\\ &+\frac{1}{SR}\left[(\bar{f}'+\bar{f}D)v_x-i\alpha\bar{f}v_y\right]\end{aligned} \tag{3.2}$$

$$-i\alpha c v_y+\alpha^2 c\mathcal{Q}\psi=-\left(i\alpha U+\frac{3-\mathcal{Q}}{3SR}\right)v_y-i\alpha\left(i\alpha U\mathcal{Q}+\frac{3-\mathcal{Q}}{3SR}\right)\psi \tag{3.3}$$

$$\begin{aligned}-i\alpha c v_x+i\alpha c\mathcal{Q}D\psi=&-\left(i\alpha U+\frac{3-\mathcal{Q}}{3SR}\right)v_x-U'v_y\\ &+\left(i\alpha U\mathcal{Q}+\frac{3-\mathcal{Q}}{3SR}\right)D\psi-i\alpha\mathcal{Q}U'\psi\end{aligned} \tag{3.4}$$

$$\alpha c\gamma\mu=\alpha U\gamma\mu-i\left(\bar{f}'+\bar{f}D\right)v_y+\alpha\bar{f}v_x \tag{3.5}$$

where $\mathcal{Q}=3/(5\gamma+1)$, with all terms involving $\mathcal{Q}$ corresponding to added–mass effects, and the boundary conditions

$$\psi(\pm1)=D\psi(\pm1)=v_x(\pm1)=v_y(\pm1)=\mu(\pm1)=0 \tag{3.6}$$

differ from those in the previous chapter solely due to the addition of the added mass term, while the mean velocity equation remains as it is, as given in 2.57. The mean velocity profile and the mean viscosity caused by the dilute particle suspension are given in Figure (3.2). We observe that the velocity profile becomes inflexional for sufficiently small particle density ratios.

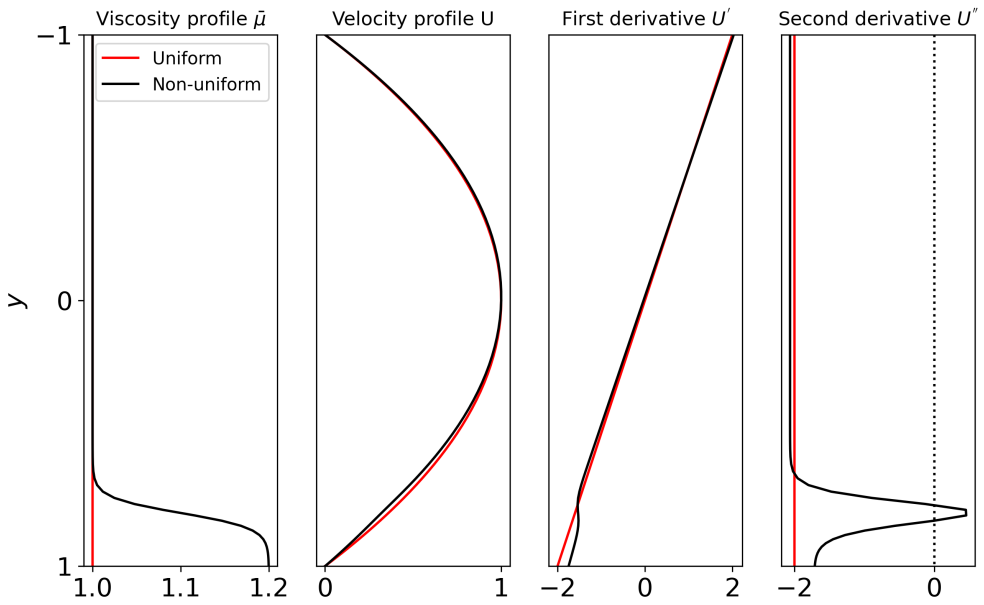

Figure 3.2: From left to right, the first plot shows the mean viscosity for the finite particle volume fraction (black curve) and the uniform viscosity case (red curve). The resulting viscosity stratification causes slight deviations in the velocity profile and its first and second derivatives (black curves) compared to the uniform viscosity case (red curves), with noticeable differences appearing in the region of viscosity variation. The parameters used for the plot are $S = 8 \cdot 10^{-4}$, $f_{\max} = 0.1$, $\sigma = 0.0578$, and $a_p = 0.80$.

3.2 Results and summary

The stability result of a quasi-steady state is presented in Fig.3.3, revealing that for finite

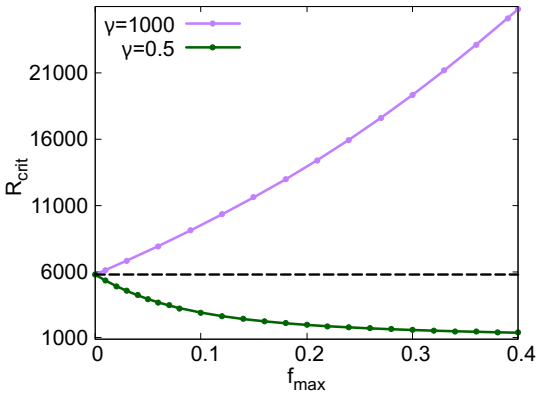

Figure 3.3: The critical Reynolds number decreases monotonically with increasing mass loading for particles with a finite particle-induced viscosity, as shown by the green curve. In contrast, for particles with a negligible contribution to viscosity, it increases monotonically, as depicted by the purple curve. The black dashed line indicates the critical Reynolds number of the clean flow. The parameters are $f_{max} = 0.1, S = 8 \cdot 10^{-4}$, $a_p = 0.85$, and $\sigma = 0.0578$.

particle-induced viscosity, these states are more unstable than the clean flow. In contrast, when particle-induced viscosity is negligible, large stabilization occurs. This difference becomes more pronounced as the particle loading strength increases. Note that for a given mass fraction profile, a large particle-to-fluid density ratio ($\propto \gamma$) results in a negligible volume fraction, making the particle-induced change to viscosity insignificant. However, for a finite particle-to-fluid density ratio, the induced effect on viscosity becomes finite, and its stratification occurs at the same location as the transition region of the mass fraction profile (i.e. a_p). Figure (3.4) further illustrates that flow destabilization occurs when the region of the viscosity stratification is close to the wall.

From Figure (3.5), we make an interesting observation: the particle-induced viscosity stratification, in itself, through the terms it contributes to the linearised equations (3.2-3.5), has only a partial direct impact on stability. The same is true for the added-mass terms. A big reason for the destabilization is the alteration in the mean velocity U caused by particle-induced viscosity stratification. The profile shows a tendency toward developing an inflection point.

We had seen in chapter 2 that viscosity variation introduced by the suspension of particles had a stabilizing effect when the particles were concentrated away from the channel walls. However, in the present case, when particles occupy the region close to the bottom wall, I find that particle-induced viscosity stratification has the opposite effect on flow stability. To understand why a viscosity variation of this kind causes destabilization, I compared the results with those of a one-peak Gaussian-shaped mass fraction profile

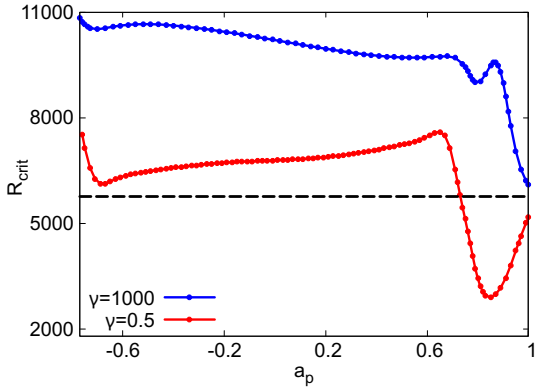

Figure 3.4: Significant stabilization occurs when particle-induced viscosity is negligible, as shown by the blue curve. However, for a finite particle volume, destabilization arises when the viscosity stratification region, represented by a_p, is near the wall, as indicated by the red curve. The black dashed line indicates the critical Reynolds number of the clean flow. The parameters are $f_{max} = 0.1, S = 8 \cdot 10^{-4}$, and $\sigma = 0.0578$.

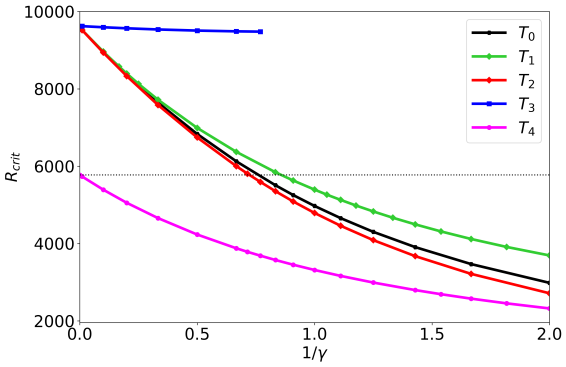

Figure 3.5: Key instability-inducing terms in the governing equations are examined. The instability arises due to changes in the mean velocity profile caused by particle-induced viscosity stratification. The critical Reynolds number decreases monotonically with increasing viscosity strength when solving the full equation, represented by curve T_0. Dropping the added mass terms results in minimal change, as shown by curve T_1. Similarly, when viscosity terms are removed except in the mean velocity, the change remains minimal, represented by curve T_2. However, when viscosity is omitted only in the mean velocity, the critical Reynolds number remains nearly constant with viscosity strength, as seen in curve T_3. Finally, removing the mass fraction and particle viscosity terms except in the mean velocity leads to a further decrease in the critical Reynolds number, which continues to decrease with increasing viscosity strength, represented by curve T_4.The parameters are $f_{max} = 0.1, a_p = 0.87, S = 8 \cdot 10^{-4}$, and $\sigma = 0.0578$.

$\bar{f} = 0.5 f_{max} \left[\tanh\left(\frac{y-a_{p_1}}{\sigma}\right) - \tanh\left(\frac{y-a_{p_2}}{\sigma}\right)\right]$, inspired by the problem in chapter 2. I begin with a set of parameters, similar to those in Figure 2.5, that preserve the instability modes observed there. Then gradually a parameter of the mass fraction profile is varied to obtain a profile similar to what I have in this gravity case; $\bar{f} \approx 0.5 f_{max} \left[\tanh\left(\frac{y-a_{p_1}}{\sigma}\right) + 1\right]$ for $a_{p_2} \gg 1 + \sigma$. From Figure (3.6), we observe that destabilization occurs due to viscosity

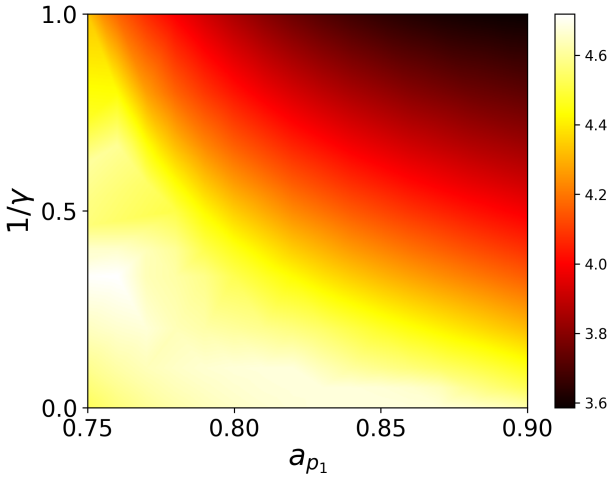

Figure 3.6: The parameters used are $f_{max} = 0.903$, $S = 8 \cdot 10^{-4}$, $\sigma = 0.0968$, and $a_{p_2} = a_{p_1} + 0.2$. The color scale represents the base-10 logarithm of the critical Reynolds number. For a fixed a_{p_1}, the critical Reynolds number initially increases with the induced viscosity ($\propto 1/\gamma$), reaches a peak, and then decreases. At a fixed induced viscosity, it initially decreases as a_{p_1}, the location of the rising arm of the mass fraction, shifts towards the wall, reaching a minimum before increasing again and asymptotically approaching the critical Reynolds number of the clean flow.

stratification near the wall (see around $a_{p_1} = 0.90$) is high. When the peak is close to the wall, as in the case $a_{p_1} = 0.90$, the mass fraction profile exhibits a strictly increasing trend across the channel. In contrast, when the peak is farther from the wall, the profile contains both increasing and decreasing regions. The peak of the profile can be shifted further towards the wall to approximate the form given in equation (3.1). However, this adjustment leads to a substantial reduction in average mass loading, eventually rendering it negligible.

To determine whether destabilization arises from changes in the shape of the mass fraction profile or the viscosity profile, we examine a scenario where the particle terms are removed from the governing linearized equations while maintaining the same mean velocity profile (i.e. the mean velocity contains the particle's effect). Interestingly, this modification results in even greater destabilization, as illustrated in Figure 3.5. This observation strengthens the suggestion that the change in the velocity profile arising out of the particle-induced viscosity stratification plays a crucial role in the destabilization.

The effect of viscosity profile changes on instability can be further understood by

analyzing its neutral curves. To assess this impact, we examine the shape, location, and strength of the largest viscosity variation. In Figure 3.7, the mass fraction used for the

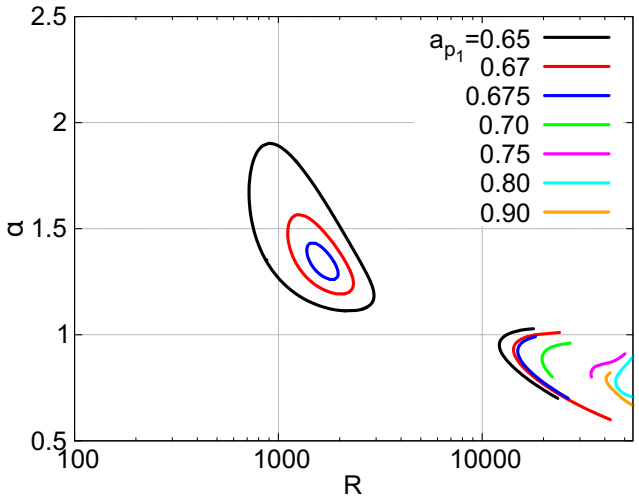

Figure 3.7: The shortwave mode disappears when viscosity variation regions are shifted sufficiently toward the wall. The parameters used are $f_{max} = 0.903$, $S = 8{\cdot}10^{-4}$, $\sigma = 0.0968$, $\gamma = 1000$, and $a_{p_2} = a_{p_1} + 0.2$.

black curve is similar to that in Figure 2.5 of Chapter 2, with the key distinction being the presence of a single peak instead of two. The neutral curves exhibit a similar pattern, featuring identical shortwave and TS modes, but with the longwave mode absent. As the mass fraction peak shifts closer to the nearest wall while keeping other parameters fixed, both modes become stabilized; the S-mode shrinks and quickly disappears. Consequently, the critical Reynolds number is later determined by the TS mode. Meanwhile, in Figure 3.8, when the particles have a finite size, the induced viscosity stabilizes both modes, with the S-mode rapidly shrinking. This outcome resembles the results obtained for the two-peaked mass fraction profile, as shown in Figure 2.17.

Suppose the peak of the mass fraction profile is shifted further toward the wall, to the extent that the decaying arm nearest to the wall extends beyond the domain and is no longer present in the mass fraction. In that case, the resulting profile represents the model mass fraction under the influence of gravity. The neutral curves for such mass fraction profiles are shown in Figure 3.9. It can be observed that only the TS mode remains, and it becomes destabilized due to the induced particle viscosity. The destabilization caused by induced viscosity can be attributed to the increase in particle volume fraction as the particle density γ decreases, leading to higher viscosity. This behavior contrasts with the two-peak Gaussian profile discussed in Chapter 2. When the viscosity variation reaches the wall, the mechanism is different, as explored by Ranganathan and Govindarajan [2001], Govindarajan [2004]. The key mechanism is that a positive viscosity gradient, where viscosity is higher near the wall than in the inner channel, induces a destabilizing effect, while a negative gradient promotes stabilization. The origin of this

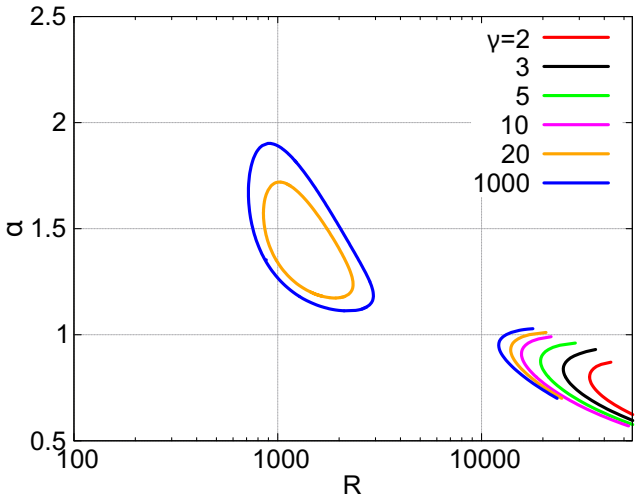

Figure 3.8: For sufficiently high viscosity variation with both increasing and decreasing regions in the profile, the shortwave mode disappears. The TS mode also stabilizes but persists, ultimately determining the instability. The parameters used are $f_{max} = 0.903$, $S = 8 \cdot 10^{-4}$, $\sigma = 0.0968$, $a_{p_1} = 0.65$, and $a_{p_2} = a_{p_1} + 0.2$.

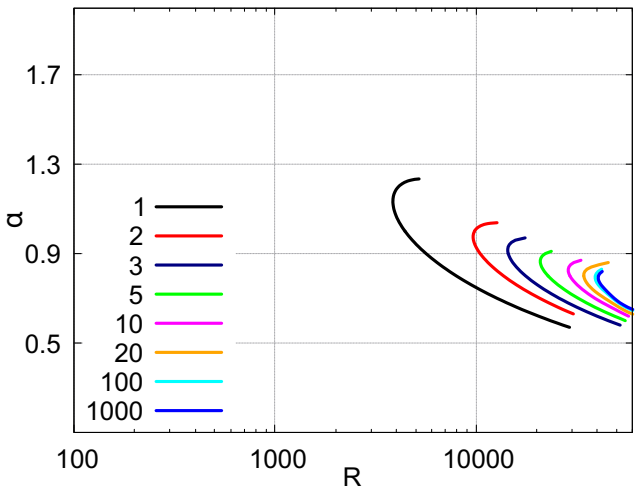

Figure 3.9: Enhanced destabilization of the TS mode with increasing induced viscosity. The parameters are $f_{max} = 0.903$, $S = 8 \cdot 10^{-4}$, $\sigma = 0.0968$, $a_{p_1} = 0.90$, and $a_{p_2} = a_{p_1} + 0.2$.

low Reynolds number instability mode can be attributed to the tendency of the velocity profile to develop an inflection point. As the induced viscosity varies, the maximum of U'' approaches zero (see figure 3.10). Near this point, the mean velocity profile is

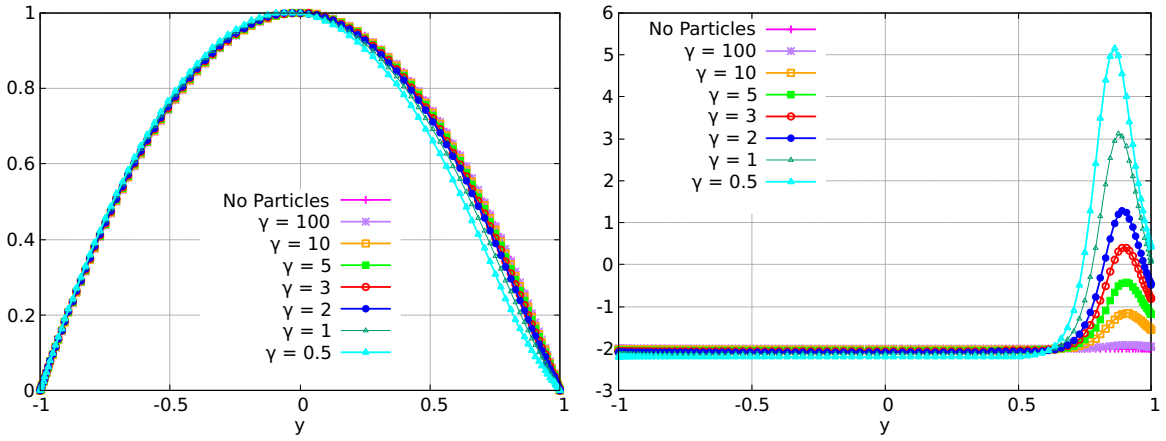

Figure 3.10: Variation of mean velocity and its second derivative with γ is shown in (a) and (b) respectively. The parameters used are $f_{max} = 0.903$, $S = 8 \cdot 10^{-4}$, $\sigma = 0.0968$, $a_{p_1} = 0.90$, and $a_{p_2} = a_{p_1} + 0.2$.

governed by $-2 = \bar{\mu}U'' + \bar{\mu}'U' \approx \bar{\mu}'U'$ for a high viscosity gradient. Since $\bar{\mu}' \sim O(1/\epsilon)$, where $\epsilon \ll 1$, and $U'' \to 0$ with $\bar{\mu} \sim O(1)$, it implies that $U' \sim O(\epsilon)$. This scaling for U' under viscosity stratification, i.e., $U' \sim O(\epsilon)$, differs significantly from the case without stratification, where $U' \sim O(1)$. Consequently, at low Reynolds numbers, this leads to a different lowest-order governing equation compared to the one derived for the overlap mechanism in chapter 2, giving rise to the observed instability modes.

When the induced viscosity becomes sufficiently strong, the mean velocity profile becomes inflectional, leading to the emergence of an additional instability mode, referred to as the "inviscid mode". This mode overlaps with the Tollmien-Schlichting (TS) mode, as shown in Figure 3.11. In this figure, the lower curve corresponds to the TS mode, while the upper curve represents the inviscid mode. For $a_{p_1} = 0.75$, the TS mode is more stable and does not appear within this Reynolds number range, leaving only the inviscid mode. As the mass fraction peak shifts toward the wall, or as a_{p_1} increases, the TS mode emerges, whereas the inviscid mode curve remains largely unchanged. In this case, the critical Reynolds number is determined by the inviscid mode. With a further shift of the mass fraction peak toward the wall, the TS mode moves toward lower Reynolds numbers, with its inner portion merging into the inviscid mode curve, while the outer portion of the inviscid mode remains nearly unchanged. When the mass fraction peak moves even closer to the wall, making the mass fraction profile resemble the model profile for the gravity-driven case, the instability Reynolds number is ultimately determined by the TS mode. In summary, the destabilizing influence of viscosity in this case is not the opposite

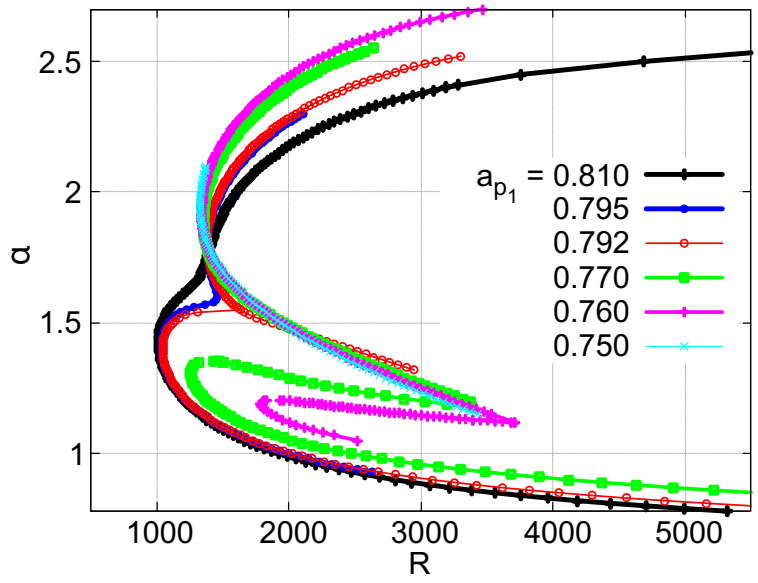

Figure 3.11: The emergence of a distinct instability mode, the inviscid mode, at relatively high particle-induced viscosity, along with the TS mode which appears, merges, and becomes dominant as the peak location shifts toward the wall. The parameters are $f_{max} = 0.903$, $S = 8 \cdot 10^{-4}$, $\sigma = 0.0968$, $\gamma = 0.5$, and $a_{p_2} = a_{p_1} + 0.2$.

of its role in the zero-gravity situation discussed in chapter 2. The destabilization observed here occurs because the particles are sufficiently close to the wall. Thus, viscosity acts in two ways: it stabilizes the flow when particles are far from the wall, and destabilizes it when particles are near the wall. These trends are independent of the specific model mass-fraction profile; a Tanh, Gaussian, or any other profile that captures the qualitative distribution of particles yields the same behavior.

Chapter 4

On the intense sensitivity to wall convergence of instability in a channel

This work presented in this chapter has been published in our *Physics of Fluids* article Kumar and Govindarajan [2024a].

4.1 Introduction

In this study we return to the classical problem of linear instability in channel flow, ask why we see dramatic effects with a small tilt of the walls, and offer a partial answer. In doing this, we hope to encourage future close examination of a problem which has fundamental questions as well as immediate applications. In practical applications, we know that it is extremely difficult to manufacture a pipe or channel that is perfectly straight, and if a small departure from being absolutely straight has such a profound effect on stability, this feature should surely be taken into consideration while drawing conclusions about the transition to turbulence.

The laminar flow through channels whose walls converge or diverge at a constant angle is described by the Jeffery-Hamel (JH) equations (Jeffery [1915], Hamel [1917]). Eagles [1966] calculated the critical Reynolds number, R_{crit}, at which the first linear instability is seen, for diverging channel flow. They noticed that R_{crit} falls steeply compared to that in a straight channel. For a straight channel, $R_{crit} = 5772.2$ (see Orszag [1971]) whereas with a wall divergence of only 0.04 degree, $R_{crit} \sim 2000$. Note that this divergence is so small that a channel built with such a divergence would be indistinguishable visually from a straight one. The reason for this sharp fall is an open question, with some beginnings having been made by Swaminathan et al. [2011]. On the other hand are channels with a small angle of convergence. The stability of this flow, to our knowledge, was first studied by Fujimura [1982]. A sharp increase in the critical Reynolds number with the smallest convergence was seen. The sensitivity to convergence angle is even more stark than to

divergence.

The focus of this chapter is on converging channel flow, and the scope is three-fold. First, it is known that the Jeffery-Hamel equations support non-unique laminar flow solutions in the channel. One solution is just a profile very close to parabolic, but the others have more than one extremum. We investigate a few of these for their stability, and we show that at low Reynolds numbers, we may have more than one stable laminar flow velocity profile in convergent JH flow. Incidentally, Drazin [2002] found multiple stable solutions in a related flow: of a geometry with converging and diverging sections separated by a straight section. We hope our findings about JH flow will motivate low Reynolds number experiments to see if several velocity profiles can be displayed under identical conditions with very minor tilt of the walls. Second, we focus on the one-lobed profile which reduces to the parabolic for a straight channel, and show how the extreme sensitivity to changes in the mean flow arises out of an alteration in the lowest-order balance within the critical layer of the dominant perturbation. In other words, a fundamental change in the nature of stability takes place. We also discuss the relevance of our findings in the context of our earlier study by Jotkar and Govindarajan [2017, 2019] on transient growth in convergent and divergent channels. A related system is studied by Jotkar et al. [2016]. A third aspect is that a pipe and of a channel are usually thought to be very different in their linear stability. A pipe is often likened to a plane-Couette flow, since both of these are stable at any Reynolds number to perturbations consisting of individual linear eigenmodes, whereas a channel goes unstable at a finite R_{crit}, as stated above. But with a small tilt of the walls, a broad similarity between the two is seen.

It is recognized that laminar-flow solutions to the JH equation are not unique [Drazin, 2002]. Interestingly, multiple solutions exist which satisfy the same third-order differential equation and all its boundary conditions in the same geometry, and these have been classified into five distinct types by Fraenkel and Squire [1962]. Of these, Type III_1 is a one-lobed profile, which for small tilt angles, θ, is very close to a parabolic velocity profile. The naming convention of the mean flows is described in Section III A. The linear stability of parallel shear flows is described by the Orr-Sommerfeld equation [Schlichting and Gersten, 2016, Drazin and Reid, 2004]. Fujimura [1982] analyzed the stability of this type of mean flow by employing a local turning point approximation. On the other hand, we use a direct numerical technique to solve the Orr-Sommerfeld (OS) equation for the III_1, III_2, and III_3 types of profiles. We accurately compute the mean flow using a 4th-order Runge-Kutta method combined with a Newton-Raphson algorithm to converge on the right boundary conditions.

4.2 The governing equations and their solution

4.2.1 Base flow

The JH equation provides the steady state of two-dimensional laminar flow of an incompressible fluid within an infinite wedge, driven by a source/sink located at the intersection of the rigid planes forming the wedge, a schematic is shown in Figure 4.1 . It is a similarity

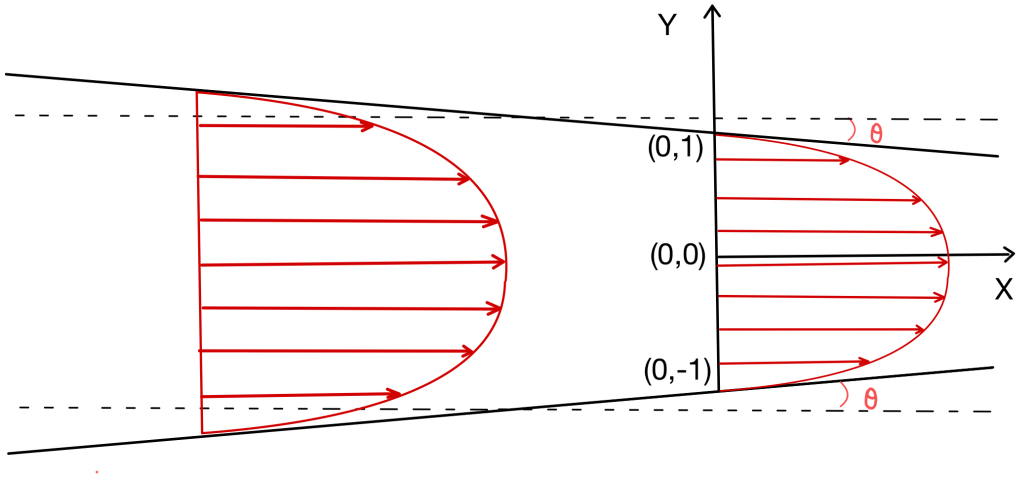

Figure 4.1: Schematic illustrating a convergent channel flow with a Type III_1 velocity profile. We emphasise that the angle of convergence is grossly exaggerated for clarity of viewing, compared to the range we study here. The x-axis is oriented along the channel centerline and the y-axis intersects the channel walls at an angle of $\pi/2 - \theta$. The lengths are non-dimensionalized using the local half-channel width H, placing the walls at $y = \pm 1$. Note that θ is negative.

equation given by

$$U''' + 2S_0 UU' + 4\theta^2 U' = 0, \tag{4.1}$$

with the boundary conditions

$$U(+1) = U(-1) = 0; \quad U(0) = 1, \tag{4.2}$$

where U is the streamwise velocity nondimensionalised by the centerline velocity U_{ce}. The angle made by the rigid walls with respect to the channel centerline (the x-axis) is denoted by θ, as illustrated in Figure(4.1). An important parameter in this problem is $S_0 \equiv \theta R$. Note that in convergent flow, θ, and therefore S_0, are negative. The Reynolds number $R \equiv \frac{|Q|}{\nu}$, where $Q = U_{ce}(x_d)H(x_d)M_U$ is the net mass flux through the channel, where $H(x_d)$ is the local channel half-width, or the distance of the wall from the centerline, and ν is the kinematic viscosity. For a constant tilt angle, we may approximate flow in the convergent channel to that going towards a sink at a location x_L, which lies extremely far downstream, so $H = (x_L - x_d)\tan|\theta|$ and $U_{ce} \propto 1/H$. A prime denotes a derivative with

respect to a similarity coordinate y, which is the coordinate normal to the centerline non-dimensionalized by $H(x)$. The non-dimensional mass flux is given by $M_U = \int_{-1}^{+1} U(y)dy$. Given that the net mass flux must be constant through all x, the Reynolds number too is constant throughout. It will become useful to define another Reynolds number, $R_{SC} = U_{ce}(x)H(x)/\nu$. The Reynolds numbers are related as $R = R_{SC}|M_U|$. Upon integrating Equation (4.1), we get

$$U'' - U''_w = -S_0 U^2 - 4\theta^2 U, \tag{4.3}$$

where the subscript w indicates a quantity at the wall, i.e. at $y = \pm 1$. Another integration yields

$$U'^2 - U'^2_w = -\frac{2}{3} S_0 U^3 + 2U''_w U - 4\theta^2 U^2. \tag{4.4}$$

The quantities at the wall are as yet unknown, and will be arrived at by our numerical procedure.

4.2.2 Stability analysis

At the tiny wall tilt-angles imposed here, the streamwise change in the base flow is extremely small, and for all practical purposes we may treat the flow as being parallel. In other words, we neglect the mean wall-normal velocity. Under this assumption, the flow stability is described by the Orr-Sommerfeld equation,

$$\mathcal{L}_{OS}\psi = -i\omega \left(D^2 - \alpha^2\right)\psi, \tag{4.5}$$

where

$$\mathcal{L}_{OS} = -i\alpha U \left(D^2 - \alpha^2\right) + i\alpha U'' + \frac{1}{\mathrm{R}} \left(D^2 - \alpha^2\right)^2, \tag{4.6}$$

$D \equiv d/dy$ and the boundary conditions are

$$\psi(y = \pm 1) = D\psi(y = \pm 1) = 0. \tag{4.7}$$

The perturbation stream function has been represented as

$$\hat{\psi} = \frac{1}{2}\Big[\psi(y)\exp\left[i(\alpha x - \omega t)\right] + \psi^*(y)\exp\left[-i(\alpha x - \omega t)\right]\Big], \tag{4.8}$$

where $c = \omega/\alpha$ denotes the complex phase speed, and the perturbation velocity components are $\hat{u_y} = -i\alpha\hat{\psi}$ and $\hat{u_y} = D\hat{\psi}$. An application of Squire's 1933 theorem [Squire, 1933] has enabled us to write a two-dimensional version of this problem, since all three-dimensional perturbations will go unstable at higher Reynolds numbers than a corresponding two-dimensional one.

We numerically solve equation (4.5) by employing the Chebyshev spectral collocation method to discretize it at n collocation points in the domain of y within (-1,1). Subsequently, the discretized eigenvalue matrix equation is solved using the LAPACK package. We choose the values of n to be 81, 101, 121, and 161 in order to achieve accuracy of at least 6, but most often 8, decimal places.

4.2.3 Energy budget

When the flow becomes unstable, there is exponential growth in perturbation kinetic energy. We can separate the positive and negative factors contributing to this growth. To do this, the linearized Navier-Stokes equation for the fluid flow (in $\hat{\mathbf{u}}$) can be multiplied by the complex conjugate velocity $\hat{\mathbf{u}}^*$. By averaging over a wavelength in the streamwise direction, we can obtain the evolution of perturbation kinetic energy $\hat{E}$ as described by:

$$\partial_t \int \hat{E} dV = -\int \frac{\partial U_i}{\partial x_j} \hat{u}_i \hat{u}_j, dV - \frac{1}{R} \int |\partial_i \hat{u}_j|^2 \, dV \tag{4.9}$$

where

$$\hat{E} = \frac{1}{2} \hat{u}_i^2, \tag{4.10}$$

and V indicates a volume of fluid extending from wall to wall and over one perturbation wavelength in the streamwise direction. We then introduce the normal-mode forms of the perturbations, given by equation (4.8), into equation (4.9), and average over the streamwise direction x, to get

$$\begin{aligned} 2\alpha c_{im} \int E \, dy &= -\frac{1}{4} \int \frac{\partial U_i}{\partial x_j} \left(u_i u_j^* + u_i^* u_j \right) \, dy - \frac{1}{2R} \int |\partial_i u_j|^2) \, dy \\ &\equiv \int (W_+ - W_-) dy, \end{aligned} \tag{4.11}$$

where

$$E(y) = \frac{1}{4} |u_i(y)|^2, \tag{4.12}$$

and $W_+(y)$ and $W_-(y)$ are the production and dissipation of perturbation kinetic energy, respectively.

4.3 Results

4.3.1 Mean velocity profiles and anticipated stability behaviour

We solve for equation (4.1) with the boundary conditions (4.2) to obtain the base velocity U. There are infinite solutions possible, which have been categorized into five types by

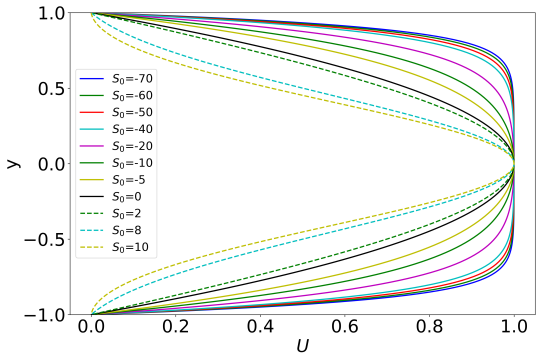

Figure 4.2: Type III_1 velocity profiles (for a convergent channel, $S_0 < 0$) and their variation with S_0. The black solid curve shows the parabolic profile for a straight channel ($S_0 = 0$), while the dashed curve shows the corresponding one-lobed profile for a divergent channel ($S_0 > 0$).

Fraenkel and Squire [1962]: I_n, II_n, III_n, IV_n and V_n. Diverging flows encompass I_n, II_n IV_n, while converging flows fall under III_n, IV_n and V_n. Types I_n, II_n and III_n are symmetric velocity profiles, while IV_n and V_n are asymmetric, and mirror images of each other. The subscript n indicates the number of zeroes within the flow: $2n-2$ for symmetric and $2n-1$ for asymmetric profiles.

We restrict our investigation here to symmetric flows falling under the category III_n. These solutions are obtained numerically, and the first in the series, i.e., profiles of type III_1, are shown in Figure 4.2 for convergent and divergent channels. Here we have used the small-angle approximation, wherein the quadratic term in θ is neglected, resulting in the mean velocity depending solely on the single parameter S_0. We see that as the magnitude of S_0 increases in the convergent channel ($S_0 < 0$), the mean velocity profile becomes progressively broader. Conversely, in the divergent channel, the profile becomes increasingly sharp as S_0 increases, and in fact we get flow separation at higher S_0. The qualitative features of the mean velocity profile are further understood by examining their second derivatives, shown in Figure (4.3) . All the variation moves progressively closer to

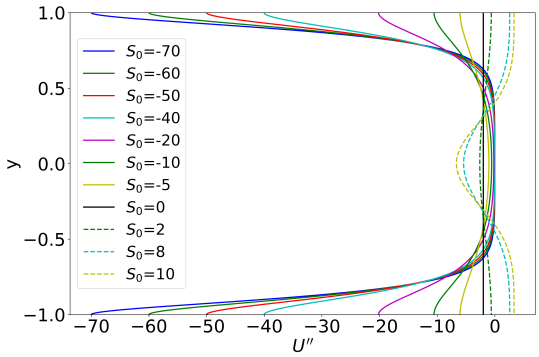

Figure 4.3: Dependence of the second derivative of mean velocity (U'') on S_0. Note that as S_0 becomes large and negative, $U''_w \sim S_0$.

the walls as S_0 becomes more negative.

The next few members of the type III series of velocity profiles, obtained by solving the complete equation (4.1), are presented in Figure 4.4 . We begin the solution at

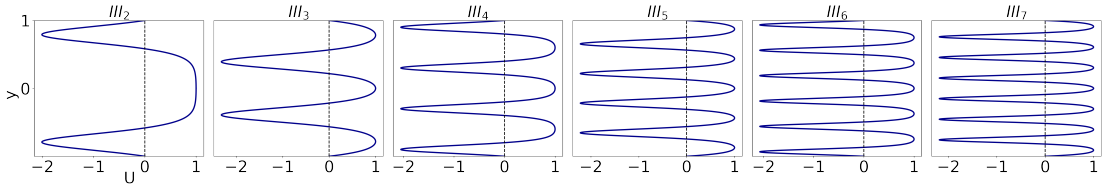

Figure 4.4: Laminar velocity profiles of type III_n for $n = 2$, 3, 4, 5, 6, and 7. The top half of the profiles are shown. The Reynolds number is 100, and the angle $\theta = -0.6^{\circ}$.

the centreline, with the conditions $U(0) = 1$, $U'(0) = 0$, and an initial guess for $U''(0)$. Equation (4.1) then provides $U'''(0) = 0$. We march up to the wall using the Runge-Kutta fourth order method. The obtained solution may not satisfy the wall boundary conditions (4.7). Therefore, we iterate for $U''(0)$ using the Newton-Raphson method until the boundary conditions are met. In figure 4.4 the net flow in each case is from left to right, namely the channel is converging downstream, but in each case we have a significant portion in reverse flow, accompanied in alternate cases by a flow separation at the walls. This is somewhat unexpected for convergent channel flow.

Before we move on to the stability of the type III velocity profiles, it is useful to summarise what may be gleaned from the laminar flow velocity profiles about their stability. The Rayleigh-Fjørtoft theorem [Rayleigh, 1880, Fjφrtoft, 1950] tells us that at infinite Reynolds number, a velocity profile which contains a point of inflexion (where U'' goes through a 0) will be unstable. While there is no corresponding theorem for viscous flows, it is commonly expected, and most often found, that flows with inflexional velocity profiles are far more unstable than those without a point of inflexion. Often a low Reynolds number instability is seen with inflexional profiles. So profiles of Type III_2 and higher n are expected to be much more unstable than a profile of type III_1. The question we ask below is, can the inflexional profiles be stabilized at any Reynolds number. If this would be the case, we would have more than one stable laminar solution possible for the same conditions.

Another aspect we may anticipate is the importance of the critical layer. By the Rayleigh-Fjørtoft theorem, type III_1 profiles must be always stable. But we know that viscosity can introduce an instability in this case. The Orr-Sommerfeld equations present a singular perturbation problem at high Reynolds numbers, where viscous effects become important in two (or more) layers within the channel: the critical layer (there could be more than one, as we shall see) and the wall layer. The critical layer is a layer of thickness $\epsilon \sim (\alpha R)^{-1/3}$ centered around the critical point y_c where the mean flow velocity equals the phase speed of the dominant disturbance, i.e., $U(y_c) = c$. This layer is where most of the

disturbance kinetic energy is produced. In other words, the critical layer is instrumental for generating viscosity-driven instability, which is the only way the channel flow can go unstable for a type III_1 profile. The wall layer is of thickness $\epsilon_w \sim (\alpha R)^{-1/2}$, and as the name implies, lies next to the wall. Viscous effects are important here too, in the form of dissipation. Thus perturbation energy is produced in the critical layer, gets transported to the wall layer and gets dissipated there. If the net production is larger than the net dissipation, the perturbation grows, i.e., the flow is unstable. We shall see below that the critical layer is key to the high sensitivity of the stability to the tile angle of the walls. In section 4.3.2, we study the stability of such solutions. We follow this with a detailed discussion on the stability of type III_1 in section 4.3.3.

4.3.2 Stability of type III_2 and III_3 mean profiles

The parabolic velocity profile of laminar plane channel flow is known to be unique. On the other hand, we have seen that a slight change in wall angle compared to the plane channel results in an infinite number of laminar flow profiles which satisfy the JH equations and their boundary conditions. For the slightly convergent flow, we study the stability behaviour of the three laminar velocity profiles denoted as III_1, III_2, and III_3. This section focuses on III_2 and III_3. To our knowledge, the stability boundaries for these two have not been obtained before, and that of the first profile obtained by Fraenkel and Squire [1962] by an approximate method.

We numerically solve the Orr-Sommerfeld equation (4.5) with boundary conditions (4.7) for the given mean profile. The flow is deemed linearly stable at a specific Reynolds number if the imaginary part of the eigenvalue ω from the OS equation (4.5) is negative for all wave numbers α. The critical Reynolds number is defined as the value below which the flow remains stable, and above which the flow becomes unstable for at least one wave number α.

In the stability boundary of the III_2 profile shown in figure 4.5 , the color represents the growth rate, or the imaginary part of ω. The black contour represents the neutral curve where the growth rate is zero, signifying that perturbations will neither grow nor decay along this curve. Perturbations inside this neutral curve will experience positive growth rates, indicating exponential growth. Outside the curve, growth rates are negative, indicating decay of perturbations. For this flow $R_{crit} = 40$. At the unstable condition of $R = 100$ and $\alpha = 2.0$, Fig. (4.6) displays the mean flow and energy budget, while Fig. (4.7) illustrates the eigenfunction $\hat{\psi}$. The mean profile $U(y)$ in Fig. (4.6a) and the phase speed of the dominant perturbation $c_r = -0.75$, yielding two solutions for $U(y_c) = c_r$ in the half channel, i.e., pointing to the existence of two critical layers in each half of the channel, at $y_{c_1} = \pm 0.93$ and $y_{c_2} = \pm 0.65$. Note that the phase propagates upstream in this case. The production of perturbation energy W_+ occurs only in one of the critical

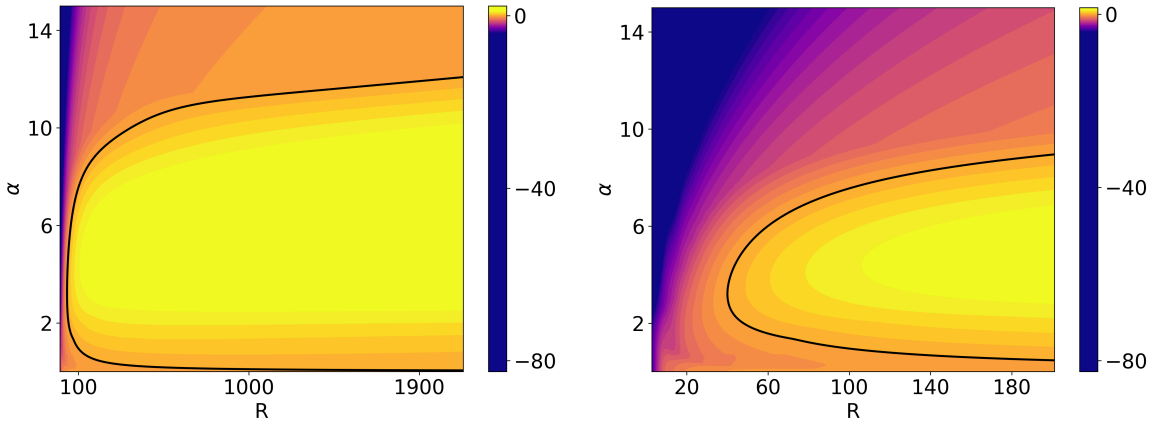

(a) (b)

Figure 4.5: (a) Growth rate of instability (shown in colour) for velocity profiles of type III_2 for perturbation wave number α and Reynolds number R. The black line denotes the neutral curve. The wall convergence angle θ is -0.6^o. (b) Zoomed-in view of the low Reynolds number region in (a) highlighting the stable behaviour at low Reynolds numbers.

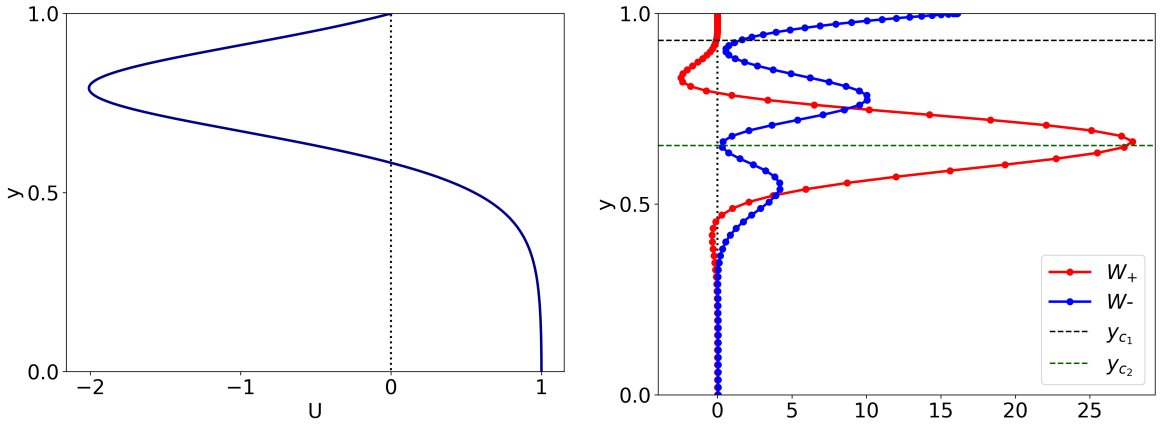

(a) (b)

Figure 4.6: (a) The steady laminar velocity profile III_2 and (b) the energy budget for a typical unstable condition $R = 100$, $\alpha = 2$ in Figure (4.5). Production is shown in red, and dissipation in blue. The two critical layer locations lying in this half of the channel are shown by the dashed lines.

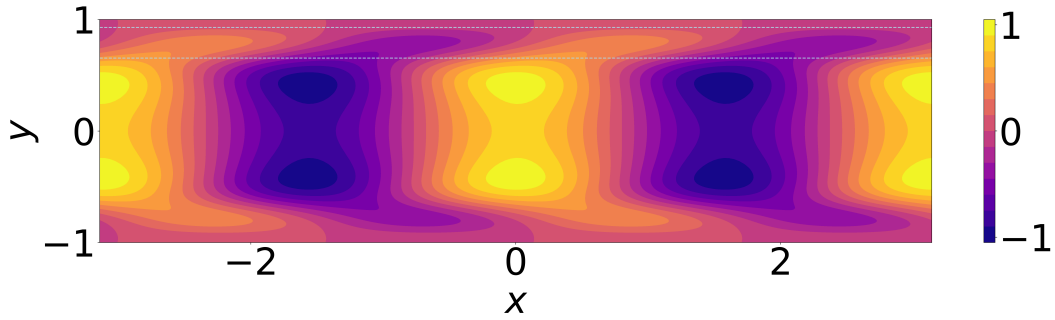

Figure 4.7: Perturbation streamfunction $\hat{\psi}$ for a typical unstable point at $R = 100$ and $\alpha = 2$ corresponding to the type III_2 mean profile. Critical layer locations in the upper half of the channel are indicated by thin dashed lines.

layers, centered around y_{c_2}. A plausible reason for this is that the critical layer thickness ϵ being $\sim (\alpha R)^{-1/3} \sim 0.17$, and the wall layer thickness $\epsilon_w = (\alpha R)^{-1/2} \sim 0.07$, the critical layer centered around $y_{c_1} = 0.93$ overlaps with the wall layer, where dissipation is expected to be high. There is significant dissipation taking place away from the wall, and this is anomalous.

In Figure (4.8) , the stability of III_3 is demonstrated, with the neutral curve represented

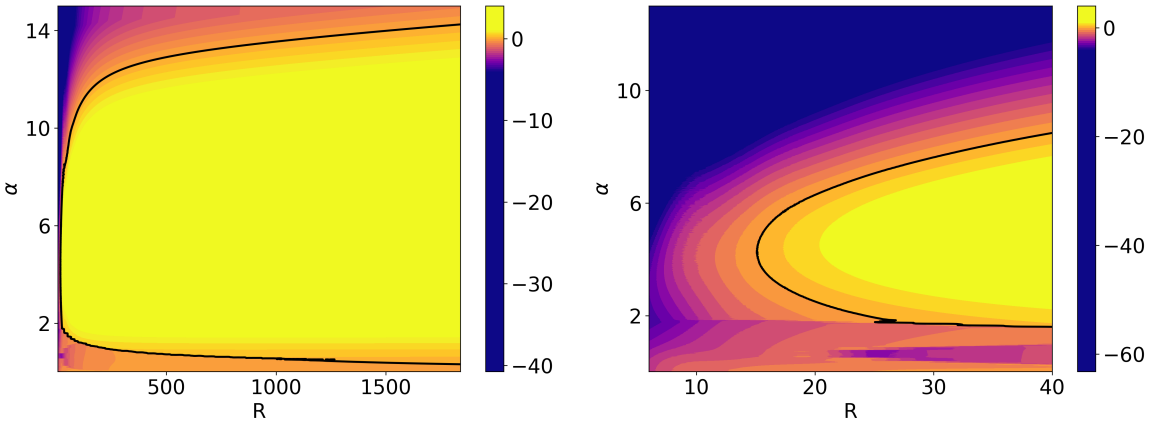

(a) (b)

Figure 4.8: (a) Growth rate of instability (shown in colour) for velocity profiles of type III_3 for perturbation wave number α and Reynolds number R. The black line denotes the neutral curve. The wall convergence angle θ is -0.6^o. (b) Zoomed-in view of the low Reynolds number region in (a) highlighting the stable behaviour at low Reynolds numbers.

by a black line. This velocity profile is different from the one above in that there is no flow separation at the wall, and instead there is a significant region of reverse flow somewhere in the channel. The critical Reynolds number is $R_{\mathrm{crit}} = 15$. At Reynolds number $R = 100$ and the wavenumber $\alpha = 2.0$, the mean flow and the energy budget are depicted in Fig. (4.9) , and the eigenfunction $\hat{\psi}$ is illustrated in Fig. (4.10) . The phase speed of the dominant eigenmode is $c_r = 0.48$, and there are now three critical layers in the half channel,

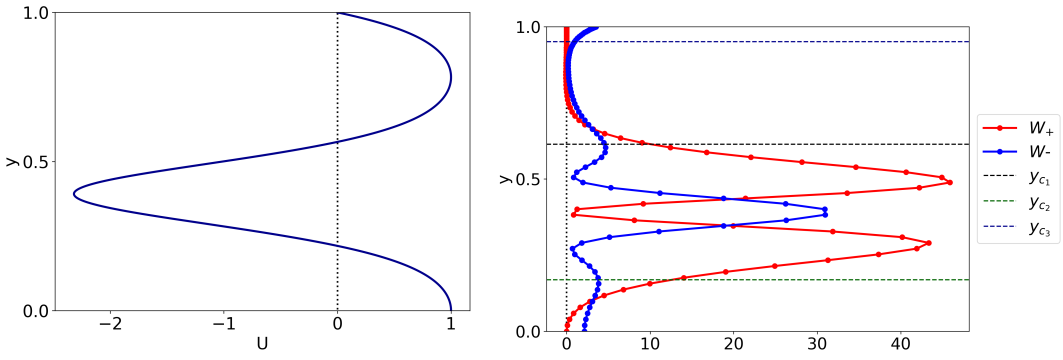

(a) (b)

Figure 4.9: (a) The steady laminar velocity profile III_3 and (b) the energy budget for a typical unstable condition $R = 100$, $\alpha = 2$ in Figure (4.8). Production is shown in red, and dissipation in blue. The three critical layer locations lying in this half of the channel are shown by the dashed lines.

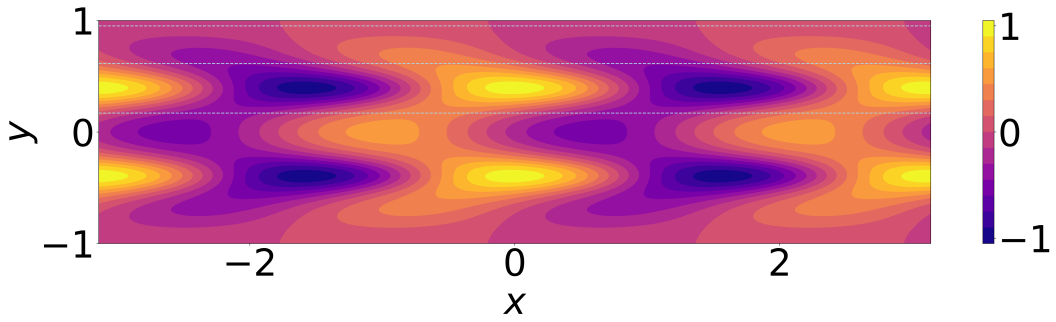

Figure 4.10: Perturbation streamfunction $\hat{\psi}$ for a typical unstable point $R = 100$ and $\alpha = 2$ corresponding to the type III_3 mean profile. The three critical layer locations lying in the top half of the channel are shown by the thin dashed lines.

located at $y_{c_1} = 0.95$, $y_{c_2} = 0.61$, and $y_{c_3} = 0.17$. The thickness of the critical layers and the wall layer depend only on the Reynolds number and wavenumber, which therefore remain the same as for $\mathbf{III_2}$. In this case the maxima in kinetic energy production W_+ do not coincide with the critical layer locations, and this is most unusual in shear flow. The reason is that viscous effects are not absent anywhere due to the existence of multiple critical layers. Equally interesting, the dissipation W_- is not maximum at the walls but peaks around $y \sim 0.4$. This too is most unusual. The critical layer at $y_{c_1} = 0.95$ overlaps with the wall layer, probably resulting in minimal kinetic energy production as well as small dissipation near the wall. The eigenfunction structure in Figs. (4.10) and (4.7) are qualitatively different from those of the one-lobed profile (not shown).

The main finding in this section is that there are multiple stable solutions at low Reynolds number which are stable. While to our knowledge this has not been established before for JH flow, multiple stable laminar flow solutions, all asymmetric about the channel centreline, have been obtained in a related flow by Sobey and Drazin [1986]. So we may ask whether a variety of laminar flows can be obtained in experiment for the same JH geometry and same Reynolds number. If they are, that could have interesting implications for small-scale flows, where JH flows are of interest, see e.g. Rezaee [2024].

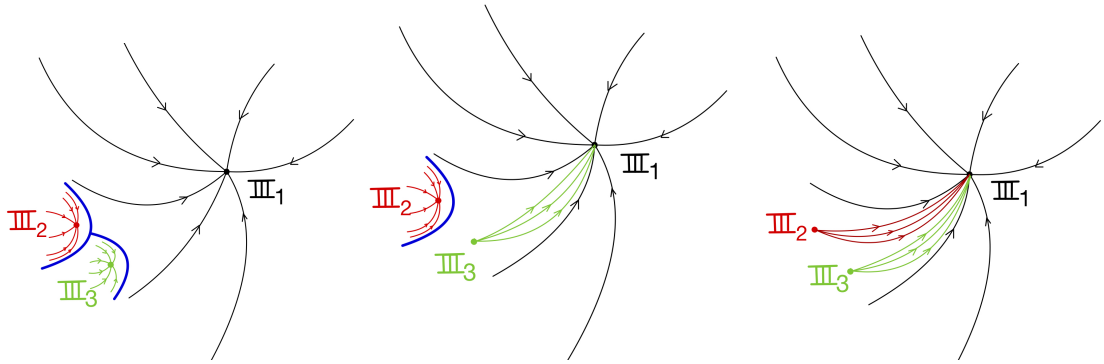

(a) R=10 (b) R=20 (c) R=60

Figure 4.11: Schematic of a portion of the phase space of laminar solutions at low Reynolds number in a convergent channel. Three steady (attractive) laminar states, labeled as III_1, III_2, and III_3, are depicted as black, red, and green points, respectively. Sample trajectories leading to, or emanating from, each, are shown in the same colour, and basin boundaries are indicated by the blue curves. In (a), for a Reynolds number $R = 10$, all three laminar states are stable. In (b), with $R = 20$, III_1 and III_2 remain stable. In (c), for $R = 60$, only the III_1 laminar state remains stable. The wall angle is set to $\theta = -0.6^o$.

Since multiple velocity profiles are stable at low Reynolds number, they can all, in principle, be observed experimentally. The ease of experimentally obtaining a given profile, will however, depend on the size of its basin of attraction in phase space and the ability to access that basin. A schematic depiction in figure 4.11 shows a portion of the phase space, containing three possible laminar velocity profiles at low Reynolds number. The complete

phase space is much larger, and contains a multitude of other solutions. The phase space is depicted in two dimensions, whereas it is in fact infinite dimensional, since U is continuous function of y. The solutions III_1, III_2 and III_3, being steady solutions, are fixed points in this phase space. At low Reynolds numbers, we know that solution III_1 remains stable. At $Re = 10$, we can glean from figures (4.5,4.8) that each is an attractive (stable) fixed point. The simultaneous existence of multiple attractors means that each has its corresponding basin of attraction, so profiles near each one, when generated experimentally, will fall into them. At $Re = 20$, we see from figures (4.8) that III_3 is now unstable, and so its basin of attraction has vanished. Trajectories now emerge out of this fixed point and will approach one of the stable fixed points. At $Re = 60$, we know from figures (4.5) that III_2 has gone unstable as well, leaving behind III_1 as the only attractor. The basin boundaries are shown schematically here but future computations are needed determine the size of each basin of attraction. The fact that the pressure gradients for a given flow rate are different for the different profiles could provide a clue to experimenters on how to design for them.

4.3.3 Stability of type III_1 or one-lobed laminar velocity profiles

The parabolic velocity profile of laminar plane channel flow is linearly stable when the Reynolds number is below the critical value of $R_{SC} = 5772.2$. But even a minute departure of the tilt and θ of the wall away from 0 results in a significant change in the critical Reynolds number R_{crit}. In this section, we use R_{SC}, but refer to it simply as R. The variation of the critical Reynolds number with tilt angle is depicted in Figure (4.12). This figure is also available in Jotkar and Govindarajan [2017] and was produced by a closely related numerical code. In the convergent channel, the critical Reynolds number increases

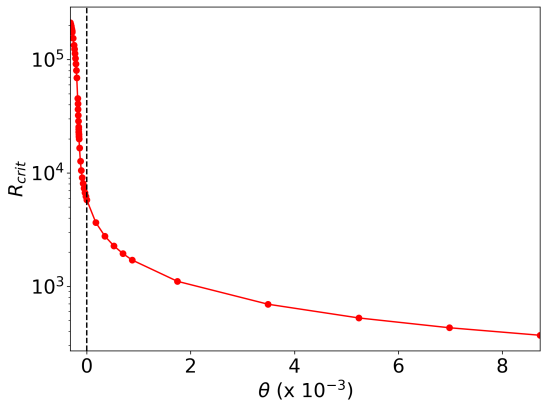

Figure 4.12: Sensitivity of critical Reynolds number to wall angle (θ in radians) . Negative angles indicate convergent channels, positive angles indicate divergent channels, with the straight channel represented by the vertical dotted black line at $\theta = 0$. This curve can also be found in Jotkar and Govindarajan [2017].

extremely rapidly with ($|\theta|$). We wished to investigate whether the flow becomes stable

at any Reynolds number beyond a certain convergence angle. We could however not draw a definitive conclusion on this question due to the sharp loss in numerical accuracy beyond the angles shown. The physical reasons for this will become clear in the following section. As illustrated in figure 4.13a, with increase in $|\theta|$ the critical layer progressively

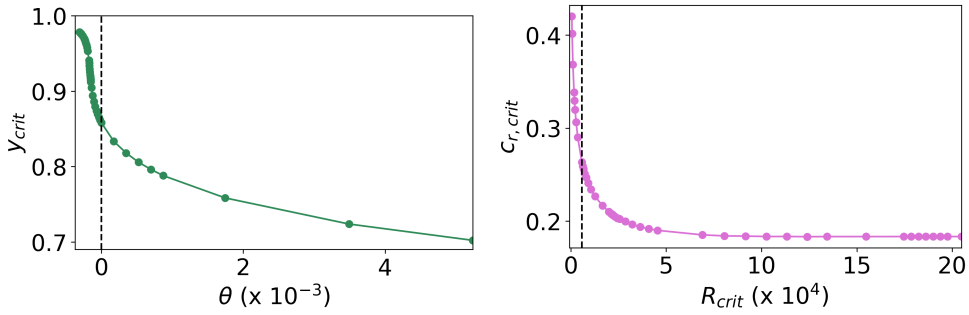

(a) (b)

Figure 4.13: (a) Variation of the critical layer location, y_{crit}, with wall angle. (b) Variation of phase speed $c_{r,\mathrm{crit}}$ of the dominant perturbation at the critical point $(R_{\mathrm{crit}}, \alpha_{\mathrm{crit}})$ with the critical Reynolds number. The vertical dotted line in (a) represents $\theta = 0$, and $R_{crit} = 5772$ in (b) corresponds to the straight channel.

approaches the wall and becomes increasingly narrow due to the large magnitude of R_{crit}. The phase speed of the dominant perturbation at the critical point, $(R_{crit}, \alpha_{crit})$, decreases and eventually flattens out at $c_{r,crit} = 0.183$, as shown in figure 4.13b. Incidentally this plateauing of the phase speed agrees with the turning-point approximation calculation of Fujimura [1982]. In figure(4.14), the typical eigenfunctions at the critical point $(R_{crit}, \alpha_{crit})$ of the convergent channel for $\theta = -0.01^{\circ}$ are contrasted with the eigenfunctions of a straight channel and a divergent channel. The contour of the convergent eigenfunction or stream function appears more rectangular and distinct when compared to those of the straight channel and the divergent channel. In figure (4.15) the neutral curve of a convergent channel of $\theta = -0.01^{\circ}$ is compared with the straight channel. The dramatic difference of one hundredth of a degree wall tile is evident here. Higher wavenumber modes are unstable in the convergent channel than in the straight channel. In figure (4.16) we compare the energy budget at $R = 5772$, $\alpha = 1.02$ (which represents the critical point of the straight channel) of the convergent channel for $\theta = -0.018^{\circ}$ with the straight and the divergent channel. The net production in the straight channel (the integral of the curve across the channel width) is equal to the net dissipation. In the convergent channel, there is significant negative production, resulting in lower net production than dissipation, while the production is positive and extends across the channel in the divergent case. Again, the large differences due to small changes in tilt angle are highlighted. The net production and dissipation are shown in Fig. (4.17) as functions of the tilt angle. Variations in the dissipation are small but those in the production are large, highlighting the importance of the critical or production layer. The difference of the integral increases

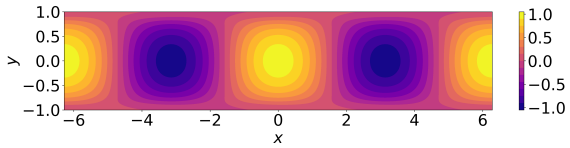

(a) Straight channel: $R = 5772$, $\alpha = 1.02$

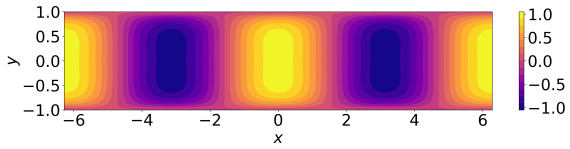

(b) Convergent channel: $R = 45506$, $\alpha = 1.06$

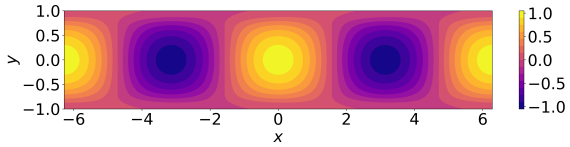

(c) Divergent channel: $R = 2271$, $\alpha = 1.13$

Figure 4.14: Comparison of the eigenfunctions $\hat{\psi}$ of straight, converging, and diverging channels at the critical Reynolds number and critical perturbation wave number given in the caption of the subplots (a),(b),and (c).

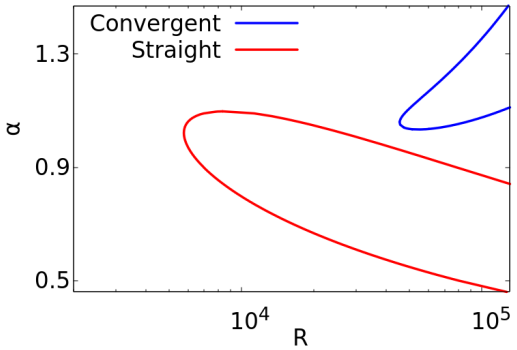

Figure 4.15: Neutral curves compared between a convergent channel with a wall angle of $\theta = -0.01^{\circ}$ (shown in blue, and partially available in Jotkar and Govindarajan [2017]) and a straight channel (shown in red).

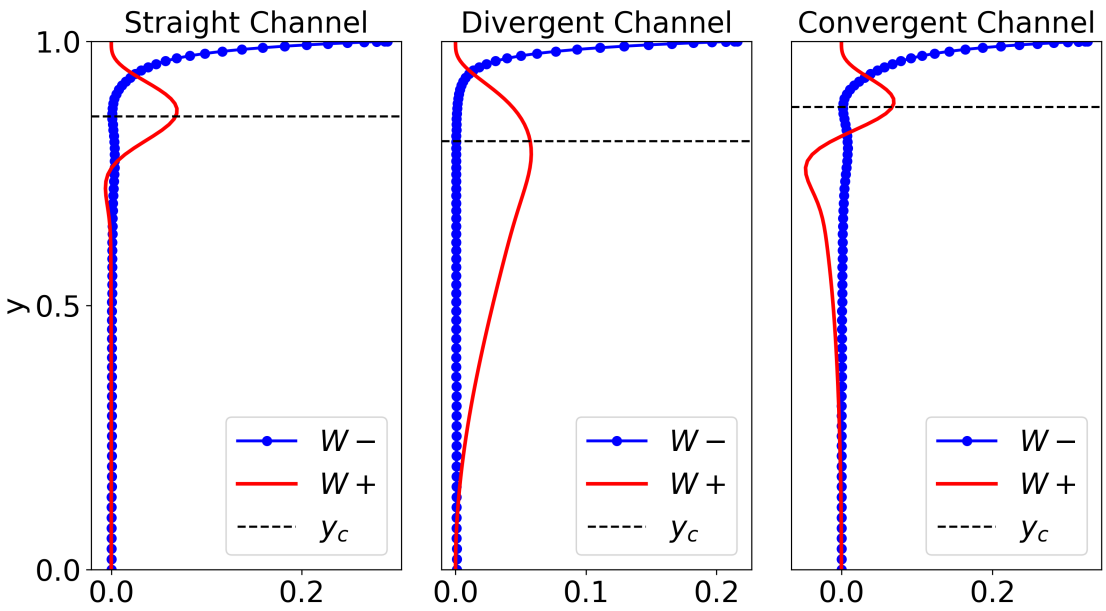

Figure 4.16: Budget of perturbation kinetic energy budget for $R = 5772$ and $\alpha = 1.02$. The angles $\theta = 0^o$, $\theta = 0.03^o$, and $\theta = -0.018^o$ correspond to a straight channel, a divergent channel and a convergent channel, respectively. Note the major changes in kinetic energy production resulting from a mere change of a few percent of a degree in wall angle.

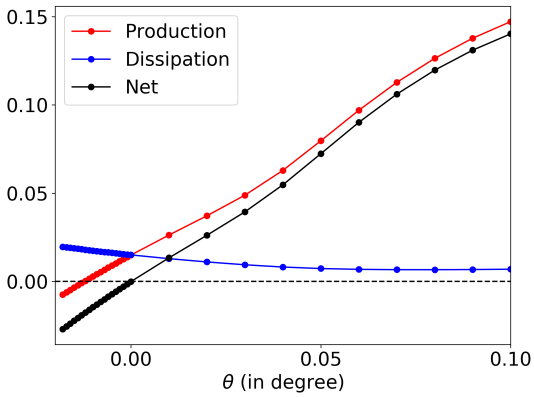

Figure 4.17: Variation of production and dissipation with wall angle θ at $R = 5772$ and $\alpha = 1.02$. Red curve: integral across the channel of the production W_+, Blue curve: integral of the dissipation W_-, Black curve: net energy (integral of $W_+ - W_-$).

with the convergence angle, leading to significant stabilization in the convergent channel.

4.3.4 Asymptotic analysis of the perturbation equation

In this section, we develop a framework that explains the mechanism behind the extremely high sensitivity of the angle in convergent channel flow. After reviewing the current understanding of parallel shear flow, we derive the dominant balances for convergent channel flow. We have seen that for many-lobed mean flows there can be more than one critical layer in each half of the channel, but we concentrate our discussion on the one-lobed profile III_1, since it is likely to be the easiest to achieve in experiment, it is stable up to a higher Reynolds than the others, and it is closest to the flow through a straight channel, and therefore remarkable in its highly modified behaviour at small $|\theta|$.

In the Orr-Sommerfeld equation (4.5), the highest derivative term in y, which is the fourth-order derivative, is scaled by the inverse of the Reynolds number. As the Reynolds number approaches infinity, this term cannot be neglected because doing so would prevent us from satisfying all four boundary conditions associated with the equation (4.7). This scenario exemplifies a classical singular perturbation problem, where the highest derivative term becomes comparable in magnitude to the terms on the left-hand side in certain regions of the flow. As mentioned above, there are two layers where viscous effects are significant and gradients are steep: the wall layer, with a thickness of $\epsilon_w \sim R^{-1/2}$, and the critical layer, with a thickness of $\epsilon \sim R^{-1/3}$. The critical-layer [Lin, 1945a,b, 1946] is a thin region centered around the critical point y_c in the channel, where the mean flow velocity matches the phase speed of the dominant normal-mode perturbation, i.e., $U(y_c) = c$. Our primary interest lies in the critical layer, which explains the mechanism of huge stabilization in the convergent channel.

We follow the standard procedure to derive the critical layer equations, as done by Lin Lin [1945a,b, 1946]. For details on singular perturbation methods, see Van Dyke [1964]. We define an inner variable ξ as

$$\xi = \frac{y - y_c}{\epsilon} \tag{4.13}$$

and will select ϵ to ensure that the derivatives of the stream function in ξ are $O(1)$. To derive the dominant balances, we write the relevant variables in the form of series expansions within the critical layer as

$$\psi = \sum_{n=0}^{\infty} \epsilon^n \psi_n(\xi) \tag{4.14}$$

In this layer, the mean flow may be written in the following expansion:

$$U(y) - c = (y - y_c)U_c' + \frac{(y - y_c)^2}{2} U_c'' + \cdots . \tag{4.15}$$

We substitute the expansions (2.33,2.36) in equation (4.5). We apriori retain all terms that may participate in the dominant balance and obtain the following composite lowest-order equation:

$$\left[-\frac{iU_c'\xi}{\epsilon}D_\xi^2 - U_c'' - \frac{1}{i\alpha R\epsilon^4}D_\xi^4\right]\psi_0 = 0. \tag{4.16}$$

Here, the subscript c represents the value of the function at the critical point y_c. In the traditional critical layer balance of Lin, since $\epsilon \ll 1$, the second term would be $O(1)$, and therefore drop out, and we would obtain a balance between the first and the third terms which are much bigger, with $\epsilon \sim (\alpha R)^{-1/3}$. This changes with even a small convergence. We now need an estimate of how high U_c'' is compared to the other terms. From figure (4.18), we see that as S_0 becomes high, we have U_w'' and therefore $U_c'' \sim S_0$. Consequently,

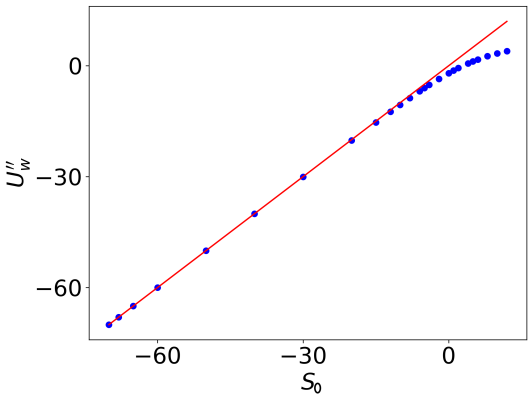

Figure 4.18: Blue dots show the second derivative of the mean velocity at the wall U_w'' as a function of S_0, approaching the red line defined by $U_w'' = S_0$ at large negative S_0.

the contribution of the second term to the lowest-order equation (2.46) is higher at higher S_0. The first term will ultimately drop out, giving

$$-S_0\psi_0 = \frac{1}{i\alpha R\epsilon^4}D_\xi^4\psi_0 \tag{4.17}$$

at high S_0. We choose $\epsilon = (-\alpha R^2|\theta|)^{-1/4}$, so the above equation becomes

$$\psi_0 = -iD_\xi^4\psi_0. \tag{4.18}$$

Equation (4.18) happens to be directly solvable, with a general solution given by

$$\psi_0(\xi) = A_1\psi^{(1)} + A_2\psi^{(2)} + A_3\psi^{(3)} + A_4\psi^{(4)}, \tag{4.19}$$

where $\psi^{(j)} = e^{\lambda_j\xi}$, $\lambda_j = e^{i\pi(4j-5)/8}$, $j = 1,\ 2,\ 3,\ 4$, and $A_1,\ A_2,\ A_3$, and A_4 are constants that can be obtained by matching the inner solution with the outer solution. While the analytical solution in the outer region is difficult to obtain, we have the complete numerical solution which we use in the outer regime to fix the four constants, A_j. In figure

(4.19) the critical layer (inner layer) solution of equation (4.18), with boundary conditions

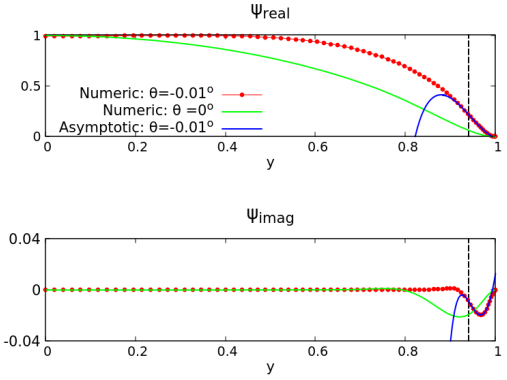

Figure 4.19: Comparison of the critical layer (blue) and full numerical (red) solutions for the convergent channel with $\theta = -0.01°$ at the critical point (R=45506, $\alpha = 1.06$). The solution for the straight channel at its critical point (R=5772, $\alpha = 1.02$) is shown in green for comparison. The top and bottom subplots show the real and imaginary parts of the streamfunction amplitude respectively. The dashed line indicates the location of a critical layer in this half of the channel.

derived from numerical data at two points is shown along with the complete solution. In the inner layer, the analytical solution aligns well with the numerical solution of the full system. This provides some evidence that the critical layer balance contains the physics we seek. The primary finding is that the critical layer thickness scales differently from the traditional case, and that the second derivative of the mean velocity profile is dominant in balancing the highest viscous derivative. Thus a tiny change in geometry alters the stability behaviour.

The critical layer analysis we carried out made the quasi-parallel approximation. Govindarajan and Narasimha [1997] showed how the mean flow perpendicular to the centreline can alter the critical-layer balance. This could become significant at higher convergence angles.

4.3.5 Comparison with pipe flow

It is worth drawing an analogy between channel and pipe flow stability, and this is done in figure 4.20 . While plane channel flow becomes linearly unstable beyond a finite Reynolds number and pipe flow does not, we note that pipe flow goes unstable at a finite Reynolds number for any non-zero divergence, and the critical Reynolds number goes down with divergence angle as $R_{crit} = 10/\theta$ (Sahu and Govindarajan [2005]). In other words, the critical Reynolds number in a pipe diverges as $1/\theta$. While we were not able to establish such a clear mathematical relationship in converging channel flow, nor indeed are we able to say definitively whether the critical Reynolds number diverges at a finite convergence angle, that remains a question for mere pedantry, given the orders of magnitude increase

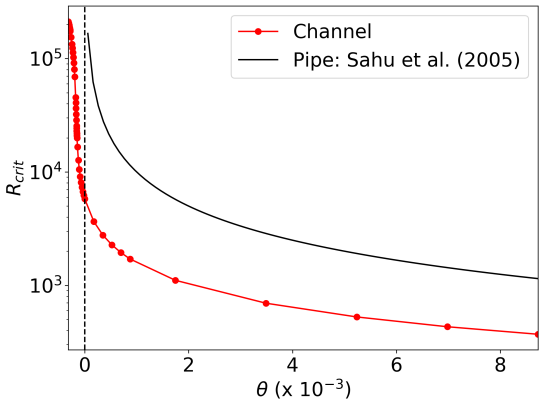

Figure 4.20: Comparison of the critical Reynolds number sensitivity to wall angle (θ in radians) for the channel (red curve) and pipe (black curve) Sahu and Govindarajan [2005].

in the critical Reynolds number for a convergence angle of a merest fraction of a degree. We note that due to Squire's theorem, the critical Reynolds number is determined in the channel by two-dimensional perturbations, while in pipe flow this theorem does not apply. There the most unstable mode, whose behaviour is shown is of $m = 1$, i.e., it is the one which supports one wave in the azimuthal direction.

4.4 Discussion

Our basic aim has been to underline the myriad ways in which an extremely small angle of wall convergence can drastically and fundamentally change the flow through a two-dimensional channel. This study reveals that at small Reynolds numbers, of $O(10)$, we can have multiple stable laminar flow solutions through convergent channels. While the multiplicity of solutions was known since the time of Fraenkel, the stability at low Reynolds for these very profiles had not been established, to our knowledge. We note that while the multiple solutions have the same Reynolds number, they must have different pressure gradients, and this will help experimenters attempting to obtain those flows.

As for the one-lobed profile of type III_1, we have obtained the lowest-order equation in the critical layer, following the traditional approach. We have shown how the dominant (lowest-order) balance in the critical layer is altered fundamentally by convergence, with the second derivative of the velocity profile entering the balance at even very low angles of convergence and ousting out the inviscid term which normally balances the dominant viscous effect.

We have discussed the direct analogy with pipe flow. Although convergent channel flow and divergent pipe flow are physically and mathematically distinct systems, they exhibit similar behavior in terms of linear stability, particularly in the sensitivity of the critical Reynolds number to the wall tilt angle.

In shear flows of this kind, we know that the transition to turbulence is subcritical, there have already been a lot of studies almost a decade ago precisely demonstrating this. The subcritical transition in pipe flow is highly sensitive to the wall divergence angle, as shown by Shenoy et al. [2020] in their direct numerical simulation and by Lebon et al. [2018] in their experiment on sudden wall expansion. We emphasise that we have only conducted a modal analysis here, considering two-dimensional perturbations. The purpose has been to elucidate some physics, and not to obtain quantitative anticipated growth. A transient growth study including three dimensional perturbations was carried out by Jotkar and Govindarajan [2017, 2019]. It indicated low levels of transient growth compared to a straight channel. Further work is needed to address the question of even the starting seeds of transition to turbulence. The recent work of Kant et al. [2022] indicates that convergent channels are even more sensitive in this regard than divergent ones. And the level of non-normality in a plane channel may be directly related to the sensitivity of the modal critical Reynolds number to tilt angle, as done in a related study by Jose and Govindarajan [2020] rotating plane channel flow. In other words, the sensitivity to tilt angle may have its underpinnings in the non-normal nature of the stability operator for a plane channel, and further study along these lines will provide a more complete answer.

We earlier studied non-modal perturbation growth in the one-lobed mean profile in Jotkar and Govindarajan [2017] where we saw that a convergence of half a degree was sufficient to reduce the optimal growth at high Reynolds number by an order of magnitude. This suggests that while subcritical transition to turbulence may occur in the convergent channel, there may be significant differences due to even a small angle of convergence, including in raising the Reynolds number at which turbulence can be attained. There is a need for studying these flows, including the exponential and algebraic growth of disturbances that take place, the origin of nonlinearity, and the entire process of transition to turbulence, in direct numerical simulations. The sensitive to small convergences and divergences points to the possible role of wall roughness in influencing the transition to turbulence through modified linear perturbation growth, which would form another possibly fruitful direction of future study.

We hope the revelations of the present study on the multiple laminar flow solutions as well as on the role of the critical layer in the one-lobed solution will make this an attractive topic for future studies.

Summary

Shear flows exhibit complex stability characteristics, making them both important and difficult to predict. In this study, we investigate the impact of non-uniform particle loading on Poiseuille flow. We derive a stability characteristic equation for the two-way coupled particulate flow system, incorporating Stokes drag and viscosity stratification induced by dilute particles as interaction mechanisms. Additionally, we extend Squire's theorem to account for systems with non-uniform particle distributions and viscosity stratification. This extension allows us to analyze a two-dimensional system without altering the overall conclusions regarding exponential growth. The governing equations are solved numerically using a pseudo-spectral method.

Our numerical results reveal that the stability response of the flow to non-uniform particle loading falls into two distinct categories: overlap and non-overlap conditions. In non-overlap conditions, the particle-laden layer remains separated from the critical layer, exerting minimal influence on stability and primarily stabilizing the flow. This stabilization occurs because particle-induced drag, arising from velocity differences between the particles and the fluid, enhances perturbation energy dissipation. In contrast, in overlap conditions, the interaction significantly modifies stability, predominantly destabilizing the flow. This destabilization comes from a singularity introduced by a sharp change in particle mass fraction, which alters the energy production mechanism in the critical layer, typically enhancing perturbation energy production.

Furthermore, two new instability modes emerge alongside the Tollmien-Schlichting (TS) mode: a shortwave mode (S-mode) at low Reynolds numbers and a longwave mode (L-mode) persisting across a broad range of Reynolds numbers. These three instability modes exhibit distinct regimes of existence and undergo intriguing interactions, including intersections and mergers, as system parameters vary.

The mechanisms of these instabilities are rooted in critical-layer physics. We derive the lowest-order critical and wall layer equations for particulate shear flow with dilute loading, highlighting the presence of additional particle terms alongside viscosity, distinguishing them from classical clean-flow equations where viscosity, however small, governs stability. Since the viscosity term appears in clean flow, the instability is referred to as viscous instability. With dilute particle loading, additional particle terms emerge, leading to what

we can term particle-viscosity instability.

The lowest-order critical layer equation, combined with an energy-budget analysis, reveals the consequences for stability. The distinction between overlap and non-overlap conditions originates in the critical layer, where variations in base particle concentration significantly influence the production of disturbance kinetic energy, resulting in strong destabilization over a range of conditions. Although the wall layer equation includes particle terms, it does not play a significant role in the energy budget.

In the above analysis, gravity was neglected. Now, taking it into account, considering a horizontal channel with slowly settling particles, we analyze the stability of quasi-steady particle distributions under small perturbations. While particles eventually settle at the wall, each stage of their distribution stabilizes the flow. However, when finite particle to fluid density ratios are considered, the particle concentration causes viscosity variations that lead to significant destabilization, in contrast to the no-gravity case, where viscosity stabilizes the flow. Our analysis shows that instability arises due to the mean velocity profile modifications caused by the viscosity variation.

In the previous analysis, we assumed perfectly straight and parallel channel walls. However, in experiments, achieving perfectly aligned walls is challenging. Now, we consider slightly tilted walls for a clean flow, representing the classical Jeffery-Hamel system. It is well known that this system exhibits multiple solutions for a given Reynolds number. Even an extremely small wall convergence angle can significantly alter the flow behavior in a two-dimensional channel. Our study reveals that in convergent channels at Reynolds numbers below 10, at least three stable laminar flow solutions can exist. These multiple stable solutions for the same Reynolds number could potentially be observed in experiments, as they must correspond to different pressure gradients. For multi-lobed velocity profiles of type III_2 and III_3 , multiple critical layers can exist, and dissipation does not necessarily reach its maximum at the wall. This is particularly interesting because viscosity plays a crucial role in only two regions: the critical layer, where production occurs, and the wall layer, where dissipation takes place.

In the one-lobed velocity profile of type III_1, the critical Reynolds number is extremely sensitive to the wall tilt angle. We have shown that this sensitivity arises because the dominant balance in the critical layer differs from the conventional balance found in a plane channel.

Bibliography

P. Anand and G. Subramanian. Inertial migration in pressure-driven channel flow: beyond the segre-silberberg pinch. arXiv preprint arXiv:2301.00789, 2023.

Evgeny S. Asmolov. The inertial lift on a spherical particle in a plane poiseuille flow at large channel reynolds number. Journal of fluid mechanics, 381:63–87, 1999.

Pinaki Bhattacharya, MP Manoharan, Rama Govindarajan, and Roddam Narasimha. The critical reynolds number of a laminar incompressible mixing layer from minimal composite theory. Journal of Fluid Mechanics, 565:105–114, 2006.

SA Boronin. Hydrodynamic stability of stratified suspension flow in a plane channel. In Doklady Physics, volume 54, pages 536–539. SP MAIK Nauka/Interperiodica Dordrecht, 2009.

SA Boronin and AN Osiptsov. Stability of a disperse-mixture flow in a boundary layer. Fluid Dynamics, 43(1):66–76, 2008.

RG Cox and HJCES Brenner. The lateral migration of solid particles in poiseuille flow—i theory. Chemical Engineering Science, 23(2):147–173, 1968.

RG Cox and SG Mason. Suspended particles in fluid flow through tubes. Annual Review of Fluid Mechanics, 3(1):291–316, 1971.

Philip G Drazin. Introduction to hydrodynamic stability, volume 32. Cambridge university press, 2002.

Philip G Drazin and William Hill Reid. Hydrodynamic stability. Cambridge university press, 2004.

PM Eagles. The stability of a family of jeffery-hamel solutions for divergent channel flow. Journal of Fluid Mechanics, 24(1):191–207, 1966.

R Fjφrtoft. Application of integral theorems in deriving criteria of stability for laminar flows and for the baroclinic circular vortex. Geofys. Publ., 17(6):1–52, 1950.

Ludwig Edward Fraenkel and Herbert Brian Squire. Laminar flow in symmetrical channels with slightly curved walls, i. on the jeffery-hamel solutions for flow between plane walls. Proceedings of the Royal Society of London. Series A. Mathematical and Physical Sciences, 267(1328):119–138, 1962.

Kaoru Fujimura. On the linear stability of jeffery-hamel flow in a convergent channel. Journal of the Physical Society of Japan, 51(6):2000–2009, 1982.

Georgios Giamagas, Francesco Zonta, Alessio Roccon, and Alfredo Soldati. Turbulence and interface waves in stratified oil–water channel flow at large viscosity ratio. Flow, Turbulence and Combustion, 112(1):15–31, 2024.

R. Govindarajan. Effect of miscibility on the linear instability of two-fluid channel flow. International Journal of Multiphase Flow, 30(10):1177–1192, 2004.

Rama Govindarajan and R Narasimha. A low-order theory for stability of non-parallel boundary layer flows. Proceedings of the Royal Society of London. Series A: Mathematical, Physical and Engineering Sciences, 453(1967):2537–2549, 1997.

Rama Govindarajan and R Narasimha. Estimating amplitude ratios in boundary layer stability theory: a comparison between two approaches. Journal of Fluid Mechanics, 439:403–412, 2001.

Georg Hamel. Spiralformige bewegungen zaher flussigkeiten. 1917.

BP Ho and LG0284 Leal. Inertial migration of rigid spheres in two-dimensional unidirectional flows. Journal of fluid mechanics, 65(2):365–400, 1974.

Xiaoyi Hu and Thomas Cubaud. Viscous wave breaking and ligament formation in microfluidic systems. Physical Review Letters, 121(4):044502, 2018.

EB Isakov and V Ya Rudnyak. Stability of rarefied dusty gas and suspension flows in a plane channel. Fluid Dynamics, 30(5):708–712, 1995.

G Ba Jeffery. L. the two-dimensional steady motion of a viscous fluid. The London, Edinburgh, and Dublin philosophical magazine and journal of science, 29(172):455–465, 1915.

Sharath Jose and Rama Govindarajan. Non-normal origin of modal instabilities in rotating plane shear flows. Proceedings of the Royal Society A, 476(2233):20190550, 2020.

Mamta Jotkar and Rama Govindarajan. Two-dimensional modal and non-modal instabilities in straight-diverging-straight channel flow. Physics of Fluids, 31(1), 2019.

Mamta R Jotkar and Rama Govindarajan. Non-modal stability of jeffery-hamel flow. Physics of Fluids, 29(6), 2017.

Mamta R Jotkar, Gayathri Swaminathan, Kirti Chandra Sahu, and Rama Govindarajan. Global linear instability of flow through a converging–diverging channel. Journal of Fluids Engineering, 138(3):031301, 2016.

Ravi Kant, Vishal Sharma, Ramesh Bhoraniya, and Narayanan Vinod. Receptivity and sensitivity analysis of jeffery-hamel flow. Sādhanā, 47(3):154, 2022.

Joy Klinkenberg, HC De Lange, and Luca Brandt. Modal and non-modal stability of particle-laden channel flow. Physics of fluids, 23(6), 2011.

Joy Klinkenberg, HC De Lange, and Luca Brandt. Linear stability of particle laden flows: the influence of added mass, fluid acceleration and basset history force. Meccanica, 49: 811–827, 2014.

Anup Kumar and Rama Govindarajan. On the intense sensitivity to wall convergence of instability in a channel. Physics of Fluids, 36(10), 2024a.

Anup Kumar and Rama Govindarajan. Mechanism of instability in non-uniform dusty channel flow. Journal of Fluid Mechanics, 997:A77, 2024b.

Iman Lashgari, Francesco Picano, Wim-Paul Breugem, and Luca Brandt. Laminar, turbulent, and inertial shear-thickening regimes in channel flow of neutrally buoyant particle suspensions. Physical review letters, 113(25):254502, 2014.

Benoît Lebon, Jorge Peixinho, Shun Ishizaka, and Yuji Tasaka. Subcritical transition to turbulence in a sudden circular pipe expansion. Journal of Fluid Mechanics, 849: 340–354, 2018.

CC. Lin. On the stability of two-dimensional parallel flows: Part i.—general theory. Quarterly of Applied Mathematics, 3(2):117–142, 1945a.

CC Lin. On the stability of two-dimensional parallel flows. ii. stability in an inviscid fluid. Quarterly of Applied Mathematics, 3(3):218–234, 1945b.

CC. Lin. On the stability of two-dimensional parallel flows. iii. stability in a viscous fluid. Quarterly of Applied Mathematics, 3(4):277–301, 1946.

J.P. Matas, J. F. Morris, and E. Guazzelli. Transition to turbulence in particulate pipe flow. Phys. Rev. Lett., 90:014501, Jan 2003a. doi: 10.1103/PhysRevLett.90.014501. URL https://link.aps.org/doi/10.1103/PhysRevLett.90.014501.

J.P. Matas, J. F. Morris, and E. Guazzelli. Influence of particles on the transition to turbulence in pipe flow. Philosophical Transactions of the Royal Society A, 361:911–919, 2003b.

J.P. Matas, J.F. Morris, and E. Guazzelli. Inertial migration of rigid spherical particles in poiseuille flow. Journal of Fluid Mechanics, 515:171–195, 2004. doi: 10.1017/S0022112004000254.

DH Michael. The stability of plane poiseuille flow of a dusty gas. Journal of Fluid Mechanics, 18(1):19–32, 1964.

Sebastian Mueller, EW Llewellin, and HM Mader. The rheology of suspensions of solid particles. Proceedings of the Royal Society A: Mathematical, Physical and Engineering Sciences, 466(2116):1201–1228, 2010.

R Narasimha and Rama Govindarajan. Minimal composite equations and the stability of non-parallel flows. Current Science, pages 730–740, 2000.

Anu VS Nath, Anubhab Roy, and M Houssem Kasbaoui. Instability of a dusty shear flow. arXiv preprint arXiv:2405.05539, 2024.

William M'F Orr. The stability or instability of the steady motions of a perfect liquid and of a viscous liquid. part ii: A viscous liquid. In Proceedings of the Royal Irish Academy. Section A: Mathematical and Physical Sciences, volume 27, pages 69–138. JSTOR, 1907.

S.A. Orszag. Accurate solution of the orr–sommerfeld stability equation. Journal of Fluid Mechanics, 50(4):689–703, 1971.

Balaji T Ranganathan and Rama Govindarajan. Stabilization and destabilization of channel flow by location of viscosity-stratified fluid layer. Physics of Fluids, 13(1):1–3, 2001.

Lord Rayleigh. On the stability, or instability, of certain fluid motions. Proc. London Math. Soc., 9:57–70, 1880.

Danial Rezaee. Linear temporal stability of jeffery-hamel flow of nanofluids. European Journal of Mechanics-B/Fluids, 2024.

V Ya Rudyak and Evgenii Borisovich Isakov. The stability of poiseuille fluid of a two-phase fluid with a nonuniform particle distribution. Journal of applied mechanics and technical physics, 37(1):80–88, 1996.

Valery Ya Rudyak, Evgeny B Isakov, and Evgeny G Bord. Hydrodynamic stability of the poiseuille flow of dispersed fluid. Journal of aerosol science, 28(1):53–66, 1997.

P. G. Saffman. The lift on a small sphere in a slow shear flow. Journal of Fluid Mechanics, 22(2):385–400, 1965. doi: 10.1017/S0022112065000824.

PG Saffman. On the stability of laminar flow of a dusty gas. Journal of fluid mechanics, 13(1):120–128, 1962.

Kirti Chandra Sahu and Rama Govindarajan. Stability of flow through a slowly diverging pipe. Journal of Fluid Mechanics, 531:325–334, 2005.

Hermann Schlichting and Klaus Gersten. Boundary-layer theory. springer, 2016.

Jeffrey A Schonberg and EJ1002883 Hinch. Inertial migration of a sphere in poiseuille flow. Journal of Fluid Mechanics, 203:517–524, 1989.

Galen B Schubauer and Harold K Skramstad. Laminar boundary-layer oscillations and stability of laminar flow. Journal of the Aeronautical Sciences, 14(2):69–78, 1947.

G. Segre and A. Silberberg. Radial particle displacements in poiseuille flow of suspensions. Nature, 189(4760):209–210, 1961.

G. Segre and A. Silberberg. Behaviour of macroscopic rigid spheres in poiseuille flow part 1. determination of local concentration by statistical analysis of particle passages through crossed light beams. Journal of fluid mechanics, 14(1):115–135, 1962.

Dhanush Shenoy, Mostafa Safdari Shadloo, Jorge Peixinho, and Abdellah Hadjadj. Direct numerical simulations of laminar and transitional flows in diverging pipes. International Journal of Numerical Methods for Heat & Fluid Flow, 30(1):75–92, 2020.

Braden Snook, Jason E. Butler, and Élisabeth Guazzelli. Dynamics of shear-induced migration of spherical particles in oscillatory pipe flow. Journal of Fluid Mechanics, 786: 128–153, 2016. doi: 10.1017/jfm.2015.645.

Ian J Sobey and Philip G Drazin. Bifurcations of two-dimensional channel flows. Journal of Fluid Mechanics, 171:263–287, 1986.

Arnold Sommerfeld. Ein beitrag zur hydrodynamischen erklaerung der turbulenten fluessigkeitsbewegungen. 1909.

Herbert Brian Squire. On the stability for three-dimensional disturbances of viscous fluid flow between parallel walls. Proceedings of the Royal Society of London. Series A, Containing Papers of a Mathematical and Physical Character, 142(847):621–628, 1933.

Gayathri Swaminathan, Kirti Chandra Sahu, A Sameen, and Rama Govindarajan. Global instabilities in diverging channel flows. Theoretical and computational fluid dynamics, 25:53–64, 2011.

Walter Tollmien. Über die entstehung der turbulenz. Vorträge aus dem Gebiete der Aerodynamik und verwandter Gebiete: Aachen 1929, pages 18–21, 1930.

Milton Van Dyke. Perturbation Methods in Fluid Mechanics. Academic Press, New York, 1964.

Chaofan Wen, Robert J Poole, Ashley P Willis, and David JC Dennis. Experimental evidence of symmetry-breaking supercritical transition in pipe flow of shear-thinning fluids. Physical Review Fluids, 2(3):031901, 2017.

Zhaosheng Yu, Tenghu Wu, Xueming Shao, and Jianzhong Lin. Numerical studies of the effects of large neutrally buoyant particles on the flow instability and transition to turbulence in pipe flow. Physics of Fluids, 25(4), 2013.